

Studies of space charge dominated beam in the spiral inflector and central region of cyclotron

by

**ANIMESH GOSWAMI
VARIABLE ENERGY CYCLOTRON CENTRE
Kolkata-700064, India**

*A thesis submitted to the
Board of Studies in Physical Sciences
in partial fulfillment of requirements
for the Degree of
DOCTOR OF PHILOSOPHY*

of

**HOMI BHABHA NATIONAL INSTITUTE
Bhabha Atomic Research Centre
Mumbai-400085, India**



September, 2012

Homi Bhabha National Institute
Recommendations of the Viva Voce Board

As members of the Viva Voce Board, we certify that we have read the dissertation prepared by Animesh Goswami entitled “Studies of space charge dominated beam in the spiral inflector and central region of cyclotron” and recommend that it may be accepted as fulfilling the dissertation requirement for the Degree of Doctor of Philosophy.

Date:

Chairman: Dr. Alok Chakrabarti

Date:

Guide/Convener: Dr. V. S. Pandit

Date:

Member: Dr. S. Krishnagopal

Date:

Member: Dr. P. R. Sarma

Date:

Technical Adviser: Shri Gautam Pal

Date:

External Examiner: Dr. Amit Roy

Final approval and acceptance of this dissertation is contingent upon the candidates submission of the final copies of the dissertation to HBNI.

I hereby certify that I have read this dissertation prepared under my direction and recommend that it may be accepted as fulfilling the dissertation requirement.

Date:

STATEMENT BY AUTHOR

This dissertation has been submitted in partial fulfillment of requirements for an advanced degree at Homi Bhabha National Institute (HBNI) and is deposited in the Library to be made available to borrowers under rules of the HBNI.

Brief quotations from this dissertation are allowable without special permission, provided that accurate acknowledgement of source is made. Requests for permission for extended quotation from or reproduction of this manuscript in whole or in part may be granted by the Competent Authority of HBNI when in his or her judgment the proposed use of the material is in the interests of scholarship. In all other instances, however, permission must be obtained from the author.

ANIMESH GOSWAMI

DECLARATION

I, hereby declare that the investigation presented in the thesis has been carried out by me. The work is original and has not been submitted earlier as a whole or in part for a degree / diploma at this or any other Institution / University.

ANIMESH GOSWAMI

Dedicated to my loving daughter “Anwasha”

ACKNOWLEDGEMENTS

First I would like to express my sincere gratitude to Dr. V. S. Pandit for his valuable guidance, supervision and constant encouragement throughout my thesis work. His broad experience and knowledge of many areas of science were extremely helpful. Working with him was a pleasant and exciting experience.

I would like to sincerely thank Dr. R. K. Bhandari (Former Director, VECC, Kolkata) and Dr. D. K. Srivastava (Director, VECC, Kolkata) for their continuous support to continue my work.

I express my thanks to Dr. P. R. Sarma and Shri S. C. L. Srivastava for many valuable and fruitful discussions we had on the topic of accelerator physics, and the helpful suggestions they offered from time to time.

I tender my grateful thanks to my colleagues Shri P. Sing Babu, Shri A. Misra and Shri S. Srivastava. I could not have completed my thesis without the support and encouragement from them.

I am grateful to Shri G. Pal, Shri C. Nandi, Shri S. Roy, Shri S. Bhattacharya, Smt. Mou Chatterjee, Shri R. C. Yadav and Shri S. K. Thakur for their assistance with assembling parts of the ion source, beam transport line and the spiral inflector. Numerous scientific, engineering, technical and office staff members from VECC, Kolkata offered helpful suggestions throughout the course of my thesis work. I thank all of these people for their time and effort.

I am thankful to my wife, Smt. Anupama Goswami, for her love and support. Her understanding and care were so important to me in my work and every-day life. I am eternally grateful to my parents and sister for their love and care, for everything what they have done for me in my life.

Contents

Synopsis	x
List of Figures	xvi
1. Introduction	1
1.1. Overview of cyclotrons	2
1.2. Space charge effect in cyclotron	6
1.2.1. Transverse space charge effect	7
1.2.2. Longitudinal space charge effects.....	8
1.3. Axial injection and inflectors	9
1.3.1. Mirror inflector	10
1.3.2. Hyperboloid inflector.....	10
1.3.3. Parabolic inflector.....	10
1.3.4. Spiral inflector	11
1.4. Microwave ion source and its injection system at VECC	11
1.5. Outline of the thesis.....	14
1.6. Summary	18
2. Space charge effects in a compact cyclotron	19
2.1. Introduction	19
2.2. Method of simulation	21
2.2.1. Cyclotron parameters.....	21
2.2.2. Betatron tunes	24
2.2.3. Beam envelopes	25
2.3. Numerical results and discussions.....	26
2.3.1. Preliminary design of the 10 MeV magnet.....	26
2.3.2. Transverse space charge effect and limiting current	28

2.3.3. Effect of input conditions on limiting current	33
2.3.4. Longitudinal space charge effect and turn separations	34
2.4. Summary	36
3. Design of magnet and spiral inflector for 10 MeV compact cyclotron.....	37
3.1. Introduction	37
3.2. Cyclotron magnet design.....	38
3.2.1. Optimization with Random search method	38
3.2.2. Optimized magnet geometry.....	42
3.2. Design of the spiral inflector	47
3.2.1. Coordinate system.....	48
3.2.2. Central ion trajectory	50
3.2.3. Central ion trajectory in a constant magnetic field.....	53
3.2.4. Orbit calculations and design parameters	54
3.2.5. Orbit centering	56
3.3. Summary	58
4. Space charge effect in the spiral inflector	59
4.1. Introduction	59
4.2. Transverse beam dynamics	60
4.2.1. Space charge field.....	60
4.2.2. Paraxial ray equations	62
4.2.3. Beam envelopes	64
4.3. Numerical results and discussions.....	66
4.3.1. Behaviour of beam envelopes.....	67
4.3.2. Study of emittance growth.....	70
4.3.3. Estimation of transverse acceptance	72
4.3.4. Effect of input parameters on beam behaviour	73

4.4. Summary	76
5. Envelope oscillations and amplitude growth in a compact cyclotron	78
5.1. Introduction	78
5.2. Calculation of Betatron tunes	79
5.3. Accelerated Beam envelope equations.....	82
5.4. Numerical results and discussions.....	86
5.4.1. Beam envelopes in a particular orbit	87
5.4.2. Beam envelopes along accelerated orbit.....	91
5.4.3. Estimation of limiting current.....	95
5.5. Summary	98
6. Elliptical solenoid and matching of intense beam to the spiral inflector	100
6.1. Introduction	100
6.2. Theoretical analysis.....	101
6.2.1. Potential for elliptical solenoid.....	102
6.2.2. Equations of motion.....	104
6.2.3. Infinitesimal transfer matrix and beam envelope	109
6.3. Beam optical properties of elliptical solenoid.....	111
6.3.1. Focusing characteristics.....	112
6.3.2. Study of inter-plane coupling effect	114
6.3.3. Parametric dependence of emittance growth.....	118
6.3.4. Conversion of an elliptical beam to a circular beam	120
6.4. Transverse beam matching to the spiral inflector	121
6.5. Summary	123
7. Conclusions and future works.....	124
7.1. Conclusions	124
7.2. Future works.....	127

Synopsis

The development of high current cyclotrons and study of the behavior of the space charge dominated beam during injection and acceleration is an important area of current research, and the complexities associated with their dynamics are still not well understood. Under the accelerator driven subcritical systems (ADSS) programme, our group at Variable Energy Cyclotron Centre, Kolkata, has undertaken the development of a 10 MeV, 5 mA compact radial sector proton cyclotron. A proton beam of $\sim 10\text{-}20$ mA at energy 80-100 keV from a 2.45 GHz microwave ion source will first be collimated by slits to remove the undesired components (H_2^+ , H_3^+ etc.), bunched using a sinusoidal buncher and will be injected axially into the central region of the cyclotron where a spiral inflector will place the beam on the proper orbit. Two delta type resonators located in the opposite valleys, will be used to accelerate the beam. Finally, this accelerated beam will be extracted using an electrostatic deflector. The main aim of this project is to study and settle various physics and technological problems associated with the production, bunching, acceleration, injection, extraction, etc. of the high intensity beams. The ion source and injection system of the compact cyclotron have been designed, fabricated indigenously, installed and commissioned. Presently it is under testing for beam characterization.

This thesis presents the results of simulation works carried out to settle some of the physics issues related with the injection and acceleration of a space charge dominated beam in a compact cyclotron. The design issues of a spiral inflector, main magnet and space charge effect on the behaviour of the beam envelope in the spiral inflector and cyclotron have been discussed. The analysis is performed for a 10 MeV high current compact proton cyclotron with injection energy of 80 keV and current in the range of 5-10 mA.

In a compact cyclotron, the vertical focusing obtained from the sectors is very weak in the central region. The transverse space charge force further reduces this focusing force. This effect leads to an increase in the beam size and thus sets a limit on the beam current that can be accommodated in a given aperture. A preliminary estimate indicates that the limiting current can be improved by increasing the injection energy of the beam and by optimizing the geometry of the cyclotron to improve the focusing forces. The first part of this thesis consists of determining the preliminary design parameters of the 10 MeV cyclotron. A hard-edge formulations and the transfer matrix technique have been used. A numerical simulation technique has been developed for studying the behaviour of the beam envelope during the first turn and also to estimate the vertical acceptance of the cyclotron central region in the presence of linear space charge. Here hills and valleys are treated as bending magnets with uniform field. The flaring and edge effects have been introduced by using thin lenses at each hill-valley boundary. The acceleration effect of two resonators in the opposite valleys has been included by approximating them with four step-function accelerating gaps. The change in the beam envelope has been studied by changing the injected beam current, initial width, divergence and emittance of the beam. A proper matching condition has been found and the limit on the injected beam current has also been estimated.

The results of these initial studies are then used to design the magnet of the 10 MeV cyclotron. The magnetic field in the cyclotron guides the particles on isochronous trajectories and provides the required focusing in order to maintain good internal beam characteristics. The available analytical formulas for calculating the average magnetic field and betatron frequencies are not valid for high flutter field and particularly at the lower radii in the case of a compact cyclotron. Another difficult problem to solve is the shaping of the magnetic field in the central region. In our case the use of high injection

energy (80 keV) requires a comparatively larger space for the spiral inflector. Therefore, a careful optimization of the central plug is also needed. To optimize the pole profile of the hill of the cyclotron magnet an iterative technique has been developed. Here the sector shape is approximated by a polynomial function of radius. A 3D magnet code MagNeT is used to calculate the magnetic field in the median plane and an equilibrium orbit code GENSPEO is used to obtain the betatron frequencies as a function of energy. The frequency error is minimized by optimizing the coefficients of the polynomial by using the random search technique. When compared with other methods, it is found that this method gives smooth pole shape of the hill and takes less computation time for optimization. It requires only 5-8 parameters for restricting the relative frequency error to 1 in 10^4 . The required isochronous field, within the tolerances, is obtained after several iterations, by shimming the angular width of the hill as a function of radius.

As mentioned earlier, a spiral inflector will be used to place the injected beam on the proper orbit in the central region of the cyclotron. In this thesis a detailed design of the spiral inflector and the dynamics of a space charge dominated beam through it have been discussed. Due to low average magnetic field and large difference between hill and valley fields, the computed magnetic field in the central region near the axis of the 10 MeV cyclotron is slightly lower than the resonance field. Near the central region it varies with height as well as with radius. Due to these large variations, the design of the spiral inflector needs special attention and is challenging. A computer code has been developed to solve the equations of motion using fourth order Runge Kutta method for the central ion trajectory in the spiral inflector using the non-homogeneous magnetic field obtained from a 3D code MagNeT. The parameters of the inflector are adjusted iteratively to orient the beam properly at its exit to produce a well centered beam. The orbit centering of the inflected beam is checked by using the central region code in the analytic electric field and

computed magnetic field. It has been shown that the beam is well centered with the input conditions provided by the spiral inflector.

For better transportation in the inflector and further acceleration in the cyclotron, the emittances and orientations of beam ellipses at the exit of the inflector should be matched to the acceptance of the central region. Any mismatch in the injection causes growth of beam sizes and emittances and finally leads to beam loss. Since knowledge of the central ion trajectory does not provide any information about how the inflector modifies the optical properties of the ion beam, a detailed study of beam dynamics using a uniform ellipsoidal bunch, and including the effect of space charge, has been carried out. As the injected dc beam from the ion source approaches the inflector, it takes the form of a bunch due to bunching action. The beam current in the bunch increases gradually as it traverses inside the spiral inflector. This effect modifies the space charge force on the particles in the beam and has been taken into account in the analysis. The optical properties of the spiral inflector have been studied using infinitesimal transfer matrix technique and sigma matrix method. The emittance growth that results from the coupling between the two transverse planes for different initial beam conditions has been estimated. The initial conditions of the beam have been optimized to reduce the emittance growth at the exit of the inflector. Simulation results show that a converging non-axisymmetric beam with equal emittances at the entrance is desirable to reduce the emittance growth at the exit.

It is well known that a beam matched to a transport system produces minimum envelope oscillations and amplitude growth. Envelope mismatch is the major cause of emittance growth and halo formation. For mismatch beams, an unbalance between the applied focusing force and the defocusing forces due to space charge and thermal effects, cause whole beam to oscillate in a coherent way. This effect increases the beam size in both the transverse planes and causes severe beam loss. In the case of low beam current

the mismatch in one plane affects the beam behaviour only in that particular plane. However, in the case of an intense beam, where the space charge effect couples the motions of the two transverse planes, a mismatch in one plane affects the beam behaviour in both transverse planes. The preliminary studies of the effect of space charge in the compact cyclotron carried out during the initial design estimate are limited in accuracy; however, they provide good insight into the behaviour of beam envelopes. This limitation is due to the use of the hard edge model of the magnetic field which overestimates the vertical betatron tunes at the lower radii. A more detailed study has been carried out on the amplitude growth and oscillations in the beam envelopes along the accelerated central orbit in the computed magnetic field assuming a uniform ellipsoidal bunch. The study has been done by changing the current of the injected beam, as well as the initial width and divergence of the beam. First, the pattern of envelope oscillations and amplitude growth of the beam in both transverse planes at a particular radius (without acceleration), by displacing the initial beam size from the matched beam size at several values of beam current, has been discussed. Then the results of studies on the behaviour of the beam envelope in the 10 MeV cyclotron for different initial conditions of the beam has been addressed. The proper matching conditions have been obtained by adjusting the input beam parameters to minimize the amplitude growth and oscillations. The maximum beam current that can be transported through a given focusing channel of the compact cyclotron has also been estimated.

Finally, since the overall goal of this thesis is to maximize the amount of beam that can be injected into the cyclotron, a transverse beam matching at the inflector entrance is necessary. Simulation results indicate that convergent phase ellipses with different orientations in x and y planes and a comparatively smaller width in the y plane give better beam transmission. The transformation of an axisymmetric beam from the ion source to a

non-axisymmetric beam at the entrance of the spiral inflector can't be achieved by using cylindrical symmetric magnets such as Glaser and solenoid magnets as used in the transport line. In this case one needs either an elliptical solenoid or a quadrupole doublet. In our case an elliptical solenoid is more suitable than the quadrupole doublet due to space constraint. In the thesis the beam optical properties of an elliptical solenoid magnet have been studied, including the effect of space charge, and the feasibility of using an elliptical solenoid for transverse matching of a space charge dominated beam to the acceptance of a spiral inflector has also been discussed.

List of Figures

1.1.	2.45 GHz microwave ion source on the high voltage deck and solenoid based low energy beam transport line.	12
1.2.	Beam spot of 80 keV, 5 mA on water cooled alumina plate.....	13
2.1.	Orbit section in one period of magnetic field consisting of a hill and a valley.....	23
2.2.	(a) A schematic of sector geometry obtained using the hard-edge formulations and the transfer matrix technique. (b) Radial and vertical betatron tunes as a function of beam energy.	27
2.3.	Behavior of beam envelopes in the radial and vertical directions with distance s along the equilibrium orbit for the first turn with zero beam current: (a) no acceleration, (b) accelerations and soft-edge effects. Normalized emittance $\varepsilon_n = 0.8 \pi$ mm mrad in both the transverse planes.....	29
2.4.	Results of numerical calculations: (a) beam envelopes in the radial and vertical directions with accelerations, soft-edge effects and $I = 5.85$ mA. Envelope amplitude is restricted to ≤ 5 mm in both planes, (b) phase ellipses in the radial and vertical directions used as initial condition. These are the matched ellipses (Fig. 2.2(a)) with $I = 0$ mA..	30
2.5.	Results of optimization: (a) beam envelopes with amplitude ≤ 5 mm in the radial and vertical planes optimized using upright phase ellipses in both planes, (b) upright beam ellipses with normalized emittance $\varepsilon_n = 0.8 \pi$ mm mrad in both planes.	31
2.6.	Beam envelopes in the radial and axial planes optimized with tilted phase ellipses to accommodate more beam current (15.8 mA). (a) Beam envelopes with amplitudes ≤ 5 mm, and (b) phase ellipses with normalized emittance $\varepsilon_n = 0.8 \pi$ mm mrad in both planes.....	32
2.7.	Beam envelopes in the radial and axial planes injection energy 80 keV and acceleration voltage 125 kV (a) Beam envelopes with amplitudes ≤ 5 mm, and (b) phase ellipses with emittance $\varepsilon_n = 0.8 \pi$ mm mrad in both planes.	33
2.8.	Variation of limiting current as a function of injection energy for various values of beam emittance. In all cases the half aperture is restricted to 5 mm in both the planes.....	34

3.1.	Magnet model built in the code.....	43
3.2.	Decrease in frequency error as a function of energy at different iterations. Here numbers 1,2,3... indicate the results obtained after that many iterations.....	44
3.3.	Hill shape and hill angle optimized by two methods. Dotted curve shows the initial hill angle obtained using hard edge approximation.	45
3.4.	Equilibrium orbit properties of the optimized magnet. (a) Radial and axial betatron tunes as a function of energy. Dotted curves represent the analytical values. (b) The optimized average magnetic field and required isochronous magnetic field (dotted) as a function of energy. (c) The phase slip $\sin \phi$ as a function of energy for initial phase $\phi_i = 2^0$, harmonic number $h = 4$ and peak energy gain per turn 500 keV..	46
3.5.	Variation of the magnetic field with distance z from the median plane along the cyclotron axis. Data is obtained from 3D code.	48
3.6.	A schematic of fixed right handed cartesian (x, y, z) and optical (u, h, v) coordinate system. The electric field is along the x direction at the entrance of the inflector and the magnetic field is uniform and opposite to the z direction..	49
3.7.	Spiral inflector geometry as viewed from a plane perpendicular to the central trajectory. Here d is the electrode spacing and S is the width of the electrodes.....	51
3.8.	Electrode geometry of the spiral inflector. Ground electrodes at the entrance and exit are not shown in the figure.	55
3.9.	Plot shows comparison of the analytic (dotted) and computed (solid) electric fields along the central ion trajectory in the spiral inflector.....	56
3.10.	Position of the inflector, location of the accelerating gaps G-1 to G-4 in the median plane (x - y plane) and accelerated orbits of proton from 80 keV to 10 MeV.....	57
4.1.	The variation of bunching factor B_f with path length as the beam bunch moves inside the spiral inflector, showing the effect of bunching action of a sinusoidal buncher. The entrance of the inflector is located at 65 cm from the buncher gap.	67
4.2.	The evolution of beam sizes through the spiral inflector in u and h planes for average beam current $I = 0$ mA (dotted curve) and $I = 5$ mA at the inflector	

	exit. Dashed curves are for case of uniform cylindrical beam and solid lines belong to uniform ellipsoidal bunched beam.....	68
4.3.	Comparison of beam envelopes for ellipsoidal bunch with constant current (dashed curve) and gradually increasing current (solid curve) from entrance to exit.....	69
4.4.	Variation of un-optimized (dotted curve) and optimized (solid curve) beam emittances in u and h planes at the exit of the inflector as a function of the beam current. The initial beam emittance is 60π mm mrad in both phase planes.....	71
4.5.	Phase ellipses in h and u planes; (a) and (b) represent the optimized phase ellipses at the inflector entrance. (c) and (d) show the phase ellipses at the inflector exit for $I_{exit} = 5$ mA. Solid lines indicate the area pertaining to the particular phase plane and dashed lines the area arising from the coupling with other phase planes. The dotted curves in (c) and (d) represent the effective phase ellipses obtained using sigma matrix method.....	72
4.6.	Variation of acceptance as a function of beam current.....	73
4.7.	Paraxial trajectories of 1000 particles with equal input emittances 60π mm mrad in both the planes at $I = 0$ mA and $I = 5$ mA. (a) axisymmetric upright ellipse with $U = H = 4$ mm and $P_u = P_h = 0$ mrad (b) non-axisymmetric tilted ellipse with $U = 4$ mm, $H = 2.3$ mm and $P_u = -6$ mrad, $P_h = -31$ mrad (optimized condition of Fig. 4.5).....	74
4.8.	Transverse cross-sections of the beam at different locations in the spiral inflector at $I = 0$ mA and $I = 5$ mA for axisymmetric and non axisymmetric input beams.....	75
4.9.	Paraxial ion trajectories and resulting beam envelopes through the spiral inflector in both u and h planes for $I = 0$ mA and $I_{exit} = 5$ mA. Input conditions are optimized.....	76
5.1.	Betatron tunes as a function of orbit radius. Dashed curves represent the contribution to the vertical betatron tunes ν_y (solid line) from the electric and magnetic focusing. The initial rf phase θ_c is equal to 5°	81
5.2.	A schematic of coordinate system attached to the beam bunch moving along the accelerated orbit in the median plane.....	83

5.3.	The variation of (a) $(\beta\gamma)' / (\beta\gamma)$ and (b) bunch size $2Z$ as a function path length s along the accelerated orbits up to five turns. Long ticks on the middle horizontal line indicate the turn number. There are four kicks at four acceleration gaps in each turn.	87
5.4.	Radial and vertical beam envelopes, for different initial conditions at radius 30 cm without acceleration for five revolutions and three different values of beam current. Matched beam sizes are shown by dotted lines. All solid curves represent mismatch by 0.5 mm from the matched beam size whereas dashed curves represent mismatch by 1.0 mm from the matched beam size. The values of the matched beam sizes are (a) $X_m = 1.71$ mm, $Y_m = 1.98$ mm for 0 mA, (b) $X_m = 1.92$ mm, $Y_m = 2.38$ mm for 5 mA and (c) $X_m = 2.11$ mm, $Y_m = 2.84$ mm for 10 mA.	88
5.5.	Radial and vertical beam envelopes without acceleration, for different initial conditions at radius 30 cm for five revolutions at $I = 5$ mA beam current. Dotted lines represent the matched envelope sizes $X_m = 1.92$ mm and $Y_m = 2.38$ mm. The beam envelopes are for (a) $X = X_m - 0.5$ mm, $Y = Y_m + 0.5$ mm, (b) $X = X_m - 0.5$ mm, $Y = Y_m - 0.5$ mm, (c) $X = X_m - 0.5$ mm, $Y = Y_m$, (d) $X = X_m + 0.5$ mm, $Y = Y_m$	90
5.6.	Variation of matched beam envelope sizes X_m and Y_m as a function of orbit radius for various values of beam current.	92
5.7.	Beam envelopes along the path of the accelerated orbits up to final radius for $I = 0$ mA. (a) The initial beam sizes are the matched beam sizes $X_m = 1.92$ mm and $Y_m = 3.26$ mm at the injection radius (7.05cm) in both the planes. (b) Envelopes obtained after optimization of initial beam conditions to yield minimum amplitude of oscillations in the beam envelopes. Ticks on the horizontal central line indicate the number of turns.	93
5.8.	Radial and vertical beam envelopes along the path of the accelerated orbit up to final radius for $I = 5$ mA. (a) The initial beam sizes are the optimized sizes with $I = 0$ mA; $X_0 = 2.4$ mm, $X'_0 = -7$ mrad in the radial plane and $Y_0 = 2.6$ mm, $Y'_0 = -10$ mrad in the vertical plane at the injection radius. (b) Envelopes obtained after optimization of initial beam conditions to yield minimum oscillation in the envelopes ($X_0 = 3.7$ mm, $X'_0 = -27$ mrad, $Y_0 = 4.8$ mm, $Y'_0 = -32$ mrad).	94

5.9.	Input phase ellipses in x and y planes for (a) matched envelope sizes at injection radius for $I = 0$ mA (Fig 5.7(a)), (b) the optimized envelopes with acceleration and $I = 0$ mA (Fig 5.7(b)), (c) the optimized envelopes with acceleration and $I = 5$ mA (Fig 5.8(b)).	95
5.10.	Radial (X) and vertical (Y) beam envelopes along the accelerated orbits up to 10 MeV. (a) uniform ellipsoidal bunched beam with initial conditions $X_0 = 4.9$ mm, $X'_0 = -30$ mrad, $Y_0 = 5.3$ mm, $Y'_0 = -35$ mrad and (b) envelopes when the betatron tunes are scaled of by 1.15 times with same initial conditions as in (a).	96
5.11.	Optimized phase ellipses at the exit of spiral inflector in the central region of 10 MeV cyclotron and beam envelopes in x and y planes along the accelerated orbits with these input beam conditions.	98
6.1.	A schematic of rotated coordinate system (\tilde{x}, \tilde{y}) with respect to the laboratory coordinate system (x, y) by an angle θ , in which the semi axes of elliptical cross-section of the beam are aligned with the coordinate axes.	105
6.2.	Beam envelopes for (a) solenoid magnet and (b) elliptical solenoid magnet, for same initial axisymmetric beam with $X(0) = Y(0) = 0.25$ cm, $X'(0) = Y'(0) = 0$ mrad and $\varepsilon_x(0) = \varepsilon_y(0) = 60 \pi$ mm mrad for two different values of beam current $I = 0$ mA (solid curve) and $I = 10$ mA (dashed curve).	113
6.3.	Transverse projected x and y emittances through the solenoid (dashed line) and elliptical solenoid (solid line) for axisymmetric input beam. The input conditions of the beam are same as in the case of Fig. 6.2.	114
6.4.	Projected x and y emittances for $I = 0$ mA (solid line) and $I = 10$ mA (dashed line) through the (a) solenoid and (b) elliptical solenoid magnet for non-axisymmetric input beam. The input beam conditions in both cases are $X(0) = 0.5$ cm, $Y(0) = 0.25$ cm, $X'(0) = Y'(0) = 0$ mrad, $\varepsilon_x(0) = 70 \pi$ mm mrad and $\varepsilon_y(0) = 50 \pi$ mm mrad.	116
6.5.	Phase ellipses in x and y planes at the exit of elliptical solenoid along with contributions from the inter-plane coupling for initial uncoupled phase ellipses. Parameters of elliptical solenoid are $K = 0.04$ cm ⁻¹ , $J = 0.0003$ cm ⁻² and $L = 30$ cm.	117
6.6.	Transverse projected emittances at the exit of the elliptical solenoid as a function of the parameter J for three different values of beam current. (a) axisymmetric beam with $X(0) = Y(0) = 1.5$ cm. (b) non-axisymmetric beam	

- with $X(0) = 1.5$ cm, $Y(0) = 1.0$. Other input conditions are, $\varepsilon_x(0) = \varepsilon_y(0) = 60 \pi$ mm mrad and $X'(0) = Y'(0) = 10$ mrad. Parameters of the elliptical solenoid are $k = 0.04$ cm⁻¹ and $L = 30$ cm.119
- 6.7. Projected emittances at the exit of the elliptical solenoid as a function of the parameter J for beam currents $I = 0$ mA (solid line), $I = 10$ mA (dashed line) and $I = 20$ mA (dotted line) for an initial non-axisymmetric beam with $X(0) = 1.5$ cm, $Y(0) = 1$ cm, $X'(0) = Y'(0) = 10$ mrad, $\varepsilon_x(0) = 70 \pi$ mm mrad and $\varepsilon_y(0) = 50 \pi$ mm mrad. Parameters of the elliptical solenoid are $K = 0.04$ cm⁻¹ and $L = 30$ cm.120
- 6.8. Beam envelopes in x and y planes for 10 mA beam current through elliptical solenoid doublet to produce beam waists at the axial location ~ 105 cm. The initial beam is axisymmetric with $X(0) = Y(0) = 0.25$ cm and $\varepsilon_x(0) = \varepsilon_y(0) = 60 \pi$ mm mrad. Here “W” indicates the location of equal beam waist in both the planes.121
- 6.9. Beam envelopes and phase ellipses in the x and y planes for matching at the inflector entrance with average beam current $I = 5$ mA. The input beam parameters are $X(0) = Y(0) = 0.25$ cm, $\varepsilon_x(0) = \varepsilon_y(0) = 60 \pi$ mm mrad. The estimated emittances at the matching point M are $\varepsilon_x(M) = \varepsilon_y(M) = 61.4 \pi$ mm mrad.122

List of Tables

2.1. Parameters of the 10 MeV compact cyclotron	28
3.1. Initial and final optimized parameters.....	45
3.2. Parameters of the 10 MeV cyclotron.....	47
3.3. Optimized parameters of the inflector.....	55
3.4. Parameters used for orbit tracing	58

Chapter 1

Introduction

The production, acceleration and transport of intense charged particle beam is an active area of research and is at the center of various scientific studies. In the recent years high current cw accelerators, especially linacs and cyclotrons have received increased interests because of the need of high power and high quality beams for applications such as spallation neutron sources, accelerator driven systems (ADSS) and for nuclear waste transmutation. There has been a growing interest to understand the beam self field effects on focusing and transfer characteristics of intense charge particle beams.

The production of clean energy through controlled nuclear fission based on accelerators has been considered all over the world as quite feasible for nuclear power generation through ADSS. In practical realization of ADSS, the most challenging task is the development of a high energy (~ 1 GeV) and high current (~ 10 - 15 mA) proton accelerator to produce neutrons by spallation to drive a sub-critical reactor assembly [1, 2]. Cyclotron is an excellent option for delivering high power high current beam because of its compact structure, low beam losses, operation in cw mode and the most important is the cost factor for beam power levels ≤ 10 MW [3, 4].

Cyclotrons, operating presently in various laboratories around the world, were designed preliminarily for research in nuclear and particle physics with low beam current requirements. The compact cyclotrons designed for medical applications are providing hundreds of micro ampere beam. The beam power available from these machines is at least one order of magnitude lower than that needed for ADSS application. The overall efficiency of these machines is also very low. Much larger efficiency can be achieved by

designing the accelerator properly keeping in mind the power dissipation in rf and magnet. Today, cyclotron is the highest beam power accelerator (590 MeV, 1.8 MW at PSI) operating in cw mode [5].

In order to achieve 10 mA proton beam at 1 GeV using cyclotron, certain critical issues are required to be studied in detail, particularly at low energy regime where the space charge forces dominate. Before reaching the prototype stage of a driver accelerator for an ADSS plant much R & D works are needed to be carried out using proton beam of lower energy and lower current. Under the ADS development programme, a 10 MeV, 5 mA compact radial sector proton cyclotron [6-8] is being developed at the Variable Energy Cyclotron Centre in Kolkata. Proton beam from 2.45 GHz microwave ion source [9] will be first collimated by slits to remove the undesired components (H_2^+ , H_3^+ etc.), bunched using a sinusoidal buncher [10] and will be injected axially in the central region of the cyclotron where a spiral inflector will place the beam on the proper orbit [11-13]. Two delta type resonators located in the opposite valleys, will be used to accelerate the beam. Finally, this accelerated beam will be extracted using an electrostatic deflector. The main aim of this project is to study and settle various physics and technological problems associated with the production, bunching, acceleration, injection, extraction, etc. of the high intensity beams. The work presented in this thesis is related with the study of different aspects of the space charge dominated beam dynamics in a high current compact cyclotron. In the following section (1.1.) we first discuss the historical overview of the cyclotron and its research and commercial applications.

1.1. Overview of cyclotrons

The concept of cyclotron was originated by E. O. Lawrence and developed by him and his students [14]. He built his first cyclotron in 1930 followed by another, and used it for nuclear physics research. The basic principle of cyclotron is based on a combination of rf

acceleration and bending of charged particles in a magnetic field. Particles are accelerated in spiral paths inside two semicircular, flat metallic electrodes called dees. Dees are connected to an rf generator and are placed in a nearly uniform magnetic field. Charged particles, produced either by an ion source located at the centre of the cyclotron or by an external ion source, are injected into the median plane. The magnetic field causes particles to move in the median plane in approximately circular orbits inside the dee and across the gap between them. At each gap particles are accelerated and follow a spiral path as they gain energy. This is because the radius of orbit, being a function of the particle velocity, increases with time. At the edge of the magnet, full energy particle beam is pulled out (extracted) by an electrostatic deflector as an external beam.

Before reaching the final energy, ions complete over a several hundred turns. In a truly uniform field the particle orbits have no stability in the vertical direction. It was recognized during early days that the strength of the magnetic field had to decrease with radius to yield simultaneously the necessary radial and vertical stability of the orbit motion. This is in conflict with the requirement of resonance which demands that the particle revolution frequency must be equal to the frequency of the rf voltage throughout the acceleration process. The situation is in fact worse than this because of the relativistic variation of mass with velocity which requires that the strength of the magnetic field should increase with radius. Due to this reason, the final energy obtainable from the so-called classical cyclotrons was limited to $\sim 2\%$ of the rest mass energy of the particle.

In the long history of the cyclotrons, researchers have made many improvements to overcome the energy limitations. The earliest solution implies a frequency modulation of the accelerating voltage, such that the frequency keeps pace with revolution frequency of the particle. These types of cyclotrons, called synchrocyclotrons have a macro-structure in the beam current. The average beam current is much lower than that of the classical

cyclotrons. The other solution was suggested by L. H. Thomas [15, 16]. He proposed to maintain a constant orbit frequency as the mass increases with energy by increasing the magnetic field strength with radius. Such a field profile brings in vertical defocusing to the beam. To counteract this defocusing, Thomas proposed contouring the magnet pole faces to provide an azimuthal variation in the field strength. In practice, this is achieved by dividing the poles into symmetrical sectors each consisting of a “hill” with small pole gap and high magnetic field and a “valley” with a large pole gap and low magnetic field. The different orbit curvatures in hills and valleys lead to a scalloped orbit oscillating around a circle. This gives rise to radial velocity component strongest at the hill valley boundary whereas the hill fringing field provides an azimuthal component of magnetic field. The result is a vertical focusing force at each hill-valley boundary.

Two additional vertical focusing forces were discovered by Kerst and Laslett by making edges of the sectors spiral shaped [17]. The vertical focusing forces from the azimuthally varying magnetic field turned out to be large enough to correct the defocusing forces that are introduced by radially increasing magnetic field. This opened the possibility to adjust the magnetic field to take care of relativistic mass increase. The cyclotron with an Azimuthally Varying Field is mostly call the AVF cyclotron or sector focused cyclotron. The first AVF cyclotron using this principle was built in 1958 [18]. Since then AVF cyclotrons have been built in many ways ranging from small dedicated accelerators for isotope production to large facilities for basic research in nuclear and particle physics.

The major advances in the AVF cyclotron over the last forty years are the use of superconducting magnets and the axial injection systems. The first development allowed to reduce the size and weight of cyclotron magnets for a given energy by more than an order of magnitude, which was important for large heavy ion beam facilities. The major facilities are K500 superconducting cyclotron at VECC [19], K500 and K1200 coupled

cyclotron complex at MSU [20], the Radioactive Ion Beam Factory (RIBF) at RIKEN [21], the ACCEL' s superconducting 250 MeV proton cyclotron [22] for medical use etc.

Another important improvement is the use of external ion source that allowed the acceleration of high intensity and variety of heavy ion beams. The AVF cyclotrons thus become a unique and versatile instrument that can be tailored to a large variety of uses. GANIL in France, operating two coupled K380 cyclotrons [23], is the facility for high intensity heavy ion beams for the production of radioactive species. The world biggest room temperature cyclotron with a magnet having 18 meter diameter and total weight of 4000 tons built in early 70's is at TRIUMF in Canada [24]. It produces 500 MeV (500 μ A) proton beam for meson production. The commercial use of cyclotrons covers a large variety of applications. Best known are small cyclotrons for production of radioisotopes for medical uses such as positron emission tomography (PET), single photon emission computed tomography (SPECT) etc. The development of a 250-400 MeV/A cyclotron for radiation therapy with proton and carbon beams is an important step in bringing this advance technology into hospitals.

In recent years, high-current cyclotrons have received increased interest because of the need of high-power and high-quality beams as required for ADSS application. The feasibility of cyclotrons for producing high power beams has been discussed by many authors and accelerator complexes consisting of two or three cyclotrons with a compact cyclotron as an injector, have been proposed to deliver 10 mA, 1 GeV proton beam as needed by ADSS. At present the 590 MeV cyclotron facility at the Paul Scherrer Institute, Switzerland (PSI) is the only machine which is routinely operated at 1.2 MW beam power as driver for the spallation neutron source SINQ [5]. As possible future applications, several proposals to generate about 10 MW of beam power using cyclotrons are in active considerations around the world.

1.2. Space charge effect in cyclotron

In the beam intensity region that we are considering here (several mA) the space charge effects play crucial roles in the beam dynamics. Space charge forces of the beam in a cyclotron affect the beam behavior in both transverse and longitudinal directions [25, 26]. Transverse space charge forces increase the beam sizes and reduce the betatron frequencies. If this reduction is significant which is serious in the axial direction, axial beam loss could occur. Longitudinal space charge force on the other hand increases the energy of the leading edge of the bunch and reduces the energy of the tail of the bunch. Because of the radius-energy correlation in cyclotrons, this energy spread expands the radial region occupied by each turn. Thus, this effect reduces the turn separation and causes a limitation on the beam intensity that can be accelerated in a cyclotron.

While the transverse space charge effects are serious only at low energies, longitudinal ones are of concern throughout. The calculation and simulation of space charge effects are very complicated. Self-fields, external focusing fields and relative motion of individual particles in the bunch separated from the motion of the bunch have to be taken into account. The relative motion of particles in the bunch changes the density distribution which defines the fields. Thus the space charge force and the density distribution have to be treated in a self-consistent manner. For understanding the behavior of tails and halos simulations have to be done with a very large number of particles. Since the tails of the profiles are determined by the nonlinear terms of the force, an accurate knowledge of the charge distribution in the bunch is necessary to calculate them which are very difficult to get for a cyclotron beam. So, an accurate prediction of the behavior of beam losses under space charge force is close to impossible. However, an insight in the essential features can be derived from simple models and the analysis of the simulation results.

1.2.1. Transverse space charge effect

In a cyclotron the transverse space charge effect is strongest on the first few turns particularly in the axial direction because the energy of the beam is low and focusing forces are small in the region near the machine center. An estimation of transverse space charge effect can be obtained by calculating the tune shift. The tune shift for a continuous un-bunched beam can be given by [26]

$$\nu_y^2 = \nu_{0y}^2 - 6.44 \times 10^{-8} \times \frac{Q}{A} \frac{I}{(\beta\gamma)^3} \frac{R}{a^2} \quad (1.1)$$

$$\nu_y = \nu_{0y} + \delta\nu_y \quad (1.2)$$

Here ν_{0y} is the axial betatron frequency at zero beam current, Q is the charge state and A is the mass number of the particle. I is the peak current of the beam of diameter $2a$ and R is the average radius of the machine. A large tune shift reduces the focusing force on the beam particles and difficulties with resonances arise if $\delta\nu_y \geq 0.5$. An absolute limit is reached if $\delta\nu_y \geq \nu_{0y}$.

In order to estimate the transverse space charge effect, Blosser and Gordon [27] used a model consisting of a uniformly charged wedge and obtain an expression for the limiting current that would decrease the vertical focusing frequency to zero as

$$I_{\text{lim}} = (\Delta y) \nu_y^2 \omega \varepsilon_0 \left(\frac{\Delta\phi}{2\pi} \right) \left(\frac{\Delta E}{Qe} \right) \quad (1.3)$$

where Δy is the beam height, ω is the orbital angular frequency, ε_0 is the permittivity of vacuum, $\Delta\phi$ is the full beam phase width, ΔE is the energy gain per turn and Qe is the ion charge. Joho [28] also developed a model appropriate for the case of separated turns with the following current limit:

$$I_{\text{lim}} = \frac{AI_0\beta}{4Q} \nu_y^2 \left(\frac{b^2\omega^2}{c^2} \right) \left(\frac{\Delta\phi}{2\pi} \right) \quad (1.4)$$

where $I_0 = 31 \text{ MA}$, $2b$ is the beam height. The above mentioned expressions of the limiting current indicates that for acceleration of high beam current in a cyclotron it is necessary to have high axial betatron tune ν_y and large beam phase width. The injection energy and energy gain per turn ΔE should also be as high as possible.

1.2.2. Longitudinal space charge effect

Special attention is needed to be paid to longitudinal space charge effects, because isochronous cyclotrons do not have the property of longitudinal focusing. In the first order approximation the longitudinal space charge force causes an additional energy spread in the beam. It causes trailing particles in a bunch to lose energy. The broadening of the bunch due to the linear part can be compensated by adjusting the phase away from the peak of the rf voltage. If a flattop system is used then it can be compensated by adjusting the phase of the third harmonic with respect to the accelerating rf voltage. The nonlinear part results in deterioration of the beam quality and increase in the loss of beam due to long tails on the beam profiles.

A rough estimate of space charge induced energy spread ΔE_{sc} can be obtain by the integration of longitudinal electric field E_l over the whole path of the particle in a cyclotron as [26]

$$\Delta E_{sc} = \frac{2}{\gamma^2} \int qE_l 2\pi R dn \quad (1.5)$$

The turns remain separated as long as this energy spread is less than the energy gain per turn at the extraction radius. Based on “sector model” Joho [28] deduced a very useful scaling law that the maximum beam current scales with $\frac{1}{N^3}$, where N is the total number of turns. Thus for acceleration of high beam current in a cyclotron the turn number N

should be small which implies a high energy gain per turn. A preliminary estimate of current limit due to longitudinal space charge effect can be obtained from

$$I_{\text{lim}} = \frac{T \varepsilon_0 \delta \Delta\phi}{2N^2 \ln(1 + \sqrt{2})} \quad (1.6)$$

where T is the final kinetic energy, N is the number of turns and δ is the cross section of the bunch with phase width $\Delta\phi$.

The criteria stated above give only a rough estimate of the intensity limit from the transverse and longitudinal space charge effects. Therefore, a more detailed study and simulations are needed to know the actual beam behavior in the cyclotron.

1.3. Axial injection and inflectors

One of the greatest improvements in the operation of the AVF cyclotron over the last thirty years has been the use of the external ion sources and axial injection system. This scheme has many advantages in terms of the high current operation, easy maintenance, possibility of pre-acceleration of the beam etc. The job of the axial injection system is to transport the ion beam from the external ion source to the injection point located at the central region of the cyclotron. In this system the ion beam enters into the axial bore of the cyclotron magnet and finally bent by 90° into the median plane of the cyclotron by means of an inflector. Most of the deflectors consist of two parallel electrodes across which an electric field is applied. The beam inside the inflector is affected by the action of both electric and magnetic fields and so the design of the inflector is complicated in nature. In the following subsection we briefly discuss about the most widely used deflectors in the cyclotrons such as electrostatic mirror [29], hyperboloid inflector [30], parabolic inflector [31] and spiral inflector [32].

1.3.1. Mirror inflector

The mirror inflector consists of a pair of planer electrodes which are positioned at an angle of about 45° to the incoming ion beam. To allow the ion beam to enter the inflector one electrode is made of grid of wires. The grid is grounded and a dc voltage is applied to the other electrode. Ions entering axially in the mirror inflector are bent by 90° in the median plane. Although the mirror inflector has a simple structure, the grid reduces the transmission efficiency and increases the effective emittance of the beam at its exit. Since ions do not travel in an equipotential line inside the mirror inflector, it requires almost same voltage as the injection voltage for the inflection.

1.3.2. Hyperboloid inflector

The hyperboloid inflector was proposed by Muller. The electrodes are formed by two pieces of concentric hyperboloids and their rotation axis is parallel to the magnetic field. The electric field distribution inside the inflector possesses radial symmetry. This means that once the magnetic radius of curvature has been chosen the inflector geometry is completely fixed and hence there are no free parameters in the inflector design for readjustment of orbit centre. It provides the complete decoupling between the radial and axial motion and hence there is no growth in the effective emittance. The matching of the beam emittance at the inflector exit with the cyclotron acceptance is much simple to obtain. The central trajectory is along an equipotential, but the contribution of electric field is not always to bend the beam by 90° . This inflector is not compact.

1.3.3. Parabolic inflector

In this inflector the electrodes are obtained from the bending sheets of metal plates into a parabolic shape. It requires relatively low voltage and is easy to manufacture using standard machine shop techniques. The one of the electric field components is always zero at all points within this inflector. It has the same disadvantages as the hyperboloid; there

are no free parameters, and the dimensions of the device are relatively large. Nowadays this type of inflector is rarely used.

1.3.4. Spiral inflector

The spiral inflector has now become most widely used inflecting device owing to its flexibility, relatively low voltage needed for operation and almost 100% transmission efficiency. First developed by Belmont and Pabot [32], it is a three-electrode device consisting of a pair of biased electrodes housed into a grounded shielding, being the third electrode. Since this inflector is used in a magnetic field, the biased electrodes have a twisted shape to take into account the spiraling of the ion trajectory due to the magnetic field. The biased electrodes produce an electric field perpendicular to the design orbit to inflect ions. Since the central ion trajectory always lies on an equipotential surface the required voltage to inflect ions is much lower. The beam inside the spiral inflector is affected by the action of both electric and magnetic fields and so the ion trajectories are complicated in nature. The shape and size of the spiral inflector depends on magnetic radius, electric radius, tilt parameter, spacing and width of the electrodes etc [33]. However, for a given magnetic field and injection energy of the beam, the final shape to meet the beam centering requirements depends on two adjustable parameters, the inflector height and the tilt angle. This fact makes the spiral inflector more flexible compared to other deflectors used in cyclotrons.

1.4. Microwave ion source and its injection system at VECC

In this section we will briefly present the description of the off-line testing stand of injection system of the cyclotron which consists of a microwave ion source and approximately 3 meter long low energy beam transport line (LEBT). The microwave ion source (2.45 GHz, 80 kV, 20 mA) is presently under testing for performance improvement

[9, 34]. Beam from the ion source will be transported by a low energy beam transport line and will be injected axially into a 10 MeV, 5 mA compact cyclotron. The ion source (shown in Fig. 1.1) consists of a plasma chamber, two movable solenoids to produce desired magnetic field and a triode ion extraction system. The diameter of the apertures in the plasma electrode, accelerating electrode and de-accelerating electrodes are 7 mm, 10 mm and 10 mm respectively. The plasma chamber is a double walled water-cooled cylindrical stainless steel chamber of 100 mm length and 90 mm diameter. The microwave power from the 2.45 GHz, 1.2 kW magnetron is coupled to the chamber through a three stubs tuning unit, an auto tuner and water cooled ridged wave-guide.



Fig. 1.1. 2.45 GHz microwave ion source on the high voltage deck and solenoid based low energy beam transport line.

Ion source with adjustable solenoid, its power supplies, microwave generator, a high precision gas flow system etc., all are kept at a high voltage deck ~ 100 kV. High voltage deck is separated from the ground through polypropylene insulators. A two-segment ceramic insulators (Al_2O_3) column, which supports the beam extraction electrodes, separates the high voltage deck and the beam line at the ground potential. Power to the various subsystems on the deck is supplied using a 150 kV, 30 kW isolation transformer. Control units for adjusting current in the solenoids, movement of solenoids, tuning of microwave power, adjustment of gas flow etc. is placed on the high voltage deck. The

control and monitoring of the various voltages and current for different subsystems are done with a PC at ground potential through optic fibre.

The injection beam line (shown in Fig. 1.1) consists of two magnetic solenoids, some diagnostic elements such as slits, faraday cup and emittance monitoring box. The beam from the ion source is expected to contain a substantial fraction (~10 to 20%) of molecular hydrogen ion. Two motor controlled independent slits at the waist location of proton between the two solenoids, one set for the x -plane and other set for the y -plane, are used to control the size of the proton beam and to reject most of the molecular hydrogen beam [35]. We have also provided another water cooled fix slit of 4 cm dia after the first solenoid and before the waist position of protons. Beam current measuring equipments used in the beam line are; a DCCT just after the extraction, a water-cooled faraday cup (up to 10 mA only) with secondary electron suppresser after the slit and a faraday cup cum beam dump at the end of the LEBT. Three turbo pumps having pumping speed of 520 l/s are used to evacuate the entire system.

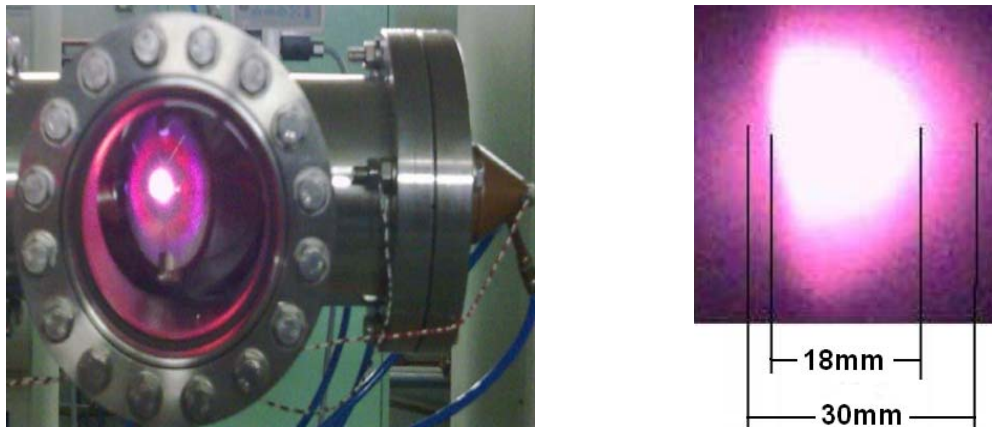


Fig. 1.2. Beam spot of 80 keV, 5 mA on water cooled alumina plate.

We have achieved a stable beam current around 10 mA on DCCT and 7 mA on the faraday cup through 1 cm \times 1 cm slit just before the faraday cup at 500 W of microwave power at an extraction voltage of 80 kV. We have transported this beam up to the length of ~ 3 meter at the last beam dump near the diagnostic chamber without any loss. We have

also observed increase in the beam current ($I > 10$ mA) at the DCCT with increase in microwave power. Beam spot of 80 keV, 5 mA on alumina plate located at a distance about 3 meters away from the extraction is shown in Fig. 1.2. Most of the ring type shadow around the hot spot is due to other beams and neutrals. At present we are testing the source for long term stability and beam quality improvement.

1.5. Outline of the thesis

This thesis presents the results of works carried out to settle some of the physics and technological issues related with the injection and acceleration of the space charge dominated beam in a compact proton cyclotron. The design issues of a spiral inflector, main magnet of the cyclotron and space charge effect on the behaviour of beam envelopes in the spiral inflector and cyclotron have been discussed. The analysis is performed for a 10 MeV high current compact proton cyclotron with injection energy of 80 keV and beam current in the range of 5-10 mA.

The design of the magnet for high current compact cyclotron requires special attention. The isochronous magnetic field of a compact cyclotron is mainly achieved by accurately shaping the profile of hill. A well designed magnet not only provide required isochronous magnetic field for the beam up to the extraction radius but at the same time it also provides sufficient vertical and radial focusing to the beam and avoids dangerous resonance crossing during the acceleration of the beam. In the design of the magnet one requires a special attention in the central part and optimization of the central plug to place the spiral inflector properly and provide sufficient axial focusing. The quality of the beam is mainly decided by the proper design of the central region. The basic problem in the central part of a high current compact cyclotron is that the focusing provided by the magnetic field is very low during the first few turns.

The other crucial component in the central region is the spiral inflector. Its task is to inflect the axially injected beam in the median plane and place the beam on the proper orbit without much degradation in the quality of the beam. In this regard the design of the spiral inflector and its location in the central region is very important for better centering and further acceleration of the beam in the cyclotron.

For the acceleration of high intensity beam in a cyclotron one requires careful control of particle dynamics with space charge forces of the beam in different subsystems. This is the important aspect that has been discussed in this thesis. The acceleration of high intensity beam of the order of mA in a compact cyclotron is strongly influenced by the space charge defocusing forces [36]. The study of the beam behavior in the cyclotron reveals that beam envelope behaves differently due to the coupling of the axial and radial motion arising due to space charge effects [37]. At the injection the beam must be matched to the acceptance of the central region of the cyclotron. Any mismatch causes envelope oscillations and amplitude growth of the beam during the acceleration which finally results in the loss of the beam. Careful optimization of the input beam parameters is thus required if matching conditions are to be achieved. The estimation of the radial and vertical acceptances of the cyclotron in the presence of space charge and understanding of the behavior of the beam envelopes along the accelerated orbits are also important for lossless acceleration of high intensity beam.

The spiral inflector couples the radial and axial motions of the ion and thus affects the properties of the beam. This effect is more pronounced for high intensity beams. The beam properties at the exit of the inflector strongly depend on the beam sizes and phase space orientations of the beam at the entrance of the inflector. Keeping all these facts in mind and the recent requirement of high intensity beam injection into cyclotrons motivated us to investigate the detailed beam dynamics in the spiral inflector with space charge.

A matching of beam from the ion source to the input of the spiral inflector is essential to keep the beam loss and emittance growth within acceptable limit and thus to achieve efficient beam transmission through the inflector. Numerical results show that for minimum emittance growth and less divergence in the axial direction, the input beam at the spiral inflector should be a converging non-axisymmetric with equal emittances in both the transverse planes. Thus the transformation of initially axisymmetric beam to a non-axisymmetric beam at the input of the inflector is also required. We have discussed this aspect in the final part of the thesis.

The Chapters of this thesis are laid out in the order in which the work has been completed. Chapter 2 of the thesis consists of determining the preliminary design parameters of the 10 MeV cyclotron. A hard-edge formulation and the transfer matrix technique are used. A numerical technique is developed for studying the behaviour of the beam envelope during the first turn and also to estimate the vertical acceptance of the cyclotron central region in the presence of space charge. Proper matching conditions have been found and the limit on the injected beam current has also been estimated.

In the beginning of Chapter 3, the detailed design of the magnet of the 10 MeV cyclotron is described. To optimize the pole profile of the hill of the cyclotron magnet an iterative optimization procedure based on random search technique has been developed. Here the sector shape is approximated by a polynomial function of radius. A 3D magnet code MagNet [38] is used to calculate the magnetic field in the median plane and an equilibrium orbit code GENSPEO [39] is used to obtain the betatron frequencies as a function of energy. The frequency error is minimized by optimizing the coefficients of the polynomial by using the random search technique.

The later part of Chapter 3 deals with the detailed design of the spiral inflector to be used to deflect the 80 keV proton beam into the central region of the 10 MeV cyclotron. A

computer code has been developed to solve the equations of motion for the central trajectory in the inflector using 3D magnetic field data. The parameters of the inflector are adjusted iteratively to orient the beam properly at its exit to produce a well centered beam.

The detailed study on the beam dynamics through the spiral inflector using a uniform ellipsoidal bunch with space charge effect is discussed in Chapter 4. The beam current in the bunch increases due to bunching as the beam traverses inside the spiral inflector. This is also taken into account in the analysis. The optical properties of the inflector and the behaviour of evolution of projected emittances through it have been studied using infinitesimal transfer matrix technique and sigma matrix method.

Chapter 5 presents a detailed investigation on the amplitude growth and oscillations in the beam envelopes along the accelerated orbit in the cyclotron in the presence of space charge effect using a uniform ellipsoidal bunch. The proper matching conditions are obtained by adjusting the input beam parameters to minimize the amplitude growth and oscillations. The maximum beam current that can be transported through a given focusing channel of the compact cyclotron is also estimated.

In Chapter 6 a transverse beam matching at the entrance of the spiral inflector using an elliptical solenoid is discussed. The transformation of an axisymmetric beam from the ion source to a non-axisymmetric beam at the inflector entrance which is required for better transmission can't be achieved by using solenoid magnets as used in the transport line. For this one needs either an elliptical solenoid or a quadrupole doublet. The space constraint in the transport line favours the use of elliptical solenoid.

Chapter 7 describes the major highlights of this thesis and suggests further work which can be fruitfully pursued as a direct consequence.

1.6. Summary

In this Chapter first we have presented some general overview about the cyclotron and different types of deflectors. Then we have described the 2.45 GHz microwave ion source and its injection system operating at the Variable Energy Cyclotron Centre, Kolkata. We have also presented a brief overview of the work presented in this thesis. The following Chapters describe the details of the work outlined briefly in this Chapter.

Chapter 2

Space charge effects in a compact cyclotron

2.1. Introduction

The acceleration of high-intensity beam in a cyclotron is primarily limited by the transverse and longitudinal space charge effects. The transverse space charge effect is serious at low energies near the central region and severely limits the intensity of the beam to be injected within a given acceptance. The longitudinal space charge effect, which expands the radial region occupied by the beam, is present throughout and is a major contributor to the extraction problem.

In a compact cyclotron, the vertical focusing force provided by the electromagnetic field is very weak near the center. The transverse space charge force further reduces this focusing force, which leads to an increase in the beam size, and thus sets a limit on the beam current that can be accommodated in a given aperture. This limit on the beam current depends on various factors, such as injection energy, beam emittance, available vertical aperture, vertical tune, phase acceptance in the central region etc. Several authors [25-27, 40, 41] have investigated the effect of transverse space charge in cyclotrons and obtained analytical expressions to estimate the limit on the beam current. The beam intensity limitations due to space charge and possible ways to improve it have been summarized in detail by Stammach in ref. [26]. A preliminary estimation indicates that the limiting current due to transverse space charge in a compact cyclotron can be improved by increasing the injection energy of the beam and enhancing the focusing forces by optimizing the magnet geometry of the cyclotron.

As mentioned earlier, the longitudinal space charge effect expands the radial region of the beam and causes extraction problem. In order to extract the beam with minimum losses, a clear separation of turns at the extraction radius is mandatory. This can be realized in practice in two ways. First, one can design rf resonators to stand high voltages. This reduces the number of turns and also increases the turn separation due to low energy spread at the extraction. The other way is to design the cyclotron with a large extraction radius, i.e., using a low average magnetic field.

Apart from using high injection energy, the general trend for improving the limiting current in a cyclotron is to use betatron tunes as high as possible. It is shown in ref. [36] that this procedure generally does not yield the desired result in the case of a compact cyclotron. The limiting current depends on the vertical betatron tune and the average magnetic field, and both are related to each other. An attempt to improve the vertical betatron tune by optimizing the sector geometry results in a reduction of the average magnetic field and vice versa. For a given hill and valley field, the maximum in the vertical betatron tune occurs at a lower hill angle and decreases as the hill angle is increased. The average magnetic field more or less increases linearly as the hill angle is increased. When these two parameters are optimized properly for a given hill and valley fields, one gets a maximum in the limiting current at a particular hill angle $\sim \pi / N$, where N is the number of sectors. This result gives a direction on how to choose the sector angle while working on the design optimization of a compact cyclotron.

In most of the works mentioned above, results are based on the assumptions that the magnet of the cyclotron is a uniform focusing channel, the available geometrical aperture is completely filled with a beam of uniform density, and there is no coupling between the vertical and horizontal motions. These assumptions are crude and, in general, due to envelope oscillations, the aperture is never filled. The space charge term in the envelope

equations couples the two motions. Though, the above-mentioned results are very useful for having an initial estimate, a more detailed study incorporating the coupling of the two betatron motions is necessary for finding out the optimum initial beam parameters.

In this Chapter first, the analytical formulations used for obtaining the shape of the magnet sectors are outlined. These formulations are then used to study the behavior of space charge dominated beam during the first turn in the 10 MeV compact cyclotron. The change in beam envelopes has been studied by changing the current, initial width, divergence and emittance of the beam. It is tried to find out the proper matching conditions and the estimation of the limit on the beam current that can be injected. In addition, the dependence of the limiting current on various beam-related parameters has also been studied.

2.2. Method of simulation

In this section, analytical formulations used for obtaining the shape of the magnet sectors are outlined. The preliminary design parameters of the cyclotron have been obtained using the hard-edge formulations [17] and the transfer matrix technique [42]. Since the vertical focusing frequency is quite sensitive to the fringe field at the hill-valley boundary, we have modified the classical hard-edge formula to include the soft-edge effect. The flaring and edge effects have been introduced by using thin lenses at each hill-valley boundary. In the following sub-sections, we briefly outline the analytical expressions used for computing the properties of the equilibrium orbit, betatron tunes and beam envelopes in the compact cyclotron.

2.2.1. Cyclotron parameters

Consider an N sector compact cyclotron with magnetic fields B_H and B_V in the hill and valley respectively. Let the angular widths of hill and valley be η_0 and ξ_0 on an

equilibrium orbit, and the corresponding angles of turning of orbits be η and ξ with radius of curvature ρ_H and ρ_V , respectively. The geometry of an equilibrium orbit for one sector is shown in Fig. 2.1. For a particle of charge q , mass m , and momentum p , following relations hold:

$$p = q\rho_H B_H = q\rho_V B_V \quad (2.1)$$

$$R \sin\left(\frac{\eta_0}{2}\right) = \rho_H \sin\left(\frac{\eta}{2}\right) \quad (2.2)$$

$$R \sin\left(\frac{\xi_0}{2}\right) = \rho_V \sin\left(\frac{\xi}{2}\right) \quad (2.3)$$

$$\eta_0 + \xi_0 = \eta + \xi = \frac{2\pi}{N} \quad (2.4)$$

Here R is the distance between the machine centre and the point on the orbit at the hill-valley boundary. By choosing a central field B_C and using the isochronous condition that the period of one revolution be constant, i.e.

$$N \frac{\rho_H \eta + \rho_V \xi}{v} = \frac{2\pi m}{qB_C} = \text{cont.} \quad (2.5)$$

and using simple algebra, one can easily get expressions for angles η and ξ as

$$\eta = \frac{B_H B_V}{B_H - B_V} \cdot \frac{2\pi}{N} \cdot \left(\frac{1}{B_V} - \frac{1}{\gamma B_C} \right), \quad \xi = \frac{2\pi}{N} - \eta \quad (2.6)$$

where γ is the usual relativistic term and v is the velocity of the particle. Using relations of Eqs. (2.1)-(2.5), it is straight forward to obtain relations between angles η_0 and ξ_0 as

$$\cot\left(\frac{\eta_0}{2}\right) = \cot\left(\frac{\pi}{N}\right) + \frac{B_H}{B_V} \left(\cot\left(\frac{\eta}{2}\right) - \cot\left(\frac{\pi}{N}\right) \right), \quad \xi_0 = \frac{2\pi}{N} - \eta_0 \quad (2.7)$$

The entry and exit angles to the hill (which becomes exit and entry angle for valley) are

$$\beta_1 = \varepsilon_1 + \frac{\eta - \eta_0}{2}, \quad \beta_2 = \varepsilon_2 - \frac{\eta - \eta_0}{2} \quad (2.8)$$

Here ε_1 is the spiral angle at the entry of the hill and can be chosen as desired to optimize a special design. The effective spiral angle ε_2 at the exit of the hill, which includes spiral angle as well as flaring effect, can be obtained using the relation

$$\tan \varepsilon_2 = \tan \varepsilon_1 + R \cdot \frac{d\eta_0}{d\gamma} \cdot \frac{d\gamma}{dR} \quad (2.9)$$

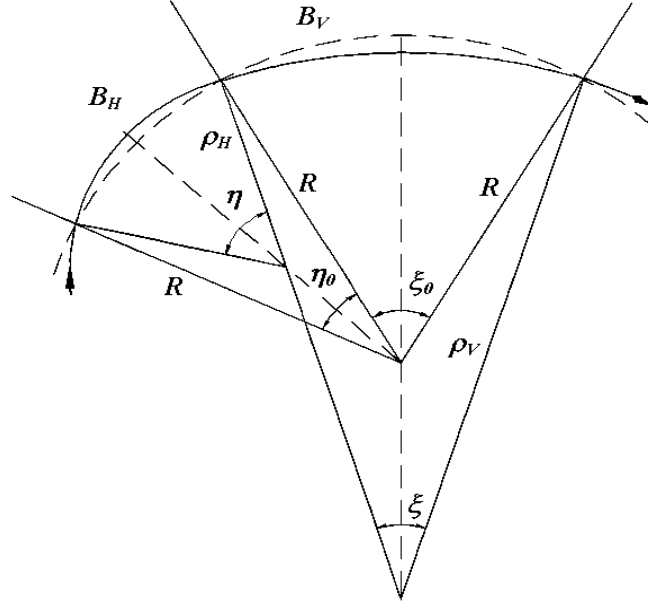


Fig. 2.1. Orbit section in one period of magnetic field consisting of a hill and a valley.

The second term of Eq. (2.9) can be obtained by performing a simple differentiation and algebraic manipulations using Eqs. (2.2), (2.3) and (2.6). We have introduced the correction term for fringing fields (soft edge effect) [43] by replacing ϕ_1 and ϕ_2 in the case of the vertical motion by

$$\phi_1^* = \phi_1 - \psi_1, \quad \phi_2^* = \phi_2 + \psi_2 \quad (2.10)$$

where,

$$\psi_{1,2} = K_1 \cdot \frac{g}{\rho} \left(\frac{1 + \sin^2 \phi_{1,2}}{\cos \phi_{1,2}} \right) \cdot \left(1 - K_1 K_2 \cdot \frac{g}{\rho} \cdot \tan \phi_{1,2} \right) \quad (2.11)$$

Here g and ρ represent the hill gap and radius of curvature of the particle in the hill when ϕ_1 and ϕ_2 are used for entry and exit angles for the hill respectively. When ϕ_1 and

ϕ_2 are used for valley, g and ρ represent the valley gap and radius of curvature of the particle in the valley, respectively. K_1 and K_2 are constants and have different values for different types fringing field boundaries [43].

2.2.2. Betatron tunes

We have used the well-known matrix method to estimate the radial and vertical betatron tunes ν_x and ν_y . Here hills and valleys are treated as bending magnets of lengths $\eta\rho_H$ and $\xi\rho_V$ having focusing strengths of $1/\rho_H$ and $1/\rho_V$ respectively. The flaring and edge effects are introduced by using thin lens matrices at each hill-valley boundary. The transfer matrices \mathbf{H}_R and \mathbf{H}_V for horizontal and vertical motions in hill are given by

$$\mathbf{H}_R = \begin{pmatrix} 1 & 0 \\ -\tan\phi_2/\rho_H & 1 \end{pmatrix} \begin{pmatrix} \cos\eta & \rho_H \sin\eta \\ -\sin\eta/\rho_H & \cos\eta \end{pmatrix} \begin{pmatrix} 1 & 0 \\ \tan\phi_1/\rho_H & 1 \end{pmatrix} \quad (2.12)$$

$$\mathbf{H}_V = \begin{pmatrix} 1 & 0 \\ \tan\phi_2^*/\rho_H & 1 \end{pmatrix} \begin{pmatrix} 1 & \eta\rho_H \\ 0 & 1 \end{pmatrix} \begin{pmatrix} 1 & 0 \\ -\tan\phi_1^*/\rho_H & 1 \end{pmatrix} \quad (2.13)$$

The transfer matrices \mathbf{V}_R and \mathbf{V}_V for horizontal and vertical motions in valley will be similar and can be obtained by replacing $\eta \rightarrow \xi$, $\rho_H \rightarrow \rho_V$, $\phi_1 \rightarrow \phi_2$, and $\phi_2 \rightarrow \phi_1$, in Eqs. (2.12) and (2.13). The radial and vertical betatron tunes ν_x and ν_y can be obtained from the expressions:

$$\nu_x = \frac{N}{2\pi} \cos^{-1} \left[\frac{1}{2} \text{Tr}(\mathbf{V}_R \cdot \mathbf{H}_R) \right] \quad (2.14)$$

$$\nu_y = \frac{N}{2\pi} \cos^{-1} \left[\frac{1}{2} \text{Tr}(\mathbf{V}_V \cdot \mathbf{H}_V) \right] \quad (2.15)$$

We have obtained the shape of the magnet and properties of the equilibrium orbit using an iterative process. Care has been taken to keep betatron tunes ν_x and ν_y sufficiently away from the resonance. It should be noted here that all η , η_0 , ξ , ξ_0 , ρ_H , ρ_V , R etc. are the function of beam energy and constant for a given equilibrium orbit. After acceleration,

particles move to new equilibrium orbit and therefore, all the parameters mentioned above assume new values.

2.2.3. Beam envelopes

In order to obtain the beam envelope $X(s)$ in the horizontal plane and $Y(s)$ in the vertical plane, where s being the distance along the equilibrium orbit, we have solved numerically the following coupled envelope equations [44]

$$X'' + k_x^2 X - \frac{4I}{(X+Y)I_0\beta^3\gamma^3} \cdot \frac{2\pi}{\Delta\phi} - \frac{\varepsilon_x^2}{X^3} = 0 \quad (2.16)$$

$$Y'' - \frac{4I}{(X+Y)I_0\beta^3\gamma^3} \cdot \frac{2\pi}{\Delta\phi} - \frac{\varepsilon_y^2}{Y^3} = 0 \quad (2.17)$$

where, k_x is the well-known focusing strength of magnets (hill or valley) in horizontal direction ($=\rho^{-1}$). The term $(2\pi/\Delta\phi)$ is included with the beam current I to account for the beam phase width accepted in the central region. $I_0 = 4\pi\varepsilon_0 mc^3/q$, with m/q being mass/charge ratio of the particle and is known as the characteristic current and for proton, $I_0 = 31$ MA. ε_x and ε_y are the beam emittance in the x and y planes respectively and β and γ are the usual relativistic parameters. We have included the acceleration effect of two resonators in the opposite valleys by approximating them with four step-function accelerating gaps. Equations (2.16) and (2.17) have been solved numerically in the hill magnet and the valley magnet to obtain X , X' and Y , Y' . At each hill valley boundary, X and X' obtained from the solutions have been converted to the well known twiss parameters α_x , β_x and γ_x using the following relations:

$$\beta_x = \frac{X^2}{\varepsilon_x}, \quad \alpha_x = -\frac{XX'}{\varepsilon_x}, \quad \gamma_x = \frac{1+\alpha_x^2}{\beta_x} \quad (2.18)$$

These twiss parameters are then transformed to new values by the thin-lens matrices \mathbf{R} , which include the effect of edge, flaring and soft edge:

$$\mathbf{J}_2 = \mathbf{R} \cdot \mathbf{J}_1 \cdot \mathbf{R}^{-1}, \quad \mathbf{J} = \begin{bmatrix} \alpha_x & \beta_x \\ -\alpha_x & -\gamma_x \end{bmatrix}, \quad \mathbf{R} = \begin{bmatrix} 1 & 0 \\ \tan \phi / \rho & 1 \end{bmatrix} \quad (2.19)$$

Here \mathbf{J}_1 and \mathbf{J}_2 stand for the initial and final matrices containing twiss parameters, respectively. We can easily obtain the lens matrix \mathbf{R} for horizontal and vertical motions at the entry of a hill by using $\phi = \phi_1$ and $\phi = -\phi_1$, and at the exit from a hill by using $\phi = -\phi_2$ and $\phi = \phi_2$, respectively. In the case of motions at the entry and exit of a valley, we need to replace $\phi_1 \rightarrow \phi_2$, and $\phi_2 \rightarrow \phi_1$. The radius of curvature $\rho = \rho_H$ for the hill, and $\rho = \rho_V$ for the valley. The final twiss parameters obtained from \mathbf{J}_2 and the relations of Eq. (2.18) have been used to get back X and X' for further calculations. Similar expressions have been used for y -plane also. Since the slope of the envelope reduces with the acceleration, we have modified X' and Y' suitably at each accelerating gap by multiplying them with the ratio of old $\beta\gamma$ to the new $\beta\gamma$.

2.3. Numerical results and discussions

In this section, we present the results of preliminary design studies of our 10 MeV compact cyclotron and discuss the results of numerical simulation carried out for studying the behavior of the beam envelopes during the injection [37].

2.3.1. Preliminary design of the 10 MeV magnet

A hard-edge approximation and the transfer matrix technique developed in the previous section have been used to determine the magnet shape. A linear drop-off of the field model has been used for the fringe field using the value for the fringe field integrals K_1 and K_2 equal to 1/6 and 3.8, respectively [43]. Figure 2.2 shows the magnet sector

geometry and radial and vertical betatron tunes as a function of beam energy. The important design parameters (preliminary design) are listed in Table 2.1.

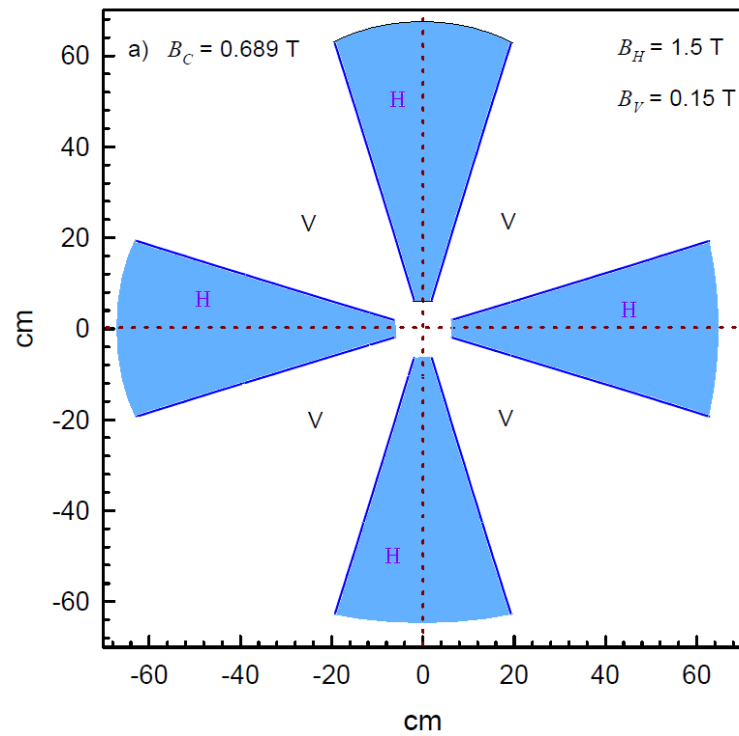


Fig. 2.2(a). A schematic of sector geometry obtained using the hard-edge formulations and the transfer matrix technique.

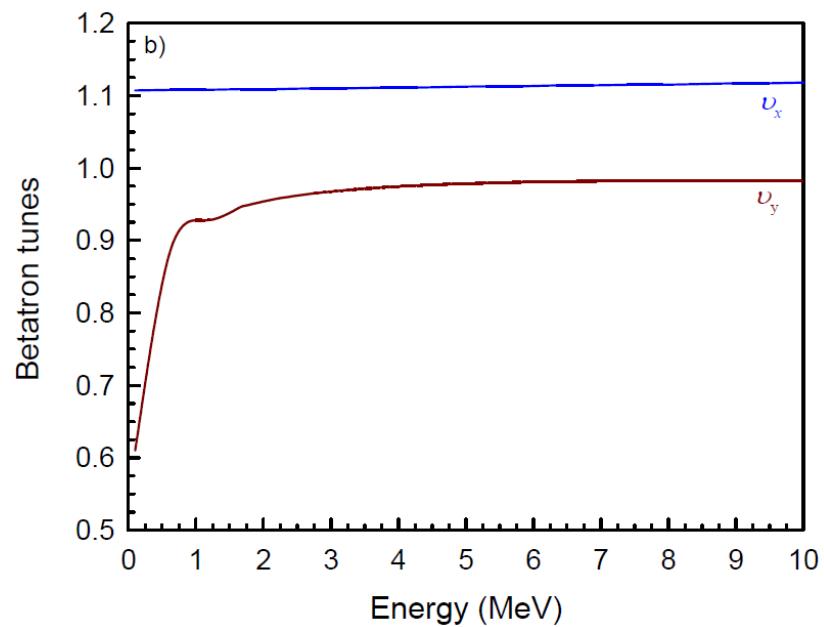


Fig. 2.2(b). Radial and vertical betatron tunes as a function of beam energy.

Table 2.1

Parameters of the 10 MeV compact cyclotron

Parameters	Values
Injection energy	100 keV
Final energy	10 MeV
Hill field B_H	1.5 T
Valley field B_V	0.15 T
Hill gap	4 cm
Valley gap	46 cm
Max. hill angle	34.2°
No. of resonators	2
Injection radius	6.6 cm
Radial tune ν_x	1.1-1.2
Vertical tune ν_y	0.61-.99

2.3.2. Transverse space charge effect and limiting current

In order to study the behavior of the space charge dominated beam during the first turn in the 10 MeV cyclotron a computer code is written to solve the differential equations (2.16) and (2.17). We have used step size equal to 0.1 mm in the numerical calculation. Microwave ion sources operating at different labs produce several mA of proton beam with normalized emittance varying between 0.4 to 1.0π mm mrad [45]. We have used same values for the normalized emittance $\varepsilon_n = \beta\gamma \varepsilon = 0.8 \pi$ mm mrad in both the planes which corresponds to total emittance of 53.4π mm mrad at 100 keV injection energy. The phase acceptance $\Delta\phi$ in the central region of a cyclotron varies between 20° to 40° of rf [46]. In the present work we have assumed $\Delta\phi = 30^\circ$ of rf.

Figure 2.3(a) shows the behavior of the beam envelopes with distance s along the equilibrium orbit at an injection radius of 6.6 cm. In this case, there is no acceleration and the beam current $I = 0$ mA. The term zero beam current ($I = 0$ mA) throughout the thesis, has been used to indicate low beam current where the space charge effect is negligible. We can clearly see the periodicity in the envelope oscillations and it is straightforward to find out the matched initial phase ellipses analytically.

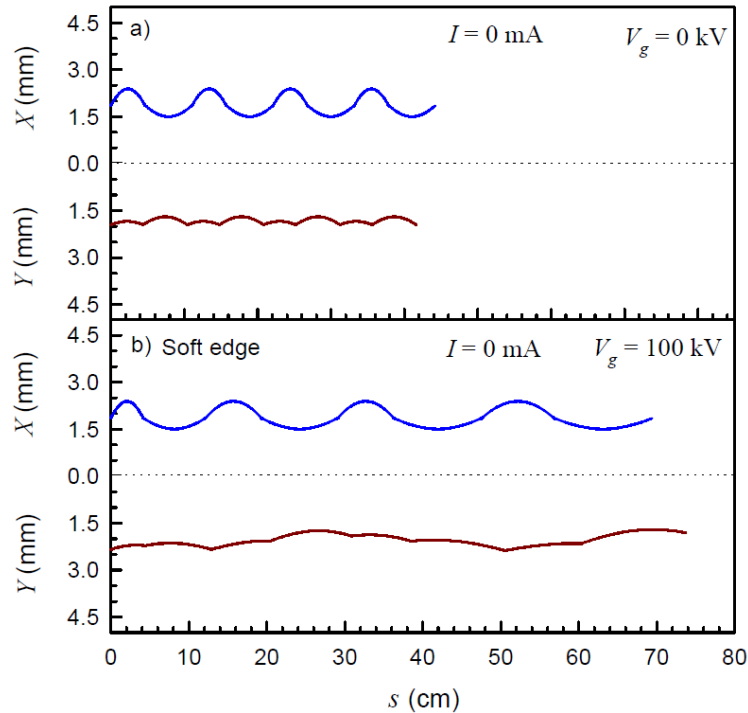


Fig. 2.3. Behavior of beam envelopes in the radial and vertical directions with distance s along the equilibrium orbit for the first turn with zero beam current: (a) no acceleration, (b) accelerations and soft-edge effects. Normalized emittance $\varepsilon_n = 0.8 \pi$ mm mrad in both the transverse planes.

Figure 2.3(b) shows the envelopes with acceleration and soft-edge effects. As indicated earlier, the acceleration has been introduced using four gaps, each having 100 kV and located in two opposite valleys. We have chosen the starting point at the entry of a hill; the first two acceleration gaps are at the beginning and at the end of the first valley and the other two gaps are in the third valley. One can see the lack of periodicity in the envelope oscillations due to the increase in the path length and slight reduction in the

amplitude caused by acceleration. The introduction of the soft edge has not only increased the envelope amplitude but also added an extra oscillation in the axial envelope. It is easy to see from Fig. 2.3 that at low beam intensity the average amplitude of the beam envelope is limited to ~ 2.2 mm in both planes. The transverse space charge effect leads to an increase in the beam size. In order to have a comparative study, we have restricted the maximum envelope amplitude to 5 mm in both planes in our further analysis.

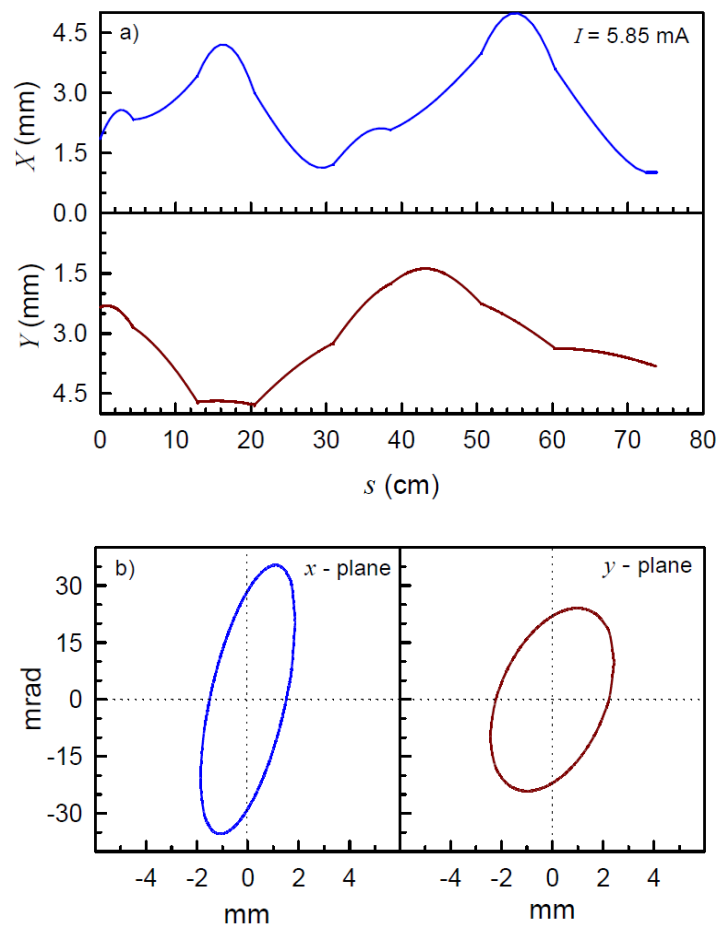


Fig. 2.4. Results of numerical calculations: (a) beam envelopes in the radial and vertical directions with accelerations, soft-edge effects and $I = 5.85$ mA. Envelope amplitude is restricted to ≤ 5 mm in both planes, (b) phase ellipses in the radial and vertical directions used as initial condition. These are the matched ellipses (Fig. 2.2(a)) with $I = 0$ mA.

Figure 2.4(a) shows the beam envelope with the same initial conditions as those of the matched conditions ($I = 0$ mA) used in Fig. 2.3(a), when the injected beam current $I = 5.85$ mA. The matched phase ellipses are shown in Fig. 2.4(b). It is clear that these

initial conditions are not at all suitable for injection in the case of space charge dominated beams, because best aperture filling does not occur in this case. It is well known that a beam matched to the periodic system has minimum envelope oscillations. However, in the case of the space charge dominated beams, it is difficult to find out the matched envelope analytically and one has to resort to numerical techniques.

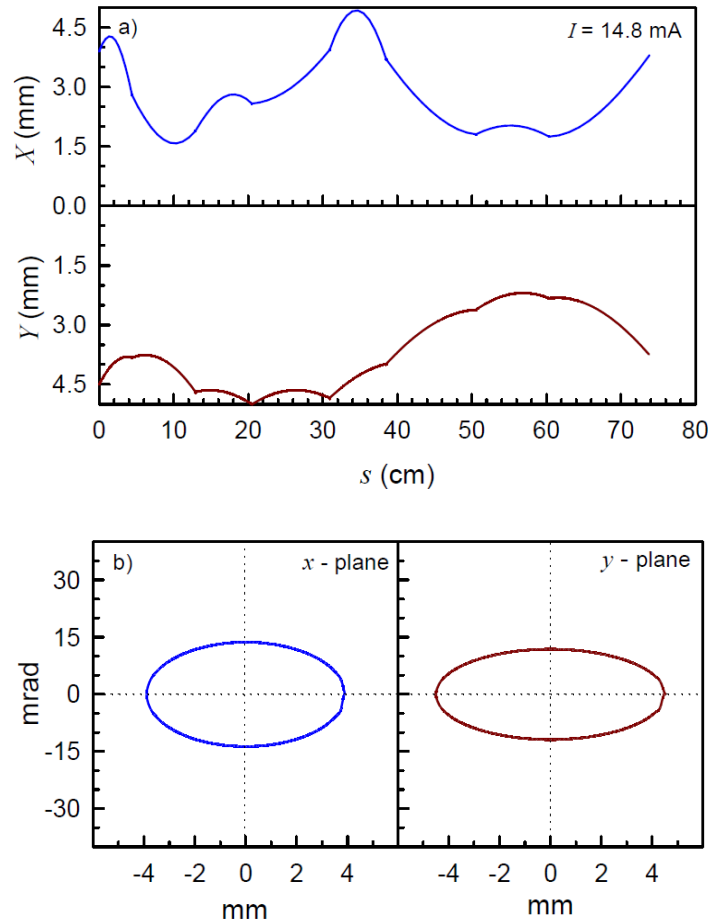


Fig. 2.5. Results of optimization: (a) beam envelopes with amplitude ≤ 5 mm in the radial and vertical planes, optimized using upright phase ellipses in both planes, (b) upright beam ellipses with normalized emittance $\varepsilon_n = 0.8 \pi$ mm mrad in both planes.

Figure 2.5(a) shows the beam envelopes optimized using initial up-right ellipses, i.e. $\alpha_x = \alpha_y = 0$. These ellipses are shown in Fig. 2.5(b). As indicated in the figure, the injected beam current is improved substantially to 14.8 mA in this case. We have also tried to optimize the beam envelopes using tilted ellipses as initial conditions. Results of

optimization are as shown in Figs. 2.6(a) and (b). One can notice a marginal increase in the beam current (15.8 mA) within the 5 mm half aperture.

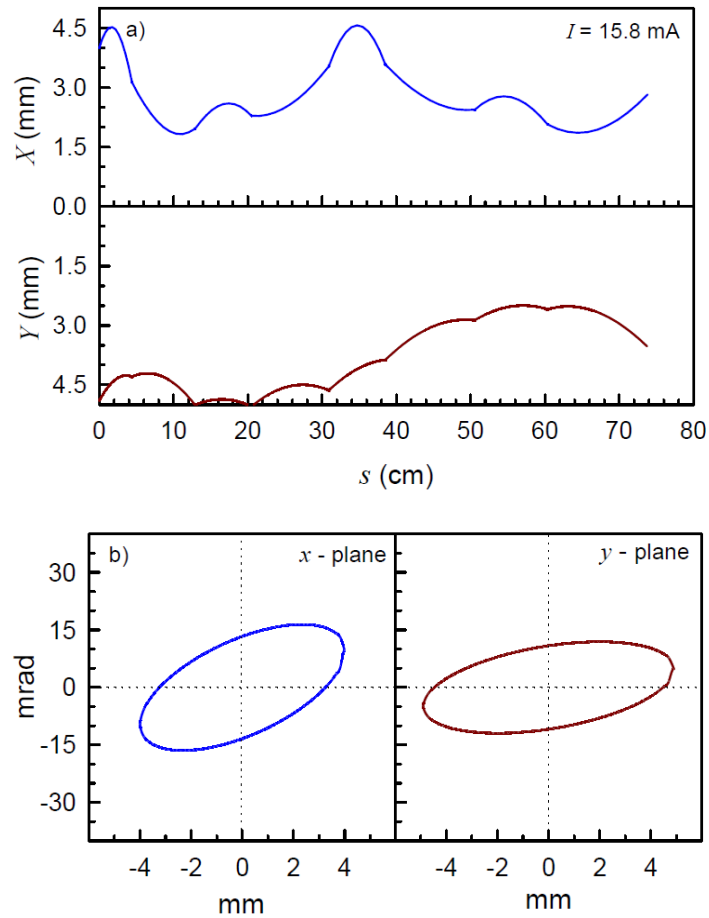


Fig. 2.6. Beam envelopes in the radial and axial planes optimized with tilted phase ellipses to accommodate more beam current (15.8 mA). (a) Beam envelopes with amplitudes ≤ 5 mm, and (b) phase ellipses with normalized emittance $\varepsilon_n = 0.8 \pi$ mm mrad in both planes.

As stated earlier the proton beam from 2.45 GHz microwave ion source will be injected into the central region of the 10 MeV compact proton cyclotron. The ion source is presently under testing for beam characterization. During the testing of the source it is observed that ion source is more stable and reliable against sparks and electric discharge in the extraction region when operated with extraction voltage near 80-85 keV. So we have repeated the simulation with injection energy of 80 keV also. In order to have large turn separation at the extraction and to reduce the number of turns to obtain the final energy we

have now chosen the dee voltage $V_g = 125$ kV. **Figure 2.7** shows the simulation results of beam envelopes in the radial and axial planes optimized with tilted phase ellipses. It has been found that with decrease in the injection energy the limiting current is also decreased to a value of 13.6 mA within the specified 5 mm half aperture sizes in both the planes.

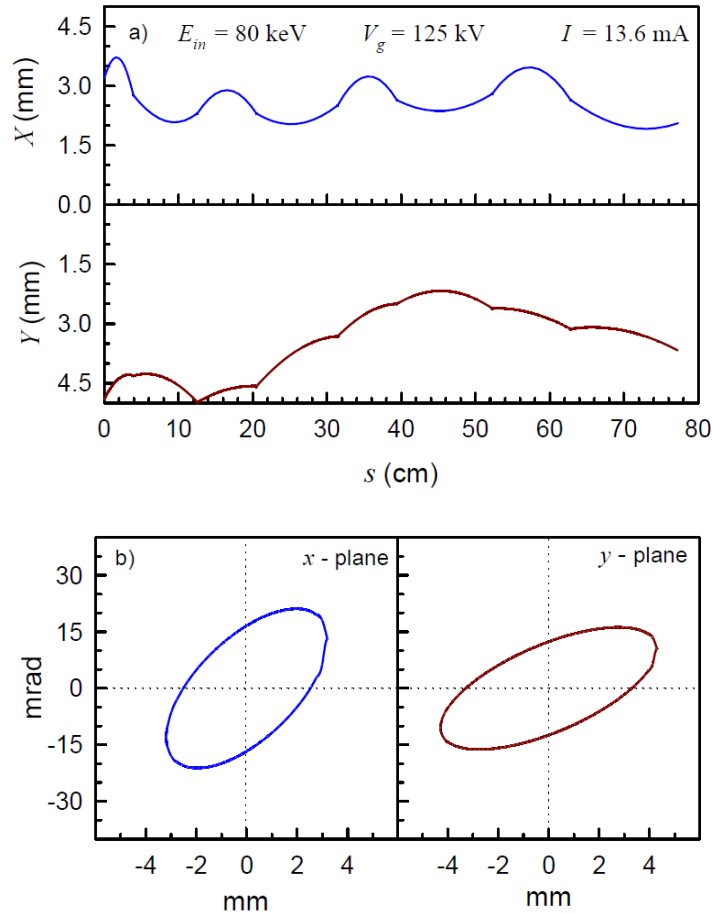


Fig. 2.7. Simulation results of beam envelopes in the radial and axial planes at injection energy of 80 keV and acceleration voltage 125 kV (a) Beam envelopes with amplitudes ≤ 5 mm, and (b) phase ellipses with emittance $\varepsilon_n = 0.8 \pi$ mm mrad in both planes.

2.3.3. Effect of input conditions on limiting current

We have also studied the behavior of beam envelopes with different starting conditions and accelerating voltages. It has been observed during optimization that there is a particular set of initial parameters for a given beam current that gives the optimum beam envelope. An optimized set of initial parameters of phase ellipses X , X' and Y , Y' for a

given beam current (say 14.8 mA) is not at all suitable for other beam currents (say 10 mA). We observed that a change in the accelerating voltage from 100 to 50 kV reduces the limiting beam current marginally (0.25 mA) in the matched condition, whereas this reduction is substantial in the case of the optimized condition (2.2 mA). We believe that these effects are due to the coupling between x and y motions via space charge term.

Figure 2.8 shows the variation of the maximum beam current confined within a half-aperture of 5 mm in both horizontal and vertical planes, as a function of the injection energy and the beam emittance. As expected, the limiting current increases with the injection energy and reduces if the emittance is increased. Clearly, a beam with low emittance $\sim 0.8 \pi$ mm mrad and injection energy in the range of 80-100 keV appear reasonable for the injection of 10 mA beam current (theoretical limiting value ~ 15 mA) in the compact cyclotron.

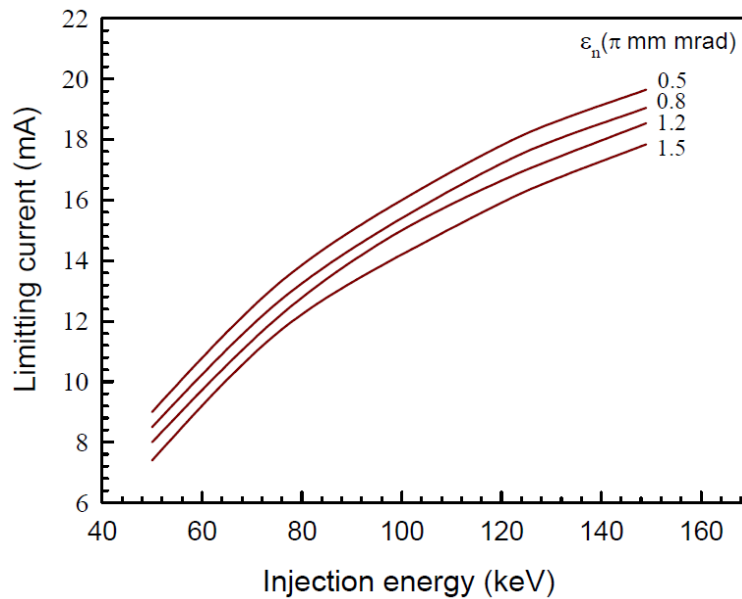


Fig. 2.8. Variation of limiting current as a function of injection energy for various values of beam emittance. In all cases the half aperture is restricted to 5 mm in both the planes.

2.3.4. Longitudinal space charge effect and turn separations

Although the work presented in this Chapter is mainly devoted to the transverse space charge effect, we would also like to mention the results of preliminary calculations for the

turn separation and the energy spread produced by the longitudinal space charge effect at the extraction. As indicated earlier, acceleration to the beam will be provided by two resonators (delta type) located in the opposite valleys. They will be designed to provide an accelerating voltage of 100 kV at the injection, which will increase gradually up to 200 kV at the extraction. With an accelerating voltage of 200 kV and v_x equal to 0.9, we get a radial gain per turn equal to ~ 32 mm and an effective turn separation of ~ 14 mm at the extraction for a beam having a phase width equal to 30° of rf and a radial width of ~ 10 mm at the injection. For estimating the effect of longitudinal space charge, we have used the following simple formula for the energy spread due to longitudinal space charge after n turns. The formula is valid for separated turns and is given by [47]

$$\Delta U_{sp} = \frac{2nI}{\epsilon_0 a \Delta\phi f_{rf}} \ln(1 + \sqrt{2}) \quad (2.20)$$

where I is the average beam current, $2a$ is the transverse beam diameter, and f_{rf} is the rf frequency. Using an average value of ~ 150 kV for the accelerating voltage at each gap and 42 MHz for the rf, one obtains an energy spread of ~ 300 keV for 10 mA beam at 10 MeV. Since the space charge induced energy spread is smaller than the energy gain per turn, turns will remain separated at the extraction. Assuming that the total longitudinal space charge energy spread is equal to half of the energy gain per turn, the average beam intensity limit due to longitudinal space charge comes out to be ~ 19.7 mA at 10 MeV.

We would like to point out here that the results presented here are valid when the injection energy is sufficiently high in the range of 80-200 keV and the average magnetic field is low (which is the case when one uses the deep valley concept to provide large flutter). These results are not applicable for the small injection radius (compared to the pole gap in the hill region), i.e. for the low injection energy in the region of 10-20 keV and

the high average magnetic field in the range of 1.5-1.8 Tesla. Here the injection radius as well as flutter becomes very small. The hard-edge analytical relations together with the estimation of fringe field using thin-lens matrices used by us are not valid in this region.

2.4. Summary

In this Chapter, we have studied the behavior of the space charge dominated beam envelopes during the injection in a compact cyclotron. We have studied the change in the beam envelopes by changing the current and other parameters of the injected beam and estimated the limit on the beam current that can be injected. The dependence of the limiting current on various machine and beam related parameters have also been studied. In addition, we have described a method for improving the limit of the beam current that can be injected into a compact isochronous cyclotron. A procedure of optimizing beam parameters in a given acceptance in the presence of space charge force is also presented. Results of this work will be helpful in choosing the geometry of the magnet for a high-current compact cyclotron during the initial design stage before a more complicated and refined optimization program is taken up.

Chapter 3

Design of magnet and spiral inflector for 10 MeV compact cyclotron

3.1. Introduction

In this Chapter first we describe the design of the magnet of 10 MeV compact cyclotron carried out using 3D code and an optimization technique. Then we present the detail design procedure of the spiral inflector using the computed magnetic field data.

One of the central problems for isochronous cyclotrons is to obtain a desired radial field profile for a constant period of ion revolution. The isochronous magnetic field of compact cyclotron is mainly achieved by accurately shaping the profile of hill. The deviation between the achieved magnetic field and the required isochronous field should be within an acceptable limit of 1 in 10^4 . Well designed sector shape, not only minimizes the phase slip of the beam with respect to rf but at the same time, provides sufficient vertical and radial focusing to the beam.

Analytical formulas available in the literature do not predict the correct values of hill angle and betatron tunes at lower radii in the case of a compact cyclotron particularly in the cases where hill gap is small and valley gap is large. The fringe field effects are no longer negligible in such cases. Hence a 3D code, together with an equilibrium orbit code, becomes necessary to obtain the correct shape of sectors. This involves a lengthy iterative procedure to determine the hill angle at a large number of radii.

There is no simple method available in the literature for the iterative shimming and quick optimization of the sector geometry. Papash et al. [48] proposed an algorithm for shimming of the hill using analytical formulas. However, their method is valid only for

low flutter field. Qin et al. [49] used a method based on least square fitting of the multiple linear regression model of the magnet pole shimming vector related to isochronous field formation. For this, they used the data of isochronous field error due to small change in hill angle at some discrete radial points. The sector shape at each iteration was controlled by changing the hill angles at these locations. In this method, for a better accuracy, one has to use a large number of hill data points. So it takes large computation time because initially one has to run the 3D code for each data point to generate the correlation matrix.

In this Chapter the design procedure of main magnet of the 10 MeV high current compact proton cyclotron has been discussed. We have proposed a shimming method, which gives smooth sector geometry of the hill. Using the computed magnetic field we have then discussed the design of a spiral inflector which will be used to inflect the 80 keV proton beam into the central region of the cyclotron. A computer code has been developed to solve the equations of motion for the central ion trajectory. The parameters of the inflector are adjusted iteratively to produce a well centered beam. The orbit centering of the inflected beam is checked by using the central region code.

3.2. Cyclotron magnet design

In this section we briefly outline the formulations used for optimizing the sector geometry [8]. We have used a 3D magnetic field code MagNet [38] to calculate the field in the median plane and have obtained the frequency errors as a function of energy using equilibrium orbit code GENSPEO [39]. These frequency errors are then minimized by modifying the sector geometry.

3.2.1. Optimization with Random search method

Consider a N sector cyclotron with constant magnetic fields B_H and B_V in the hill and valley respectively. Let $\eta(r)$ and $\xi(r)$ define the hill and valley angles, respectively, at an

average radius r . Using hard edge approximation for the sectors, we can write the following relations:

$$\eta(r) + \xi(r) = \frac{2\pi}{N} \quad \bar{B}(r) = \frac{\eta(r)B_H + \xi(r)B_V}{\eta(r) + \xi(r)} \quad \bar{B}(r) = \frac{B_C}{\sqrt{1-ar^2}} \quad (3.1)$$

where B_C is the isochronous field at the center of the cyclotron and $a = (qB_C / mc)^2$.

Using Eqs. (3.1) we can write

$$\eta(r) = \frac{2\pi}{N(B_H - B_V)} \left[\frac{B_C}{\sqrt{1-ar^2}} - B_V \right] \quad (3.2)$$

Expanding the square root term in the above equation we get

$$\eta(r) = \frac{2\pi}{N(B_H - B_V)} \left[B_C \left(1 + \frac{1}{2}ar^2 + \frac{3}{4}a^2r^4 + \frac{15}{16}a^3r^6 + \dots \right) - B_V \right] \quad (3.3)$$

The above equation shows that the hill angle $\eta(r)$ is a polynomial function of r^2 for constant hill and valley fields. We can see that the coefficients of the above equation are known in terms of the parameter a and it is very easy to get required $\eta(r)$ at different radii. However, in real situation, hill and valley magnetic fields are not constant due to fringe field effects and are function of both r and azimuthal angle. As a result, the coefficients of the polynomial in Eq. (3.3) for $\eta(r)$ will be different. These are then to be found out by the iterative approach as mentioned earlier. We approximate the form of the hill angle to be a polynomial of degree m in r^2 as

$$\eta(r) = a_0 + a_1r^2 + a_2r^4 + a_3r^6 + a_4r^8 + \dots + a_m r^{2m} \quad (3.4)$$

It is obvious that the polynomial coefficients a_0, a_1 etc. depend on the hill and valley fields, in addition to the final beam energy. One can start with a given set of a_n values, and iteratively correct these to obtain the final optimized hill angle. For initial model one can choose a hill profile as given by Eq. (3.3); however, any reasonable profile of hill including a constant hill angle can be used. The first step in the present method is to

calculate the z -component of the magnetic field $B(r, \theta, z = 0)$ at the median plane for the initial sector geometry and obtain the frequency errors at different energies. The frequency error is defined as

$$\Omega(k) = \frac{\omega_0}{\omega(E_k)} - 1 \quad (3.5)$$

where $k = 1, 2, \dots, n$ denotes the energy steps, ω_0 is the constant rotation frequency of the particle for isochronous field and $\omega(E_k)$ is the rotation frequency of the particle at energy E_k for the calculated magnetic field with the assumed sector shape. The magnitude of frequency errors greater than the specified tolerance limit means the magnetic field is different from the required isochronous field and hence it needs to be corrected by modifying the sector shape.

The second step involves the calculation of the elements of the $n \times (m + 1)$ correlation matrix. For this it is required to calculate the magnetic field by slightly changing the sector shape with a very small change in one of the coefficients, say $a_i = a_i + \Delta a_i$, of the polynomial keeping all other coefficients and geometry constant. The same procedure is repeated for all other coefficients one by one. The small deviation in frequency errors $\Delta\Omega(1), \Delta\Omega(2), \dots, \Delta\Omega(n)$ so obtained at different energy steps are related linearly as

$$\Delta\Omega(k) = \frac{\partial\Omega(k)}{\partial a_0} \Delta a_0 + \frac{\partial\Omega(k)}{\partial a_1} \Delta a_1 + \dots + \frac{\partial\Omega(k)}{\partial a_m} \Delta a_m \quad (3.6)$$

For the validity of these linear set of equations it is necessary that the perturbed values Δa_i should be very small so that the shift in the frequency errors is small and

$$\frac{\partial\Omega(k)}{\partial a_i} = \frac{\Omega(k)|_{a_i + \Delta a_i} - \Omega(k)|_{a_i}}{\Delta a_i} \quad (3.7)$$

While calculating the correlation matrix we have found that the values of the matrix elements for initial few energy values (i.e. at lower radius) are very small. So to make an

appreciable change in the elements at lower radii we have added another factor to the equation of hill angle $\eta(r)$. Now the modified hill angle becomes

$$\eta(r) = \sum_{i=0}^m a_i r^{2i} + g e^{-\alpha(r-r_0)^2} \quad (3.8)$$

Here, g is a parameter which we want to optimize for pole shimming in the central region, r_0 is the radius where we want maximum changes in the frequency error and a is a chosen constant. Further, we have included the coil current also for the optimization so the total number of parameters becomes $(m+3)$ and the size of the correlation matrix is $n \times (m+3)$. The linear set of equations can be written in the matrix form

$$\begin{bmatrix} \Delta\Omega(1) \\ \Delta\Omega(2) \\ \vdots \\ \vdots \\ \vdots \\ \vdots \\ \vdots \\ \Delta\Omega(n) \end{bmatrix} = \begin{bmatrix} \frac{\partial\Omega(1)}{\partial a_0} & \frac{\partial\Omega(1)}{\partial a_1} & \dots & \frac{\partial\Omega(1)}{\partial a_{m+2}} \\ \frac{\partial\Omega(2)}{\partial a_0} & \frac{\partial\Omega(2)}{\partial a_1} & \dots & \frac{\partial\Omega(2)}{\partial a_{m+2}} \\ \vdots & \vdots & \dots & \vdots \\ \frac{\partial\Omega(n)}{\partial a_0} & \frac{\partial\Omega(n)}{\partial a_1} & \dots & \frac{\partial\Omega(n)}{\partial a_{m+2}} \end{bmatrix} \begin{bmatrix} \Delta a_0 \\ \Delta a_1 \\ \vdots \\ \Delta a_{m+2} \end{bmatrix} \quad (3.9)$$

The optimization of the parameters a_0, a_1, \dots, a_{m+2} , has been done by random search techniques which is given below. Here parameter a_{m+1} represents the coefficient g in Eq. (3.8) and a_{m+2} is the coil current parameter.

In random search method we have minimized the frequency error of the particle by a suitable combination of all the unknown parameters. We have defined an error term R_{error} which is the sum of the squares of the estimated frequency errors accumulated over all the energy steps

$$R_{error} = \sum_{k=1}^n \left(\Omega(k) - \sum_{i=0}^{m+2} \left(a_i \frac{\partial\Omega(k)}{\partial a_i} \right) \right)^2 \quad (3.10)$$

Here $\frac{\partial \Omega(k)}{\partial a_i}$ are the elements of the correlation matrix calculated for the initial geometry.

Now the quantity R_{error} is minimized by varying the parameters a_i randomly [50]. A set of parameters is chosen randomly within a small range for a_i and R_{error} is calculated. This is done repeatedly until a small value of R_{error} is obtained. This gives an intermediate set of a_i . The process is repeated with random values chosen around the intermediate set of values. At each step the range for each parameter is decreased so that the search becomes faster. After a number of cycles of the process one obtains the minimum value of R_{error} and new values of parameters a_i . This completes one step of iteration of minimizing the frequency error. With this set of new parameters a_i , a new hill shape is obtained, and the magnetic field is calculated once again. The new frequency errors, which are smaller than those calculated with the earlier hill shape, are also determined and random search process is repeated. The iterations are continued until the frequency error falls below the required tolerance. A good feature of the random search technique is that one can easily introduce constraints in the problem. One can reject a solution if the constraints are not fulfilled. One can also put constraints that the central field should be within a pre-defined range and the betatron frequencies are in the chosen range.

3.2.2. Optimized magnet geometry

The above method has been applied to optimize the sector geometry of our 10 MeV, 5 mA compact cyclotron. The preliminary design of the magnet was obtained using analytical formulations based on hard edge approximation and matrix method [17, 37, 42, 51] discussed in Chapter 2. We have chosen the configuration of the magnet having four sectors with maximum field of 1.5 T at the hill centre. We have chosen the deep valley structure to provide strong focusing in the vertical direction. The hill gap is 5 cm and the

valley gap is 50 cm, same as the distance between the upper and lower return yokes. For the injection system, one hole is provided at the center. We have provided eight holes in the four valleys for vacuum pumps and RF cavities. Apart from using a high dee voltage (125 kV), we have chosen a low average magnetic field equal to 0.689 T (particle revolution frequency $f = 10.5$ MHz, harmonic number $h = 4$) and hence a large extraction radius of ~ 65 cm for 10 MeV cyclotron to have a reasonable turn separation at the extraction. In order to meet the isochronism, the shaping of the azimuthally averaged magnetic field was done with the help of varying the sector angular width along the radius.

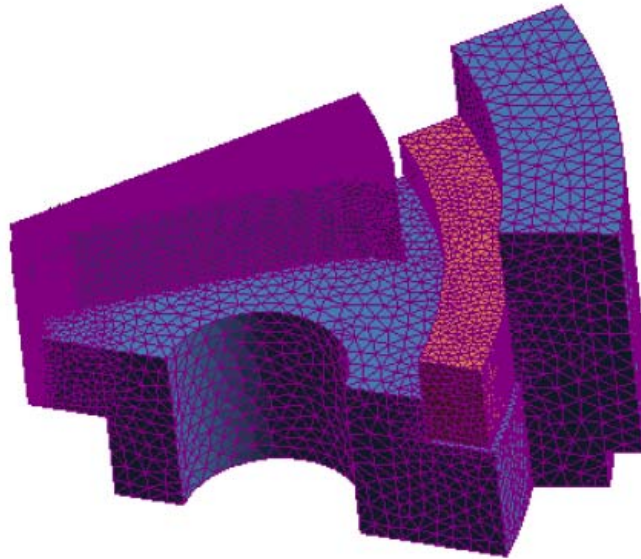


Fig. 3.1. Magnet model built in the code.

Based on the preliminary design, a 3D magnet model was established and MagNet code was utilized for the field calculation and optimization. Before starting the actual optimization we have fixed the yoke and leg thickness properly so that there is no saturation in any part of the magnet. Symmetry considerations allowed us to use only 1/16 portion of the magnet as shown in [Fig. 3.1](#). This helped us to save time for the computation of the field. In order to improve the accuracy we have divided the model into different zones appropriate with the dimension i.e., smaller mesh sizes at lower radii. The output of the magnet code was used in GENSPEO for the calculation of frequency errors

and other equilibrium orbit properties. In the optimization we have used six parameters $a_0, a_1, a_2, a_3, a_4, a_9$ from the polynomial and other two as coil current and pole shimming in the central region. The field near the extraction radius falls very sharply because of finite pole radius. Therefore the hill angle should also change rapidly to keep isochronous condition intact up to the extraction radius. For this we have used a higher order term $a_9 r^{18}$ in the polynomial which affects the field only at the extraction.

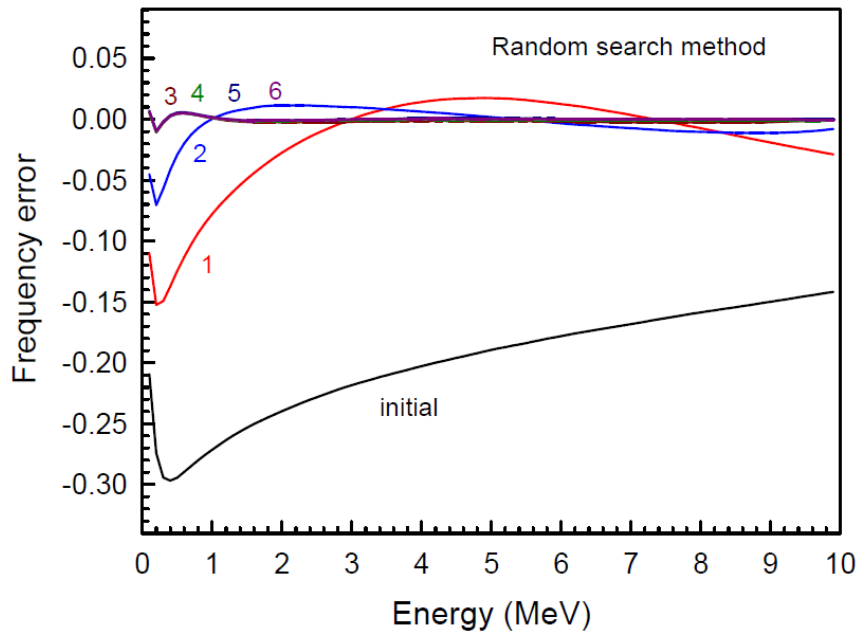


Fig. 3.2. Decrease in frequency error as a function of energy at different iterations. Here numbers 1, 2, 3... indicate the results obtained after that many iterations.

For the optimization we have started with the hill shape obtained from Eq. (3.3) and current in the coil is set equal to 500 A (turns ~ 200). The values of frequency error as a function of energy are shown in Fig. 3.2 for successive iterations. We can see that the convergence of the method is fast and frequency errors are within ± 0.02 throughout only after two iterations. After 6 iterations we have achieved the frequency error $< 10^{-4}$ at all energies. The initial and optimized values of parameters are given in Table 3.1.

Table 3.1

Initial and final optimized parameters

Parameter	Initial value	Optimised value
Coil current (A)	500	489.4
a_0	15.8	9.59
a_1	6.10^{-5}	$1.5.10^{-3}$
a_2	$4.4.10^{-10}$	$-1.51.10^{-7}$
a_3	$2.64.10^{-15}$	$-6.36.10^{-12}$
a_4	0	$1.85.10^{-15}$
a_9	0	$4.74.10^{-34}$
g	0	-2.37

Figure 3.3 shows the optimized hill shape, i.e., the hill angle as a function of radius. It is markedly different from the initially adopted hill shape, indicating the dominance of fringe field effect in the case of large difference between the hill and the valley fields.

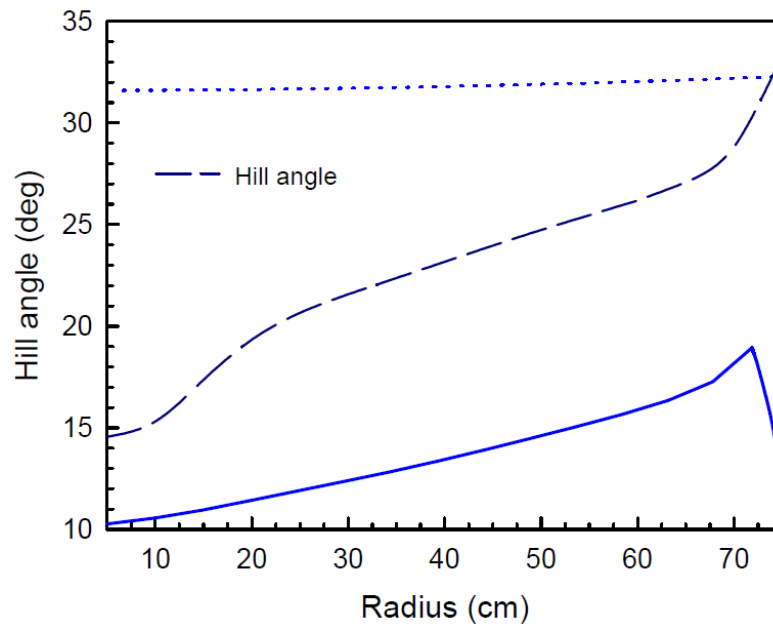


Fig. 3.3. Hill shape and hill angle optimized by random search method. Dotted curve shows the initial hill angle obtained using hard edge approximation.

Fig. 3.4(a) shows the variation of the optimized radial and axial betatron tunes as a function of energy. The dotted curve represents the analytical values. We can see that the values of axial betatron tune ν_y are greater than 0.5 throughout, except near the central region. Fig. 3.4(b) shows the optimized average magnetic field and required isochronous magnetic field (dotted). The variation of the integrated phase slip $\sin\phi$ is shown in Fig. 3.4(c). It shows that the phase excursion in the entire region is limited within ± 2 deg. The optimized parameters of the 10 MeV cyclotron are listed in Table 3.2.

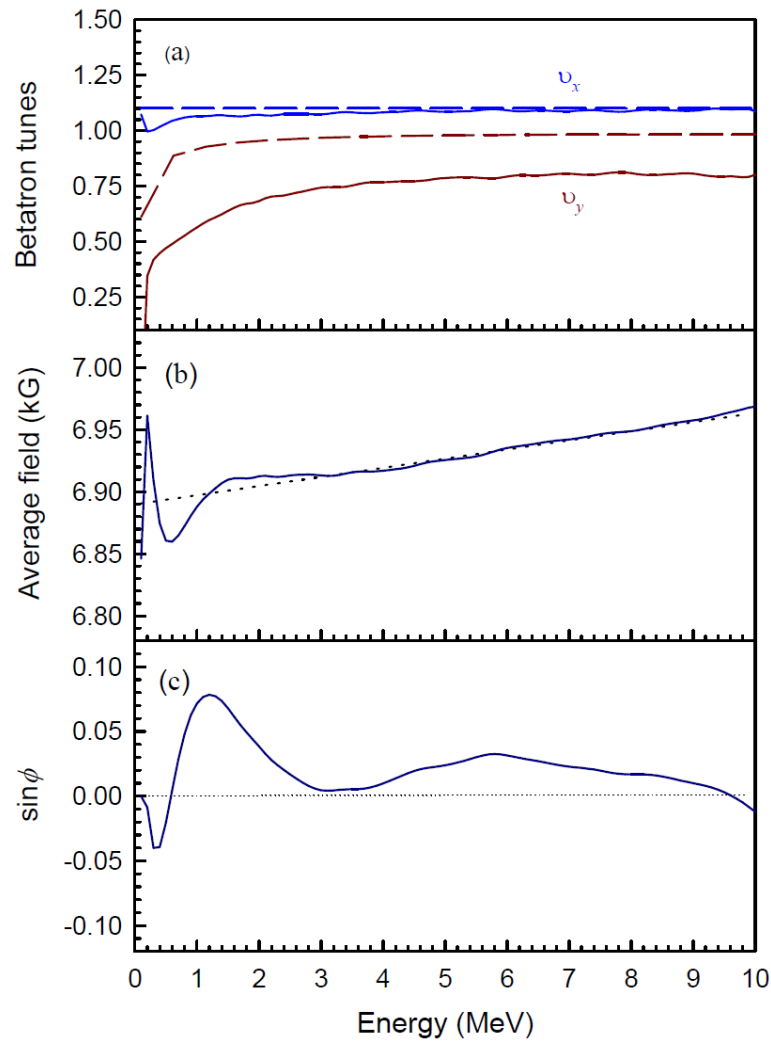


Fig. 3.4. Equilibrium orbit properties of the optimized magnet. (a) Radial and axial betatron tunes as a function of energy. Dotted curves represent the analytical values. (b) The optimized average magnetic field and required isochronous magnetic field (dotted) as a function of energy. (c) The phase slip $\sin\phi$ as a function of energy for initial phase $\phi_i = 2^0$, harmonic number $h = 4$ and peak energy gain per turn 500 keV.

Table 3.2

Parameters of the 10 MeV cyclotron

Parameters	Values
Injection energy	100 keV/80 keV
Final energy	10 MeV
Injection radius	6.6 cm
Extraction radius	65 cm
Hill / Valley field	1.5 T/0.15 T
Pole gap; Hill/ Valley	5 cm/50 cm
Sector width	16-34 deg.
Pole radius	72 cm
Ampere turn	315×200
Iron weight	25 ton

One of the most difficult problem to solve was the shaping of the magnetic field in the central region. The estimated height of the spiral inflector is comparatively large, around 10 cm (80 keV injection energy), and therefore, a careful optimization of the central plug was needed. We have optimized the height and position of the plug, hill extension in the central region to get the average field close to the isochronous magnetic field.

3.2. Design of the spiral inflector

The design of a spiral inflector assuming a constant magnetic field has been described by many authors [52-56]. This simplification is almost always satisfied when the injection energy of the beam is low (~10-20 keV) and the dimension of the inflector is comparatively small (height ~ 2-4 cm). Due to low average magnetic field and large difference between hill and valley fields, the computed magnetic field in the central region

near the axis of our 10 MeV cyclotron is slightly lower than the resonance field. Near the central region it also varies with height as well as with radius. The variation of the magnetic field with distance z from the median plane along the cyclotron axis is shown in [Fig. 3.5](#). Due to these large variations the design of the spiral inflector and central region geometry are more complicated and challenging. Here we briefly outline the formulations used by us to design the spiral inflector [\[12\]](#).

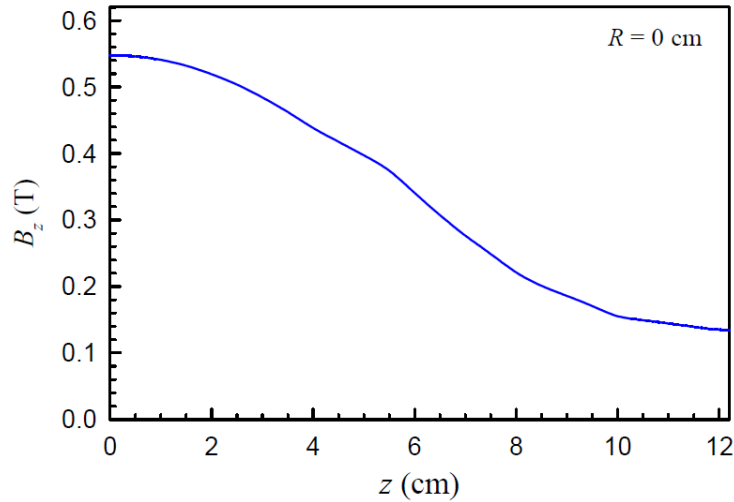


Fig. 3.5. Variation of the magnetic field with distance z from the median plane along the cyclotron axis. Data is obtained from 3D code.

3.2.1. Coordinate system

In a spiral inflector two coordinate systems are generally used [\[57\]](#). We have used the right handed Cartesian coordinate system x , y and z with its origin lies on the cyclotron axis in the median plane. The three unit vectors \hat{x} , \hat{y} and \hat{z} point along the x , y and z axes respectively. The z axis is vertically opposite to the direction of the incoming ion and major component of the magnetic field (B_z) is opposite to the z direction and x and y axes are in the median plane. The electric field at the entrance of the inflector is along the x direction. The second coordinate system is the optical coordinate system u, h and v with basis vectors \hat{u} , \hat{h} and \hat{v} which moves in space along with the central ion trajectory.

Here u, h and v denote the coordinates of a paraxial ray. Vector \vec{v} is along the direction of the velocity of the beam, vector \vec{h} is always parallel to the median plane (x - y plane) and vector $\vec{u} = \vec{h} \times \vec{v}$. It is parallel to the median plane at the entrance of the inflector, changes its direction as the beam advances and becomes perpendicular to the median plane at the exit of the inflector. A schematic diagram of both coordinate systems is shown in Fig. 3.6.

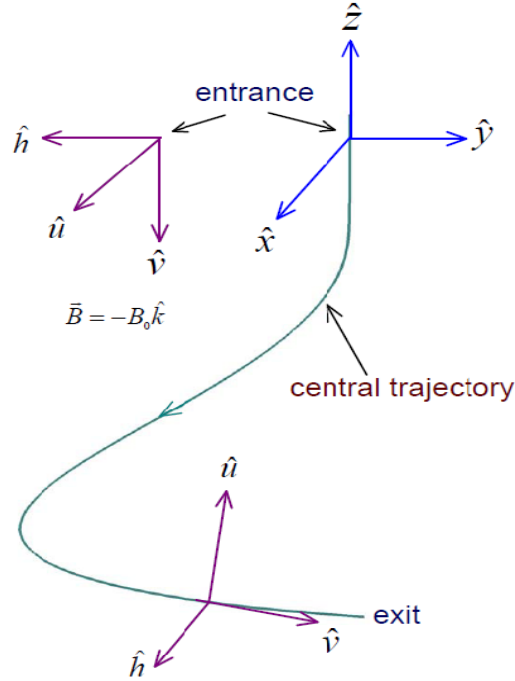


Fig. 3.6. A schematic of fixed right handed cartesian (x, y, z) and optical (u, h, v) coordinate system. The electric field is along the x direction at the entrance of the inflector and the magnetic field is uniform and opposite to the z direction.

If $v_0 = \sqrt{\dot{x}^2 + \dot{y}^2 + \dot{z}^2}$ is the velocity of an ion on the central trajectory, where \dot{x} , \dot{y} and \dot{z} are the velocity components of the central ion along x , y and z respectively, then the unit vectors \hat{u} , \hat{h} and \hat{v} can be expressed in terms of \hat{x} , \hat{y} and \hat{z} as

$$\hat{u} = -\frac{\dot{x}\dot{z}}{v_0\sqrt{v_0^2 - \dot{z}^2}}\hat{x} - \frac{\dot{y}\dot{z}}{v_0\sqrt{v_0^2 - \dot{y}^2}}\hat{y} + \frac{\sqrt{v_0^2 - \dot{z}^2}}{v_0}\hat{z} \quad (3.11)$$

$$\hat{h} = \frac{\dot{y}\hat{x} - \dot{x}\hat{y}}{\sqrt{v_0^2 - \dot{z}^2}} \quad (3.12)$$

$$\hat{v} = \frac{\dot{x}\hat{x} + \dot{y}\hat{y} + \dot{z}\hat{z}}{v_0} \quad (3.13)$$

where dot denotes the differentiation with respect to time t .

3.2.2. Central ion trajectory

The components of Lorentz force equation in the combined electric and magnetic fields can be written as:

$$x'' = \frac{q}{mv_0^2} E_x + \frac{q}{mv_0} (z'B_y - y'B_z) \quad (3.14)$$

$$y'' = \frac{q}{mv_0^2} E_y + \frac{q}{mv_0} (x'B_z - z'B_x) \quad (3.15)$$

$$z'' = \frac{q}{mv_0^2} E_z + \frac{q}{mv_0} (y'B_x - x'B_y) \quad (3.16)$$

where q , m and v_0 are the charge, mass and velocity of the ion respectively. Here the electric and magnetic fields both are functions of coordinates x , y and z and prime denotes the differentiation with respect to path length $s = v_0 t$. In order to find the analytical electric field inside the spiral inflector we have made the following assumptions:

- a) The u component of the electric field, E_u is constant (E_0) at all points along the central trajectories.
- b) The v component of the electric field E_v is zero.

Using these assumptions, the electric field in a tilted spiral inflector can be written as

$$\vec{E} = E_u \hat{u} + E_h \hat{h} = |\vec{E}| \cos(\theta) \hat{u} + |\vec{E}| \sin(\theta) \hat{h} \quad (3.17)$$

where $|\vec{E}|$ is the electric field strength seen by the central ion trajectory and θ is the local tilt angle. **Figure 3.7** shows the u - h cross-sectional view. Since the electrodes surface of

the spiral inflector are slanted by an angle θ , we introduce a rotated optical coordinate system defined by rotating the vectors \hat{u} and \hat{h} about the vector \hat{v} by an angle θ . Thus

$$\hat{u}_r = \cos\theta \cdot \hat{u} + \sin\theta \cdot \hat{h} \quad (3.18)$$

$$\hat{h}_r = -\sin\theta \cdot \hat{u} + \cos\theta \cdot \hat{h} \quad (3.19)$$

and they form the right handed coordinate system $(\hat{u}_r, \hat{h}_r, \hat{v})$ as shown in Fig. 3.7.

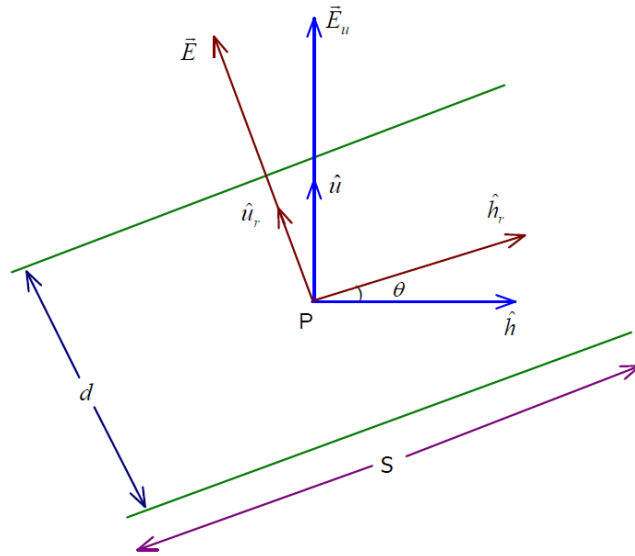


Fig. 3.7. Spiral inflector geometry as viewed from a plane perpendicular to the central trajectory. Here d is the electrode spacing and S is the width of the electrodes.

From Fig. 3.7 and using the condition (a) we can write,

$$|\vec{E}| = \frac{E_u}{\cos\theta} = \frac{E_0}{\cos\theta} \quad (3.20)$$

Here E_0 is the magnitude of the electric field which is always constant and perpendicular to the direction of motion of the ion. For a given kinetic energy T of the beam, it decides the height parameter A of the spiral inflector, defined as

$$A = 2T/qE_0 \quad (3.21)$$

In fact, A is the electric radius of the ion in the absence of the magnetic field. For an inflector without tilt the spacing between electrodes is held constant to keep the magnitude

of the electric field E_0 a constant and so the electrical radius A . In the case of a tilted inflector a component of the electric field is used to generate a force in the plane of the magnetic force to modify the beam centering. Here the spacing between electrodes is narrowed gradually so that the electric radius A remains constant. The local tilt angle θ as used earlier is defined by

$$\tan \theta = k' \frac{A - z(s)}{A} \quad (3.22)$$

where k' is a free parameter and it decides the maximum tilt angle $\theta_m = \tan^{-1} k'$ at the exit of the inflector. Using equations (3.11), (3.12) and (3.20) in equation (3.17) we can write the components of the electric field in the spiral inflector as,

$$E_x = E_0 \left(-\frac{x'z'}{\sqrt{x'^2 + y'^2}} - \frac{y'}{\sqrt{x'^2 + y'^2}} \tan \theta \right) \quad (3.23)$$

$$E_y = E_0 \left(-\frac{y'z'}{\sqrt{x'^2 + y'^2}} + \frac{x'}{\sqrt{x'^2 + y'^2}} \tan \theta \right) \quad (3.24)$$

$$E_z = E_0 \sqrt{x'^2 + y'^2} \quad (3.25)$$

Choosing a suitable value of A and k' one can easily solve Eqs. (3.15)-(3.16) to get the coordinates of the central ion trajectory in a given magnetic field.

One of the important parameter required to be optimized in the design of the spiral inflector is the “off- centre” i.e. the displacement of the centre of the trajectory from the vertical axis at the exit of the inflector. It is given by

$$\rho_c = \sqrt{x_c^2 + y_c^2} \quad (3.26)$$

$$x_c = x + \frac{x''(x'^2 + y'^2)}{(x'y'' - y'x'')^2}, \quad y_c = y + \frac{y''(x'^2 + y'^2)}{(x'y'' - y'x'')^2} \quad (3.27)$$

Here all the values of x, x', x'' and y, y', y'' are evaluated at the exit of the inflector. While designing an inflector one needs to optimize the off-center parameter at the exit of the inflector to meet the requirement of the orbit centering of the beam in the central region for further acceleration. If the central magnetic field is not enough to make the beam well centered, the height A and tilt k' are required to be adjusted properly. The height A of the inflector is limited by the space available in the central region. More tilt affects the beam emittance adversely, reduces the gap between electrodes in the exit region and makes the fabrication of the inflector difficult. Therefore, a proper choice of parameters A and k' plays an important role in the design of the spiral inflector.

3.2.3. Central ion trajectory in a constant magnetic field

It is easy and straight forward to show that the general equations for the spiral inflector developed so far can be reduced to the well-known equations presented in the literature for the case of a constant magnetic field i.e. $B_x = B_y = 0$ and $B_z = B_0$. Equations (3.14)-(3.16) and (3.23)-(3.25) with some algebraic manipulations take the following form:

$$x''(b) = A[\cos(2Kb)\cos b - k'\sin(2Kb)\sin b] - \frac{qA}{mv_0} y'(b)B_0 \quad (3.28)$$

$$y''(b) = A[\sin(2Kb)\cos b + k'\cos(2Kb)\sin b] + \frac{qA}{mv_0} x'(b)B_0 \quad (3.29)$$

$$z''(b) = A \sin b \quad (3.30)$$

where $b = (v_0 t / A) = (s / A)$ is the instantaneous angle of the velocity vector with the vertical. The shape parameter K is defined by

$$K = \frac{A}{2R_m} + \frac{k'}{2} \quad (3.31)$$

Here $R_m = p/qB_0$ is the magnetic radius of the ion with momentum p . Equations (3.28)-(3.30) can be solved analytically to yield the following parametric equations;

$$x(b) = \frac{A}{2} \left[\frac{2}{1-4K^2} + \frac{\cos[(2K-1)b]}{2K-1} - \frac{\cos[(2K+1)b]}{2K+1} \right] \quad (3.32)$$

$$y(b) = -\frac{A}{2} \left[\frac{\sin[(2K+1)b]}{2K+1} - \frac{\sin[(2K-1)b]}{2K-1} \right] \quad (3.33)$$

$$z(b) = A(1 - \sin b), \quad 0 \leq b \leq \pi/2 \quad (3.34)$$

These equations agree with the equations presented in many references mentioned earlier.

3.2.4. Orbit calculations and design parameters

In this subsection we present the design results of the spiral inflector. As mentioned earlier, the ion source is more stable and reliable against sparks and electric discharges in the extraction region when operated with extraction voltage near 80-85 kV. So we have worked out the design of the spiral inflector for 80 keV injection energy. The option of using 100 keV injection energy is still open. We have performed all the calculations at 100 keV also, however, in this thesis we present the results for 80 keV only.

The design of an inflector is an iterative process. For a given injection energy a suitable value of parameter A is chosen considering a reasonable value of the electric field between the electrodes (< 20 kV/cm) to avoid any sparking. The tilt parameter k' is then varied to produce the desired orbit centre at the inflector exit. We have written a computer code to solve Eqs. (3.14) to (3.16) for the central trajectory in the inflector using magnetic field data obtained from 3D code and electric field from Eqs. (3.23) to (3.25). The gap between electrodes is chosen ~ 14 mm to ensure the loss free bending of the beam with maximum diameter of 10 mm. The aspect ratio ξ , defined as the width of the electrode divided by gap between the electrodes is taken equal to 2, first to avoid the effect of the fringe field and second to tolerate the shift in the beam trajectory inside the inflector. The grounded plates parallel to the inflector entrance and exit are placed 7 mm away from the

inflector such that opening of these plates coincide with the opening of the inflector at the entrance and exit. Important parameters of the inflector are listed in Table 3.3.

Table 3.3

Optimized parameters of the inflector

Parameters	Values
Height (A)	8.65 cm
Tilt (k)	0.65
Electric field (E_0)	18.5 kV/cm
Aspect ratio (ξ)	2
Off centering (ρ_c)	4.1 cm
Gap (d_0) entrance/exit	14 mm/12 mm
Position at exit (r, θ)	7.05 cm, 99.11°
Exit data (x_e, y_e)	(-1.24, 6.84) cm

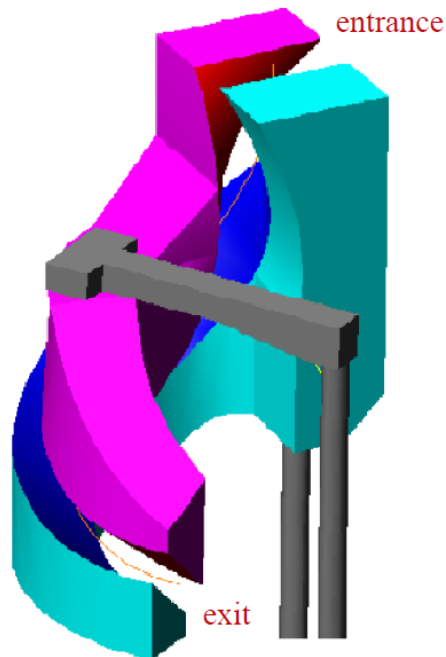


Fig. 3.8. Electrode geometry of the spiral inflector. Ground electrodes at the entrance and exit are not shown in the figure.

The data of the central ion trajectory in the inflector obtained from the code has been used in program INFLECTOR [58] to generate the shape of electrodes and mesh points for RELAX3D [59] to compute the electric field distributions in the inflector. Figure 3.8 shows the geometry of the spiral inflector without ground plates. Figure 3.9 shows the computed electric field strength on the central ion trajectory (u plane) and compares it with the analytical electric field (hard edge approximation) used for the initial design.

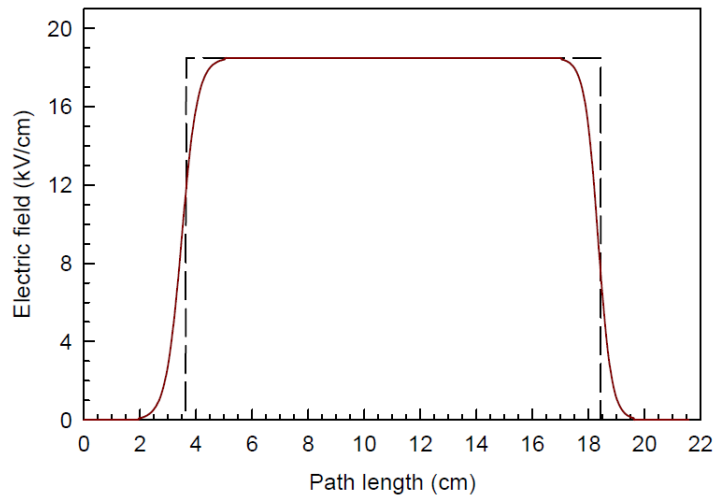


Fig. 3.9. Comparison of the analytic (dotted) and computed (solid) electric fields along the central ion trajectory in the spiral inflector.

It can be readily seen from Fig. 3.9 that the extension of fringe field is very small compared to that of short inflectors where entrance and exit fringe fields contribute significantly. This may be due to the choice of a comparatively large aspect ratio ξ and height A of the inflector in the present design. We found very small difference in the coordinates of the central ion trajectory calculated using analytic and computed electric fields. The computed electric field and magnetic field data are then used to optimize the geometry to get the desired orbit center at the exit of the inflector.

3.2.5. Orbit centering

The orbit centering of the inflected beam has been checked by using the central region code which solves the equations of motion in a combined electric and magnetic fields. The

coordinates and direction of the velocity of the particle following the central trajectory are obtained at the inflector exit and entered as an input to the central region code. All calculations of beam centering have been performed with the parameters listed in Table 3.4. The orbit tracing has been done using the computed magnetic field (3D) data. The electric field distribution in the median plane at four accelerating gaps is approximated by a Gaussian function given by the following expression, $E_g = (V_g / \sigma \sqrt{2\pi}) \exp(-x^2 / 2\sigma^2)$, $\sigma = 2(0.4W + 0.2H)$ where $2W$ is the gap between the dee and dummy dee (ground electrode), $2H$ is the height of the dee and $x = 0$ is the gap centre. This formula for the horizontal component of electric field E_g within the accelerating gap in the median plane generates electric field which is very close to the numerically computed electric field [60].

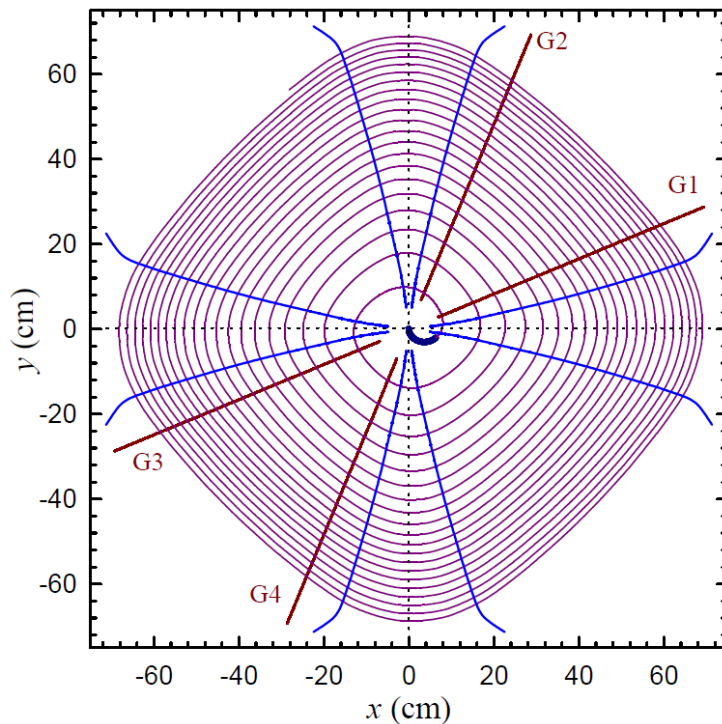


Fig. 3.10. Position of the inflector, location of the accelerating gaps G-1 to G-4 in the median plane (x - y plane) and accelerated orbits of proton from 80 keV to 10 MeV.

Figure 3.10 shows the horizontal cross section in the central region, position of the inflector, location of the accelerating gaps G-1 to G-4 in the x - y plane (median plane) and accelerated orbits of protons from 80 keV to 10 MeV. It is easy to see from Fig. 3.10 that

the beam is well centered with the input condition provided by the spiral inflector. The position of the orbit center has also been found to converge satisfactorily after few turns.

Table 3.4

Parameters used for orbit tracing

Parameters	Values
Dee voltage (V_g)	125 kV
r.f. frequency (f_{rf})	42 MHz
Harmonic No. (h)	4
Dee gap (W)	2 cm
Dee height (H)	3 cm
Phase width ($\Delta\phi$)	$\pm 15^\circ$

3.3. Summary

In this Chapter, we have described random search techniques for obtaining the isochronous magnetic field for a compact cyclotron by optimization of pole profile of the hill. The advantage of this method is that one can optimise the sector geometry using only few parameters (5-8) of the polynomial. This reduces the initial computational effort required to generate the correlation matrix by running the 3D code. This method is fast and converges in five to six iterations and it allows one to include constraints during optimization. The acceptable range of the various parameters, such as the coil current (i.e., the central magnetic field), minimum and maximum hill angles, etc., can be easily incorporated. We have also described a design procedure of the spiral inflector in the inhomogeneous magnetic field. Axially available space in the central region for the inflector and the beam centering requirement forced us to choose the tilt parameter $k' = 0.65$, making the fabrication a challenging job.

Chapter 4

Space charge effect in the spiral inflector

4.1. Introduction

In this Chapter we present a numerical method to study the space charge dominated beam dynamics in the spiral inflector. Numerous studies related to the inflector beam optics have been reported by several researchers in the literature [52-56, 61-65]. The recent requirement of high current beam injection in a cyclotron [66-69] demands for more detailed analysis of beam transport through this including the effect of space charge.

Many authors [70-72] have discussed about the beam transport through a spiral inflector including the effect of space charge by assuming a simple model of a continuous cylindrical beam with uniform distribution. However, in the real situation, as the injected dc beam from the ion source approaches the inflector, it takes the form of a bunch due to bunching action. The beam current in the bunch increases gradually as it traverses inside the spiral inflector. This effect modifies the space charge force on the particles in the beam and needs to be taken into account for more accurate analysis of the beam dynamics through the spiral inflector.

In the following section, first we derive the equations of paraxial ion trajectories assuming the beam as a well defined ellipsoidal bunch. This assumption is more realistic compared to the uniform cylindrical beam. The increase of current in the bunch due to bunching action is included in the calculation as the beam traverses inside the inflector. The increase in the transverse space charge force is taken proportional to the increase of beam current in the bunch. We have also calculated the beam envelopes inside the inflector and projected emittances at the exit of the inflector using the sigma matrix

method. The initial starting conditions of the beam have been optimized to obtain desired phase ellipses with minimum emittance growth in the two transverse phase planes at the exit of the inflector. Furthermore, the four dimensional transverse acceptance of the spiral inflector has been estimated as a function of beam current.

4.2. Transverse beam dynamics

In the derivation of paraxial ion trajectory equations we have assumed the beam bunch as a well defined ellipsoid with radial semi axis r_m and longitudinal semi axis v_m in the bunch frame. As mentioned earlier the velocity modulation imparted to the beam at the buncher gap leads to the density modulation as the beam advances and thus at each step, the charge density $\rho_0(b)$ in the bunch will take a new value. We have assumed that, though the local charge density $\rho_0(b)$ will vary with path length, it will remain uniform in the bunch. The uniformity of local charge density in the bunch is a simplified approximation; however, it is very near to the real situation. It has some advantage in terms of studying the beam dynamics because in this case the space charge forces are linear. In the following derivations we have also assumed that the bunch shape remains ellipsoidal within the inflector, the effect of image charge due to the conducting boundary is negligible and the beam radius r_m remains constant inside the spiral inflector.

4.2.1. Space charge field

The space charge potential at any point inside the ellipsoidal bunch is given by the following expression [73, 74],

$$\phi_s(r, v, b) = -\frac{\rho_0(b)}{4\epsilon_0} [(1-M)r^2 + 2M \cdot v^2] \quad (4.1)$$

where r is the radial distance from the bunch axis and v is the distance along longitudinal direction from the bunch centre.

The parameter M for $\alpha > 1$, where $\alpha = (v_m / r_m)$, is given by the following expression:

$$M = -\frac{1}{\alpha^2 - 1} + \frac{\alpha}{2(\alpha^2 - 1)^{3/2}} \ln \left| \frac{\alpha + (\alpha^2 - 1)^{1/2}}{\alpha - (\alpha^2 - 1)^{1/2}} \right| \quad (4.2)$$

and for $\alpha < 1$

$$M = \frac{1}{1 - \alpha^2} - \frac{\alpha}{(1 - \alpha^2)^{3/2}} \tan^{-1} \left(\frac{1}{\alpha^2} - 1 \right)^{1/2} \quad (4.3)$$

In the moving frame of the bunch the space charge force is purely electrostatic. The longitudinal and radial space charge electric fields can be easily obtained by differentiating Eq. (4.1) with respect to v and r respectively. In dealing with the spiral inflector it is common practice to use the so called optical coordinate systems (u, h, v) and (u_r, h_r, v) as defined earlier. The origin of this system is at the bunch center and travels along the central trajectory. Calculations become easy after expressing the electric field components in the optical coordinate systems. Using the relations between the two optical coordinate systems described in detail in [57], it is straight forward to get the following expressions for the space charge electric fields from Eq. (4.1) as

$$\vec{E}_v^{SC} = \frac{\rho_0(b)Mv}{\epsilon_0} \hat{v} = \frac{3I_p(b)Mv}{4\pi\epsilon_0 r_m^2 v_m f} \frac{\Delta\phi}{2\pi} \hat{v} \quad (4.4)$$

$$\vec{E}_r^{SC} = \frac{\rho_0(b)(1-M)r}{2\epsilon_0} \hat{r} = \frac{3I_p(b)(1-M)}{8\pi\epsilon_0 r_m^2 v_m f} \frac{\Delta\phi}{2\pi} (u\hat{u} + h\hat{h}) \quad (4.5)$$

where I_p , is the peak beam current, given by

$$I_p(b) = I \cdot \frac{2\pi}{\Delta\phi} = Q(b)f \frac{2\pi}{\Delta\phi} = \frac{4}{3} \pi r_m^2 v_m \rho_0(b)f \frac{2\pi}{\Delta\phi} \quad (4.6)$$

in which I is the average beam current, f is the frequency of the voltage applied on the buncher, $Q(b)$ is the total charge in the bunch and $\Delta\phi$ is the beam phase width.

4.2.2. Paraxial ray equations

In the derivation of paraxial ray equations in the presence of space charge we have used the analytic electric field and a constant magnetic field. Let $\vec{r}_p(t)$ and $\vec{r}_c(t)$ be the position vectors of the paraxial and central trajectory particles of charge q and mass m at time t respectively. Then both position vectors must follow the Lorentz equation of motion:

$$m\ddot{\vec{r}}_p = q[\vec{E}(\vec{r}_p) + \vec{E}^{SC} + \dot{\vec{r}}_p \times \vec{B}(\vec{r}_p)] \quad (4.7)$$

$$m\ddot{\vec{r}}_c = q[\vec{E}(\vec{r}_c) + \dot{\vec{r}}_c \times \vec{B}(\vec{r}_c)] \quad (4.8)$$

If the magnetic field \vec{B} is constant throughout the volume of the spiral inflector then the equation of motion of the paraxial ion with respect to the central trajectory at time t can be written as

$$m\ddot{\vec{r}}_1 = q[\Delta\vec{E} + \vec{E}^{SC} + \dot{\vec{r}}_1 \times \vec{B}] \quad (4.9)$$

where $\vec{r}_1 = \vec{r}_p - \vec{r}_c = u\hat{u} + h\hat{h} + v\hat{v} = r\hat{r} + v\hat{v}$ is the displacement vector of the paraxial ray from the bunch centre and $\Delta\vec{E}$ is the first order change in the electric field with respect to the central ray. Here u, h and v denote the coordinates of the paraxial ray and dot indicates the differentiation with respect to time t .

The components of $\Delta\vec{E}$ in the optical coordinate system can be obtained by taking the first order change in the electric field with respect to the central ray [57]

$$\Delta\vec{E}(v, h_r, u_r) = \vec{E}(b, h_r, u_r) - \vec{E}(b, 0, 0) + \frac{v}{A} \frac{\partial \vec{E}}{\partial b} \Big|_{h_r, u_r=0} \quad (4.10)$$

where u_r, h_r and v are the projections of the displacement from the central ion trajectory (\vec{r}_1) on the rotated coordinate system. The expression of $\Delta\vec{E}$ in the (u, h, v) coordinate system can be written as [57]

$$\Delta E_u = \frac{E_0}{A} \left\{ (u - hk' \sin b) \frac{1 + 2Kk' \sin^2 b}{1 + k'^2 \sin^2 b} - 2vKk' \sin b \cos b \right\} \quad (4.11a)$$

$$\Delta E_h = \frac{E_0}{A} \left\{ -v(2K + k') \cos b + (u - hk' \sin b) \frac{k' \sin b (1 + 2Kk' \sin^2 b)}{1 + k'^2 \sin^2 b} \right\} \quad (4.11b)$$

$$\Delta E_v = \frac{E_0}{A} \left\{ -2uKk' \sin b \cos b - v(1 + 2Kk' \sin^2 b) - h(2K + k') \cos b \right\} \quad (4.11c)$$

Using the relation $\frac{d}{dt} = \frac{v_0}{A} \frac{d}{db}$ and the first and second derivatives of \hat{u} , \hat{h} and \hat{v} with respect to the angle b and keeping only first order terms, we can easily obtain the expressions of $\dot{\vec{r}}_1$ and $\ddot{\vec{r}}_1$ as,

$$\dot{\vec{r}}_1 = \frac{v_0}{A} [(u' + 2Kh \cos b + v) \cdot \hat{u} - (2Ku \cos b - h' + 2Kv \sin b) \cdot \hat{h} + (v' - u + 2Kh \sin b) \cdot \hat{v}] \quad (4.12)$$

$$\begin{aligned} \ddot{\vec{r}}_1 = \frac{v_0^2}{A^2} \{ & [u'' - u(1 + 4K^2 \cos^2 b) + 4Kh' \cos b + 2v' - 4vK^2 \sin b \cos b] \cdot \hat{u} \\ & + [4Ku \sin b - 4Ku' \cos b + h'' - 4K^2 h - 4Kv' \sin b - 4Kv \cos b] \cdot \hat{h} \\ & + [v'' - 2u' - 4K^2 u \sin b \cos b + 4Kh' \sin b - v(1 + 4K^2 \sin^2 b)] \cdot \hat{v} \} \end{aligned} \quad (4.13)$$

Using the relation for the constant magnetic field through the spiral inflector

$$\vec{B} = -B_0 \hat{k} = -B_0 (\sin b \cdot \hat{u} - \cos b \cdot \hat{v}) \quad (4.14)$$

and using Eqs. (4.4), (4.5) and (4.9-4.14) we can obtain the coupled differential equations for the paraxial ion trajectory through the spiral inflector as

$$u'' = -2v' - (2K + k')h' \cos b + u + 2uKk' \cos^2 b + (u - hk' \sin b) \times \frac{1 + 2Kk' \sin^2 b}{1 + k'^2 \sin^2 b} + \frac{3I_p(b)(1-M)}{8\pi\epsilon_0 r_m^2 v_m f} \frac{\Delta\phi}{2\pi} \frac{uA}{E_0} \quad (4.15a)$$

$$h'' = -(2K + k')(u \sin b - u' \cos b - v' \sin b) - (u - hk' \sin b) \times \frac{k' \sin b (1 + 2Kk' \sin^2 b)}{1 + k'^2 \sin^2 b} + 2hKk' + \frac{3I_p(b)(1-M)}{8\pi\epsilon_0 r_m^2 v_m f} \frac{\Delta\phi}{2\pi} \frac{hA}{E_0} \quad (4.15b)$$

$$v'' = -(2K + k')(h' \sin b + h \cos b) + 2u' + \frac{3I_p(b)M}{4\pi\epsilon_0 r_m^2 v_m f} \frac{\Delta\phi}{2\pi} \frac{vA}{E_0} \quad (4.15c)$$

The last term on the right hand side of each of the paraxial ion equations (4.15) is due to the space charge effects. In the case of a uniform cylindrical beam these terms in u , h and v directions take the form $\frac{I_p A u}{2\pi\epsilon_0 r_m^2 v_0 E_0}$, $\frac{I_p A h}{2\pi\epsilon_0 r_m^2 v_0 E_0}$ and 0 respectively, where v_0 is the velocity of the beam. The relation between beam divergence p_u , p_h and p_v in the coordinate system perpendicular to the central trajectory velocity vector and u' , h' and v' can be given by [52],

$$u' = A p_u - 2hK \cos b \quad (4.16a)$$

$$h' = A p_h + 2uK \cos b \quad (4.16b)$$

$$v' = A p_v + u - 2hK \sin b \quad (4.16c)$$

Equations (4.15) cannot be solved analytically and hence a numerical integration method is needed to get the coordinates of the paraxial ion trajectory. One can easily estimate approximate beam envelope through the spiral inflector by solving the paraxial trajectories for several representative particles that belong to the boundary of the contours in $(u - p_u)$ and $(h - p_h)$ planes as well as in the interior of the phase ellipse at the entrance. However an easy way to obtain the envelope is to use the infinitesimal transfer matrix as discussed in the following sub-section.

4.2.3. Beam envelopes

Since paraxial ray equations presented in the previous subsection are linear, therefore any solution of these equations can be represented by the linear combinations of six linearly independent solutions. Let $\mathbf{x}(s_0) = (u, p_u, h, p_h, v, p_v)^T$ represents the coordinates of a paraxial ray at a location s_0 . At some other location s , the coordinates will be

transformed according to the matrix equation, $\mathbf{x}(s) = \mathbf{M}(s, s_0) \mathbf{x}(s_0)$ where $\mathbf{M}(s, s_0)$ is a 6×6 transfer matrix whose elements are functions of s and s_0 . In order to generate matrix $\mathbf{M}(s, s_0)$, we need to solve Eqs. (4.15) for six different initial conditions. A simple way is to choose initial condition in which one coordinate say u is equal to 1 and all other coordinates are equal to 0. The solution of differential equations will yield the first column of transfer matrix \mathbf{M} . By repeating the same procedure with other coordinates one can easily get all other columns of matrix \mathbf{M} . It is to be noted here that the initial conditions for forming the matrix elements should be canonical so that matrix \mathbf{M} should be a symplectic one. As the inflector is put in the axial magnetic field B_0 of the cyclotron, the variable $\mathbf{x}(s_0)$ are no longer canonical at the inflector entrance. To make the variables canonical we need to modify them by multiplying with the matrix [75] :

$$\begin{pmatrix} 1 & 0 & 0 & 0 & 0 & 0 \\ 0 & 1 & 1/2R_m & 0 & 0 & 0 \\ 0 & 0 & 1 & 0 & 0 & 0 \\ -1/2R_m & 0 & 0 & 1 & 0 & 0 \\ 0 & 0 & 0 & 0 & 1 & 0 \\ 0 & 0 & 0 & 0 & 0 & 1 \end{pmatrix} \quad (4.17)$$

The transfer matrix so developed can be used to study the beam properties through the spiral inflector. In order to study the effect of space charge on the inter plane coupling when the beam passes through the inflector, we need to calculate the six dimensional beam matrix σ as a function of the path length s . The beam matrix σ can be defined as

$$\sigma = \langle \mathbf{x} \mathbf{x}^T \rangle \quad (4.18)$$

where $\langle \rangle$ denotes the average over the beam distribution. The evolution of sigma matrix at position s can be obtained from

$$\sigma(s) = \mathbf{M}(s, s_0) \sigma(s_0) \mathbf{M}^T(s, s_0) \quad (4.19)$$

where $\sigma(s_0)$ is the beam matrix at location s_0 . The rms beam sizes and the rms emittances in the u and h planes at a point s can be obtained from the following relations

$$\begin{aligned}\tilde{U}(s) &= \sqrt{\sigma_{11}(s)}, \quad \tilde{H}(s) = \sqrt{\sigma_{33}(s)} \\ \tilde{\varepsilon}_u(s) &= \sqrt{(\sigma_{11}\sigma_{22} - \sigma_{12}\sigma_{21})}, \quad \tilde{\varepsilon}_h(s) = \sqrt{(\sigma_{33}\sigma_{44} - \sigma_{34}\sigma_{43})}\end{aligned}\quad (4.20)$$

Since we have considered the beam as a uniform ellipsoidal distribution, the actual beam sizes and emittances are related with the corresponding rms quantities as,

$$U(s) = \sqrt{5} \cdot \tilde{U}(s), \quad H(s) = \sqrt{5} \cdot \tilde{H}(s) \quad \text{and} \quad \varepsilon_u(s) = 5 \cdot \tilde{\varepsilon}_u(s), \quad \varepsilon_h(s) = 5 \cdot \tilde{\varepsilon}_h(s) \quad (4.21)$$

4.3. Numerical results and discussions

In this section we present the simulation results of space charge dominated beam behaviour through the spiral inflector with designed parameters $A = 8.65$ cm and $k' = 0.65$ of our 10 MeV cyclotron presented in Chapter 3 [12]. Since the paraxial trajectory equations through the inflector are valid only for a constant magnetic field, we have searched out an equivalent constant magnetic field B_0 ($= 5.15$ kG) to yield almost similar central ion trajectory what we obtained with the 3D magnetic field data. The energy conservation in the paraxial ray calculation was ensured by incorporating two discontinuous jumps $P_v = \pm(qV/d.T) \cdot u$ in the forward kinetic momentum at the entrance (+) and exit (-) of paraxial ion through the spiral inflector. Here V is the voltage on the inflector electrode and u is the paraxial ion displacement from the central ion [57].

As mentioned earlier, the bunch compression increases the peak current I_p in the bunch as it traverses through the spiral inflector and alters the space charge force. In order to include this effect in the beam dynamics, we have used the results of buncher simulation presented in detail in ref. [10]. The entrance of the inflector is located at a distance of 65 cm from the centre of the buncher gap. The variation of bunching factor

B_f , defined as the ratio of beam current in the specified bunch width at a given location s when the buncher is on to the beam current in the same bunch width when the buncher is off, is shown in Fig. 4.1 as a function of path length inside the spiral inflector from the entrance to exit. It can be readily seen that the beam current in the bunch is already increased by 4.8 times at the entrance of the inflector, increases gradually as the bunch traverses through the inflector and becomes almost 5.2 times at the exit of the inflector. This variation of beam current has been taken into account in the paraxial ion trajectory and envelope calculations. In the numerical calculations we have assumed $\Delta\phi = 30^\circ$ of rf. Since at injection energy of 80 keV and buncher frequency of 42 MHz, the bunch size corresponding to 30° of rf phase is equal to 7.8 mm, we have used the value of longitudinal semi axis of the ellipsoidal bunch equal to 3.9 mm. The value of radial semi axis is chosen 4.5 mm.

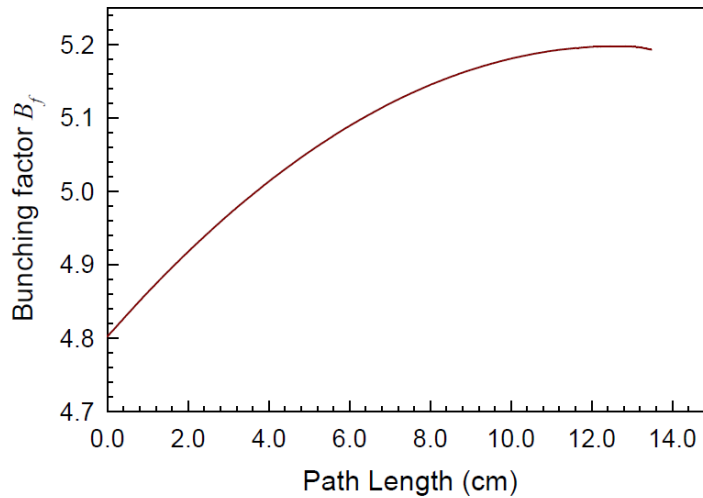


Fig. 4.1. The variation of bunching factor B_f with path length as the beam bunch moves inside the spiral inflector, showing the effect of bunching action of a sinusoidal buncher. The entrance of the inflector is located at 65 cm from the buncher gap.

4.3.1. Behaviour of beam envelopes

In order to determine the beam envelope quantities through the spiral inflector using the formulations developed in the previous sections we have written a computer code. It

first solves the paraxial trajectory given by Eqs. (4.15) for given initial beam conditions from point s_0 to $s = s_0 + ds$ in the spiral inflector, where ds is the small interval. In the calculations we have used the step size $ds = 0.5$ mm. Using the solution of paraxial ion trajectories for six different initial conditions, the infinitesimal transfer matrix $\mathbf{M}(s, s_0)$ is obtained for the small interval ds . This infinitesimal transfer matrix is then used to find out the beam matrix $\sigma(s)$ at point s from Eq. (4.19) utilizing the initial value of $\sigma(s_0)$. The beam envelope quantities are obtained from the elements of $\sigma(s)$ using Eqs. (4.20) and (4.21). The entire process is repeated until the exit of the spiral inflector is reached.

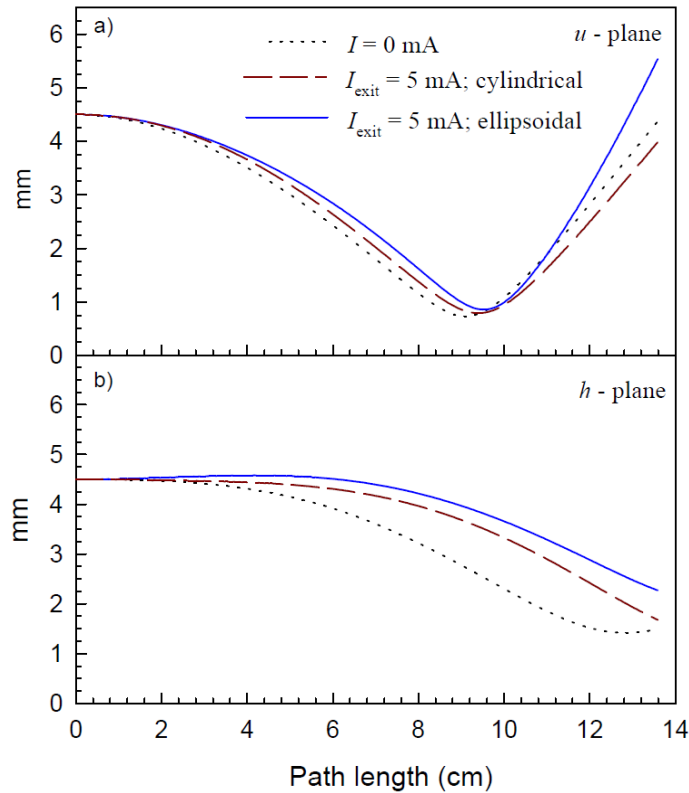


Fig. 4.2. The evolution of beam sizes through the spiral inflector in u and h planes for average beam current $I = 0$ mA (dotted curve) and $I = 5$ mA at the inflector exit. Dashed curves are for case of uniform cylindrical beam and solid lines belong to uniform ellipsoidal bunched beam.

Figure 4.2 compares the beam envelope through the spiral inflector in u and h planes for the case of ellipsoidal beam and cylindrical beam with same initial conditions and

same variation of beam current in the bunch inside the inflector (Fig. 4.1). We have considered the initial beam as an upright ellipse in both u and h planes with beam size $U = H = 4.5$ mm and emittance $\varepsilon_u = \varepsilon_h = 60 \pi$ mm mrad. It is evident from Fig. 4.2 that the space charge force contributes significantly at this current level and results of uniform cylindrical beam underestimates the space charge contributions in both the planes.

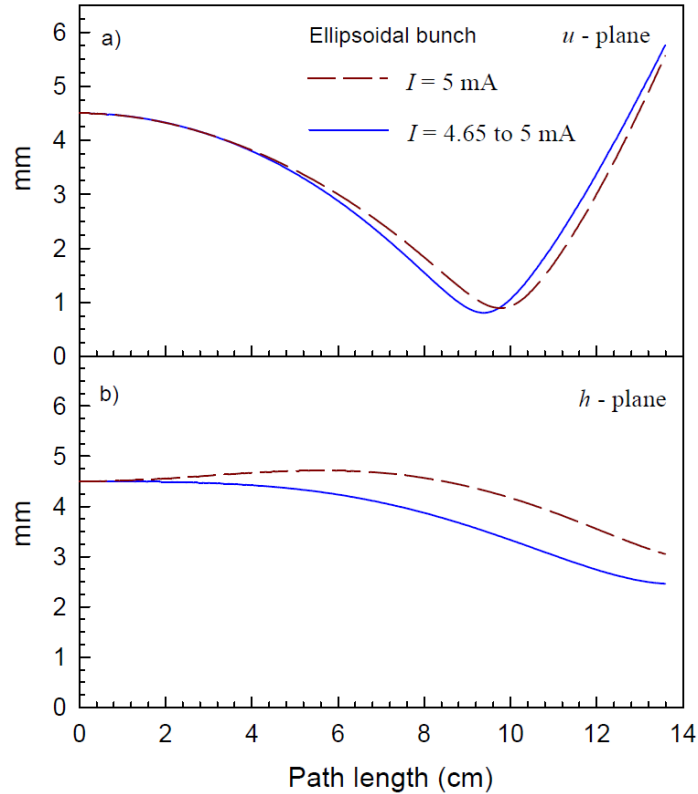


Fig. 4.3. Comparison of beam envelopes for ellipsoidal bunch with constant current (dashed curve) and gradually increasing current (solid curve) from entrance to exit.

As mentioned earlier, that when the beam enters the inflector it takes the form of a bunch and current in the bunch increases gradually as it traverses inside the inflector. In order to compare the effect of this variable beam current with the constant current in the bunch we have plotted the evolution of beam envelope through the spiral inflector in u and h planes in Fig. 4.3. Dashed curve represents the case when the average beam current in the bunch is constant and equal to 5 mA (peak current is 60 mA). Solid curve represents the case when the average current in the bunch is 4.65 mA (peak current is 55.8 mA) at the

entrance, increases gradually up to 5 mA (peak current is 60 mA) at the exit. It can be readily seen that there is a noticeable difference in the behaviour of envelopes in the h plane for the two cases.

4.3.2. Study of emittance growth

In a spiral inflector, there is a strong coupling between the two transverse directions which results in emittance growth at the exit. This emittance growth is very sensitive to the beam size and orientation of the phase ellipses of the beam at the entrance of the inflector. Initially the orientations of the entrance ellipses with zero beam current were adjusted to have minimum growth of emittances in both planes at the inflector exit. We then studied the behaviour of the emittance growth at the exit of the inflector by varying only beam current and keeping all other conditions unchanged. Results are illustrated in Fig. 4.4 by dotted curves. We then tried to optimize the initial conditions in u and h planes for each value of beam current to reduce the emittance growth in both the planes. Results are shown in Fig. 4.4 by solid curves. It can be readily seen from the Fig. 4.4 that emittance growth increases sharply in h plane when the beam current is high. During the optimization it is observed that the output condition in the u plane is very sensitive to the initial conditions. A slight variation in the input parameters to reduce the emittance causes rotation of the beam ellipse with increase in the beam size and beam divergence by large amount. During the optimization of emittance at the exit we have taken care that beam size and beam divergence remain within a reasonable limit in both the planes. The increase in emittances at zero beam current in both the planes is due to the inter plane coupling effects. The effect of space charge is rather weak below 3.0 mA in both the planes. We observed that the initial phase ellipses which correspond to the minimum emittance growth without space charge are not at all suitable when the space charge effect is included and hence the initial beam conditions need to be adjusted again to reduce the

emittance growth at the inflector exit. In other words, one needs different set of initial phase space ellipses to control the emittance growth if the beam current is changed.

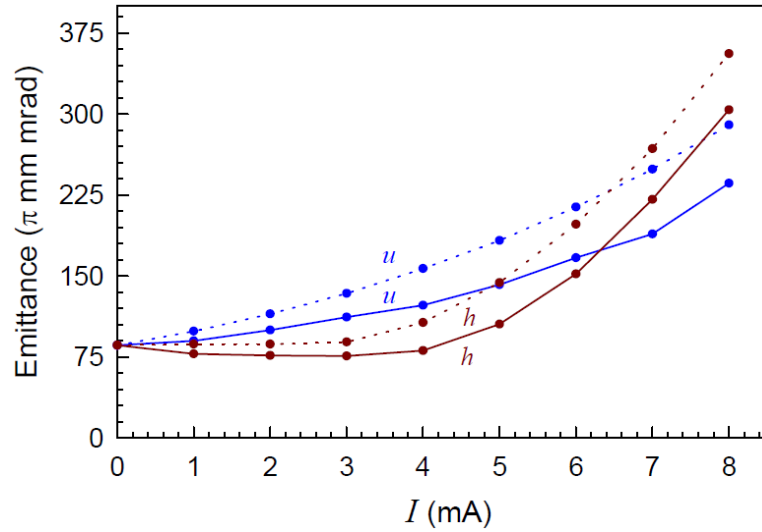


Fig. 4.4. Variation of un-optimized (dotted curve) and optimized (solid curve) beam emittances in u and h planes at the exit of the inflector as a function of the beam current. The initial beam emittance is 60π mm mrad in both phase planes.

Figure 4.5 shows the orientations of optimized phase ellipses, in h and u planes at the entrance and the resulting phase ellipses at the exit of the inflector for average beam current of 5 mA at the exit. While optimizing the orientation of the phase ellipses at the entrance of the inflector we have taken care that the emittance growth should be less in the vertical plane within the acceptable beam size, because focusing force in the central region is comparatively weak in this plane. An effort to reduce the emittance in u plane leads to an increase in the beam size and beam slope by a large amount. The large vertical defocusing (u -plane) at the inflector has also been observed in simulation by many authors [76-78]. This is a major concern and needs to be taken care during the optimization. Results show that comparatively large growth of emittance in both the planes is mainly due to the coupling effect. The estimated effective emittances at the exit in h and u planes are 106π mm mrad and 144π mm mrad for $I_{exit} = 5$ mA respectively. A comparison of emittances at the entrance and exit in h plane shows an increase by a

factor of 1.8 whereas in the u plane it is 2.4 times, which are within the acceptance of the central region. The acceptance of the central region at the inflector exit for 6 mm half aperture is 514π mm mrad in the horizontal plane and 200π mm mrad in the vertical plane. During the simulation we observed that the influence of coupling and space charge on emittance growth is comparatively large when one uses the upright input ellipses. To restrict the emittance growth within the acceptable value it is necessary to use tilted phase ellipses at the input of the spiral inflector.

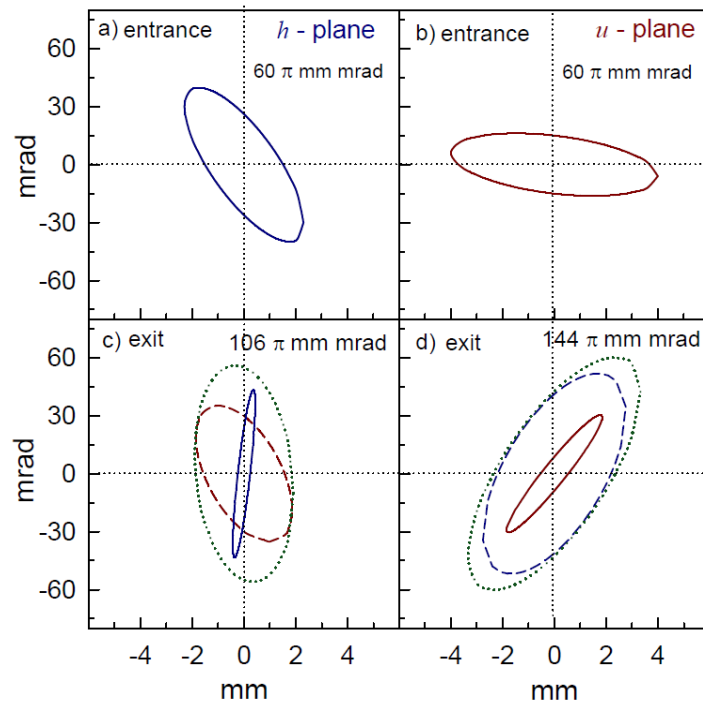


Fig. 4.5. Phase ellipses in h and u planes; (a) and (b) represent the optimized phase ellipses at the inflector entrance. (c) and (d) show the phase ellipses at the inflector exit for $I_{exit} = 5$ mA. Solid lines indicate the area pertaining to the particular phase plane and dashed lines the area arising from the coupling with other phase planes. The dotted curves in (c) and (d) represent the effective phase ellipses obtained using sigma matrix method.

4.3.3. Estimation of transverse acceptance

We have also calculated the four dimensional transverse acceptance of the spiral inflector i.e. the largest phase space volume that passes through the inflector. For this purpose we generated a uniform distribution of particles in four dimensional phase space

(u, p_u, h, p_h) and then tracked the paraxial ray of each of these particles through the inflector for a given value of the beam current. At each integration step we checked the location of particles and accepted only those which were within the 75% of the available aperture $u_{\max} = \pm d/2$ and $h_{\max} = \pm \xi d/2$ in the spiral inflector in both the planes. The rms quantities of all the accepted particles were analyzed to obtain the elements of the sigma matrix. The square root of the determinant of the sigma matrix gives the four dimensional rms acceptance of the spiral inflector [79].

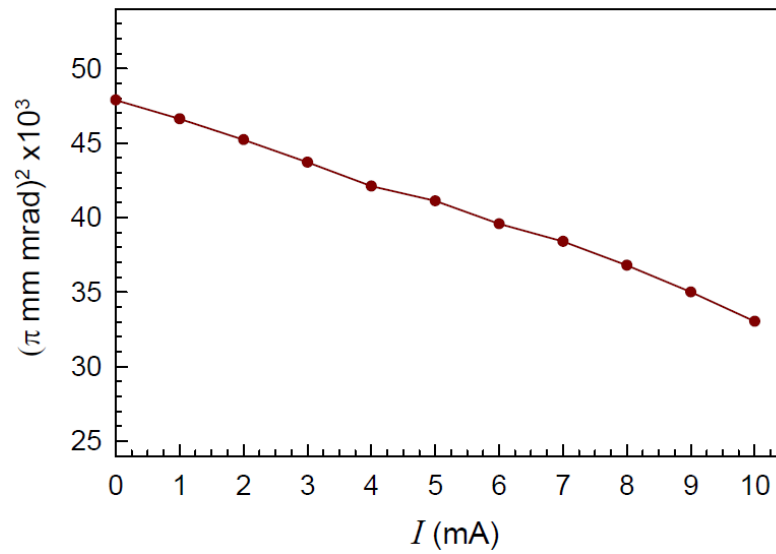


Fig. 4.6. Variation of acceptance as a function of beam current.

Figure 4.6 shows the four dimensional acceptance (16 times rms acceptance) of the spiral inflector as a function of the beam current. Since the other parameters are kept constant, the reduction of the acceptance with beam current is only due to the space charge effect.

4.3.4. Effect of input parameters on beam behaviour

In order to see the effect of space charge and input beam conditions on the paraxial ion trajectories we have tracked 1000 particles through the spiral inflector with equal emittances $60 \pi \text{ mm mrad}$ in both the planes for two values of beam current $I = 0 \text{ mA}$ and

$I = 5$ mA. The results are illustrated in Fig. 4.7. We have considered two cases. In the first case the input beam is axisymmetric with $U = H = 4$ mm and $P_u = P_h = 0$ mrad whereas in the second case the beam is non-axisymmetric with $U = 4$ mm, $H = 2.3$ mm

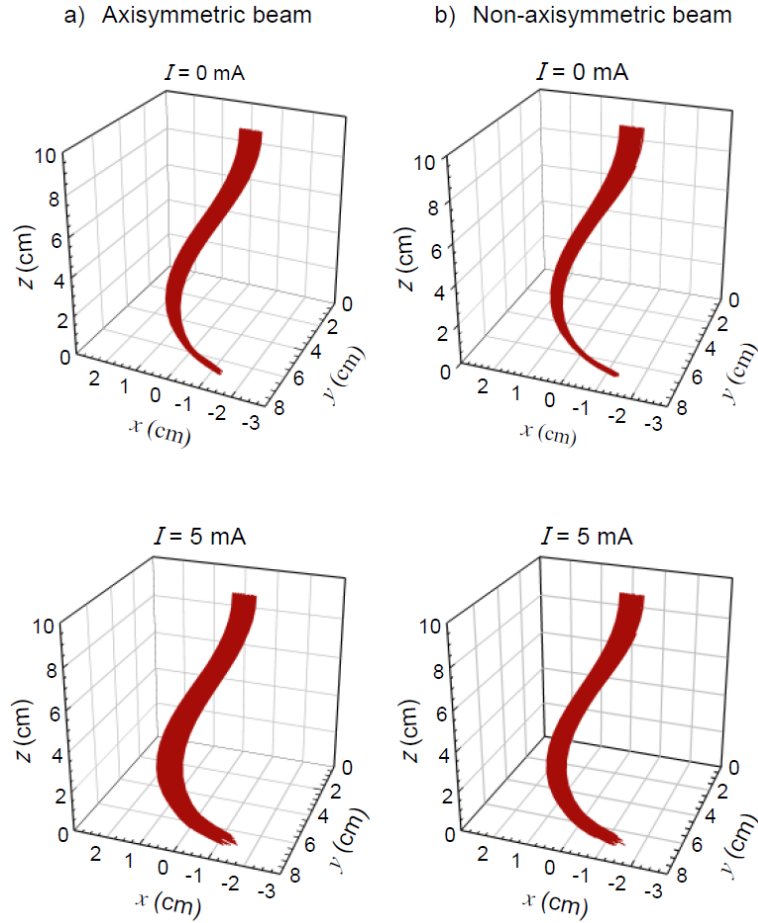


Fig. 4.7. Paraxial trajectories of 1000 particles with equal input emittances 60π mm mrad in both the planes at $I = 0$ mA and $I = 5$ mA. (a) axisymmetric upright ellipse with $U = H = 4$ mm and $P_u = P_h = 0$ mrad (b) non-axisymmetric tilted ellipse with $U = 4$ mm, $H = 2.3$ mm and $P_u = -6$ mrad, $P_h = -31$ mrad (optimized condition of Fig. 4.5).

and $P_u = -6$ mrad, $P_h = -31$ mrad. The space charge effect as well as the influence of input beam conditions is clearly visible on the spiral pattern. It is evident from the figure that the radial expansion of the beam in the case of non-axisymmetric beam is comparatively less at both the values of beam current.

The numerical result plotted in Fig. 4.8 shows the beam cross section consisting of 1000 paraxial trajectories at different locations s/S inside the inflector for the axisymmetric and non-axisymmetric input beams. Here $S = \pi A/2 = 13.58$ cm, is the path length of the central ion trajectory in the inflector. The dynamics of the beam pulsation and rotation caused due to inter-plane coupling and space charge effect is clearly visible in the plots. As mentioned earlier here also we see that non-axisymmetric beam with converging phase ellipse is more suitable for better transmission in the spiral inflector because it occupies less area in $u-h$ planes.

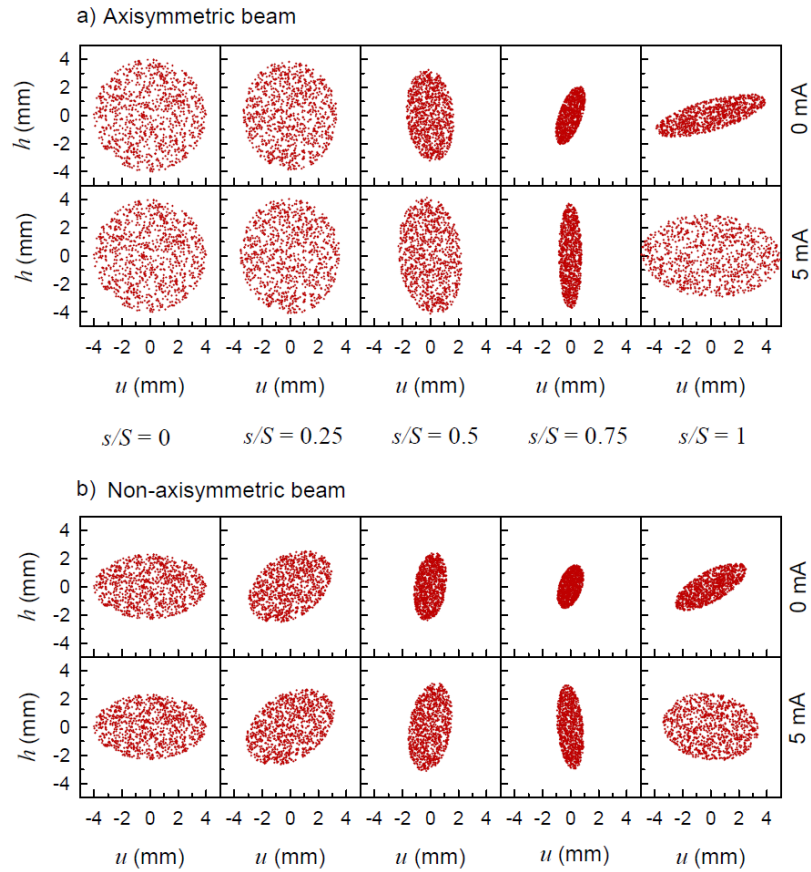


Fig. 4.8. Transverse cross-sections of the beam at different locations in the spiral inflector at $I = 0$ mA and $I = 5$ mA for axisymmetric and non axisymmetric input beams.

Figure 4.9 shows the paraxial ion trajectories and resulting beam envelopes for $I = 0$ mA and $I_{exit} = 5$ mA through the spiral inflector in u and h planes for 40 representative particles belonging to the boundary of the input emittances of 60π mm mrad in each

plane. The dashed curve represents the envelope obtained using the sigma matrix method. It can be readily seen that the envelopes obtained by both the methods are in good agreement. The maximum beam size is limited within 6 mm in both the planes throughout the inflector, much less than the minimum gap of 12 mm between electrodes, which is kept to fulfill the requirement of high beam intensity.

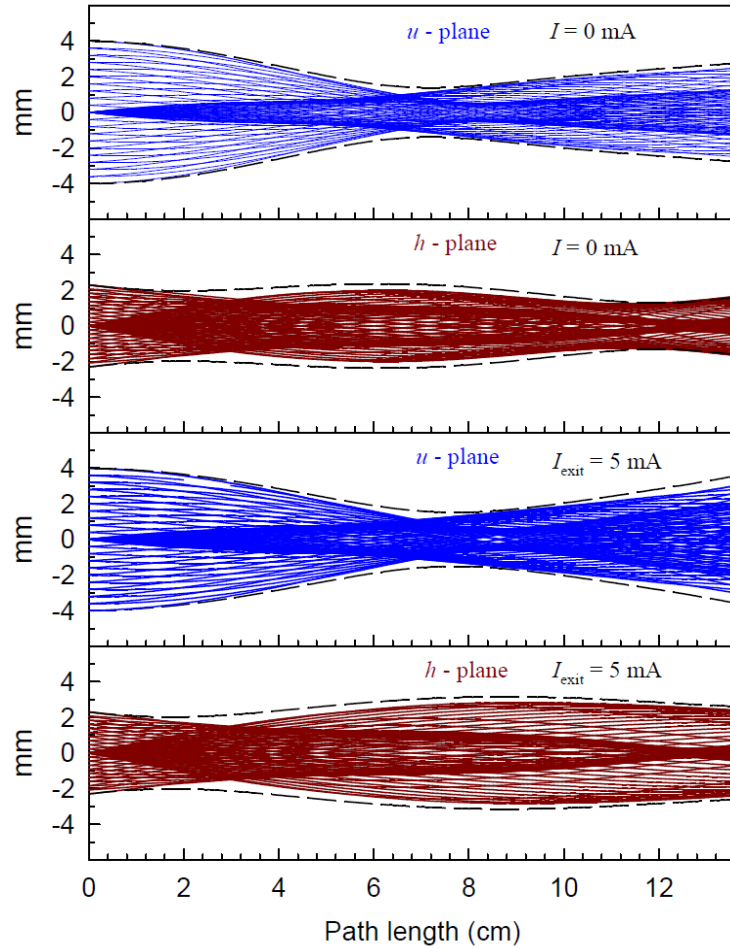


Fig. 4.9. Paraxial ion trajectories and resulting beam envelopes through the spiral inflector in both u and h planes for $I = 0$ mA and $I_{exit} = 5$ mA. Input conditions are optimized.

4.4. Summary

To summarize, we have developed the equations of paraxial ion trajectories to study the space charge dominated beam dynamics assuming the beam as an ellipsoidal bunch. We have also calculated the beam envelopes inside the inflector and emittance growth at

the exit of the inflector using the sigma matrix method. The inclusion of increase of the beam current in the bunch due to bunching action as the beam traverses inside the inflector, produces a significant change in the beam envelope compared to the case when the beam current in the bunch is constant. From the results of ion trajectory calculations we have found that initial emittance conditions have considerable effect on the emittance growth at the exit of the inflector. Results show that space charge effect remains rather weak for beam intensity below 3.0 mA. At higher current above 3.0 mA space charge force is no longer negligible and starts to play a crucial role in the growth of beam envelope and emittance. It is also observed that the initial phase ellipses which correspond to the minimum emittance growth without space charge are not at all suitable when the space charge effect is included. One needs different set of initial phase space ellipses to control the emittance growth at the exit if the beam current is changed.

Chapter 5

Envelope oscillations and amplitude growth in a compact cyclotron

5.1. Introduction

In this Chapter we discuss the investigation on the amplitude growth and oscillations in the beam envelopes along the accelerated orbit in a compact cyclotron cyclotron [7]. We have used the coupled beam envelope equations and assumed the beam to be a uniform ellipsoidal bunch.

The study of the beam behavior in the central region of the cyclotron reveals that beam envelope behaves differently due to the coupling of the horizontal and vertical motions arising due to space charge effects [37]. In order to achieve optimum performance, the emittance and orientation of the phase ellipses of the injected beam must be matched to the acceptance of the central region of the cyclotron. It is believed that envelope mismatch is the major cause of emittance growth and halo formation [44]. For mismatch beams, an unbalance between the applied focusing force and the defocusing forces due to space charge and thermal effects, cause whole beam to oscillate in a coherent way. This effect increases the beam size in both the transverse planes and causes severe beam loss. In the case of low beam current the mismatch in one plane affects the beam behavior only in that particular plane. However, in the case of intense beam, where the space charge effect couples the motions of the two transverse planes, a mismatch in one plane affects the beam behavior in both transverse planes.

In a previous work [37] discussed in Chapter 2 we have studied the effect of space charge in a compact cyclotron to get the proper beam matching conditions at the injection.

We have used transverse envelope equations assuming a uniform continuous beam and an analytical hard edge model for the magnetic field. Since hard edge model of the magnetic field overestimates the vertical betatron tunes at lower radii, the results so obtained are limited in accuracy; however, they provide good insight about the behavior of beam envelopes. We like to point out here that studies on space charge effect in a compact cyclotron above 1 mA beam current are still not well understood and lots of research is going on to resolve the physics and technological issues at high current. Commercial compact cyclotrons operating for medical isotope production are limited to beam current <1 mA. Therefore, to avoid the beam loss, a systematic study of the space charge dominated beam behavior in the focusing channel of a compact cyclotron is of practical importance. This is the main objective of the work presented in this Chapter.

In this Chapter, first we have obtained the values of magnetic and electric betatron tunes and then developed the coupled accelerated beam envelope equations. It is assumed that the beam is a uniform ellipsoidal bunch. First the pattern of envelope oscillations and amplitude growth of the beam in both transverse planes at a particular radius (without acceleration) have been analyzed by displacing the initial beam size from the matched beam size at several values of beam current. Then we have discussed the results of our studies on the behavior of beam envelope in the 10 MeV cyclotron at different initial conditions of the beam. Finally we have obtained the proper matching conditions by optimizing the input beam parameters and also estimated the maximum beam current that can be transported through a given aperture of the cyclotron focusing channel.

5.2. Calculation of Betatron tunes

The design of the magnet of 10 MeV cyclotron has been discussed in Chapter 3. We have obtained the radial and axial betatron tunes from the computed magnetic field data

using the equilibrium orbit (EO) program GENSPEO [39]. The variation of the radial v_x and vertical v_y (magnetic) magnetic betatron tunes as a function of the orbit radius R is shown in Fig. 5.1. During the first few turns in a compact cyclotron, the vertical magnetic focusing is very weak. It is, therefore, necessary to exploit the vertical electric focusing available at the dee gaps by properly adjusting the geometry and phase.

In a cyclotron, the electric field at the acceleration gaps exerts a lens like action in the vertical plane on off-median plane particles during the first few turns. In order to include this effect in the calculations, we have used the first order theory [80] to estimate the electric vertical betatron tune. The electric focusing has negligible effect on the radial motion. We have assumed that particle traverses the electric gaps periodically in a stationary orbit of radius R , without increase of energy (taking the average of initial and final energy at the gaps). As mentioned earlier, the accelerating structure of 10 MeV cyclotron consists of two delta type resonators located in the opposite valleys and each has an angle of $\pi/4$. For a particle displaced from the median plane in the vertical direction, the initial position and slope y_0 and y'_0 at the first gap and final position and slope y and y' at the third gap are related as

$$\begin{pmatrix} y \\ y' \end{pmatrix} = \mathbf{M} \begin{pmatrix} y_0 \\ y'_0 \end{pmatrix} \quad (5.1)$$

$$\mathbf{M} = \begin{pmatrix} 1 & 3\pi R/4 \\ 0 & 1 \end{pmatrix} \begin{pmatrix} 1 & 0 \\ -1/f_2 & -f_1/f_2 \end{pmatrix} \times \begin{pmatrix} 1 & \pi R/4 \\ 0 & 1 \end{pmatrix} \begin{pmatrix} 1 & 0 \\ -1/f_2 & -f_1/f_2 \end{pmatrix} \quad (5.2)$$

where \mathbf{M} is the transfer matrix from the first gap to the third gap. The distance between the first and second gap is $\pi R/4$ whereas the distance between the second and third gap is $3\pi R/4$, where R is the average orbit radius under consideration. The focal length f_1 and f_2 are given by the following expressions:

$$\frac{f_1}{f_2} = \frac{E_c - (qV_g \cos \theta_c)/2}{E_c + (qV_g \cos \theta_c)/2}. \quad (5.3)$$

$$\frac{1}{f_2} = \frac{\pi f_{rf}}{c} \left(\frac{2\pi V_g}{E_0} \right)^{-\frac{1}{2}} \left(\frac{qV_g}{E_c} \right)^{\frac{3}{2}} \sin \theta_c + \frac{F}{2\pi H} \left(\frac{qV_g}{E_c} \right)^2 \cos^2 \theta_c \quad (5.4)$$

where f_{rf} , H and E_0 are the rf frequency, half height of the dee and rest mass energy of the particle respectively. The factor F depends upon the geometry of the dee [80]. A particle with kinetic energy E will gain energy $qV_g \cos \theta_c$ in traversing the first gap and the energy of the particle at the middle of the gap will be $E_c = E + (qV_g \cos \theta_c)/2$ where V_g is the gap voltage and θ_c is the phase of rf when the particle is at the middle of the gap. The electric vertical betatron tune can be obtained from

$$\nu_y = \frac{1}{\pi} \cos^{-1} \left[\frac{1}{2} \text{Tr} \mathbf{M} \right] \quad (5.5)$$

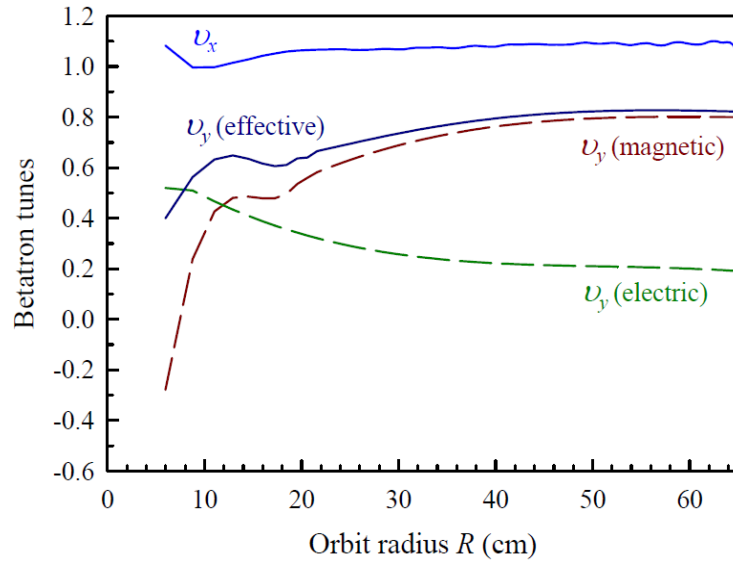


Fig 5.1. Betatron tunes as a function of orbit radius. Dashed curves represent the contribution to the vertical betatron tunes ν_y (solid line) from the electric and magnetic focusing. The initial rf phase θ_c is equal to 5° .

The parameters used in the calculations are: injection energy $E = 80$ keV, dee voltage $V_g = 125$ kV, rf frequency $f_{rf} = 42$ MHz, dee height from the median plane $H = 1.5$ cm

and gap between dee and dummy dee $2W = 2$ cm. The corresponding F factor for this particular dee geometry is 0.82. The electric vertical tune $\nu_y(\text{electric})$ obtained using Eq. (5.5) which is appreciable only at lower radii is shown by dashed line. The effective vertical tune is obtained using the formula, $\nu_y(\text{effective}) = [\nu_y^2(\text{magnetic}) + \nu_y^2(\text{electric})]^{0.5}$ which is obtained by adding the vertical magnetic and electric focusing forces together and using the fact that focusing force is proportional to the square of the tune value. The result is also shown in Fig. 5.1. We have used values of these betatron tunes ν_x and $\nu_y(\text{effective})$ in the beam envelope calculations.

5.3. Accelerated Beam envelope equations

Our main objective in this work is to study the behavior of beam envelopes along the accelerated orbits in the two transverse planes and to estimate the maximum transportable beam current in a given aperture. In order to obtain the coordinates of the path along the accelerated orbits, we performed the orbit tracing in the median plane of the cyclotron by solving the equations of motion in the combined electric and magnetic fields. The coordinates and velocity of the central ion trajectory obtained at the inflector exit were used as input. The accelerated orbits of the proton from 80 keV to 10 MeV in the median plane of the cyclotron is shown in Fig. 3.10 in Chapter 3.

We consider a bunched beam having uniform density distribution with ellipsoidal symmetry propagating along the accelerated orbit in the focusing channel of a compact cyclotron. The method presented here can also be utilized for any beam distribution using the concept of equivalent beams. According to this concept, the beam must have the same second moment as the actual beam distribution [44, 81]. It is well known that the space charge effect on bunches circulating in a cyclotron is very complex. Bunches rotate in the median plane and the rate of rotation depends upon the charge density. For short bunches

the stationary beam distribution shape is circular (*i.e.* bunch length = radial width). In the case, where the injected bunches are much longer azimuthally compared to the radial width, the bunch breaks up into small droplets [82, 83]. Since the charge density and hence the perveance reduces in the case of long bunches for the same beam current compared to the short bunches, this break up takes comparatively longer time [82]. Since in our case the average longitudinal bunch size during the first turn (~ 14 mm) is large compared to the matched radial beam width (~ 5 mm) we have simplified our analysis by neglecting the bunch rotation due to the radial and longitudinal coupling. We have also neglected the effect of axial variation of longitudinal field on the transverse motion. Under these assumptions the bunch shape remains ellipsoidal within the cyclotron. Since the longitudinal bunch size in a cyclotron depends on the location of the equilibrium orbit it will change to a new value after the acceleration at each gap.

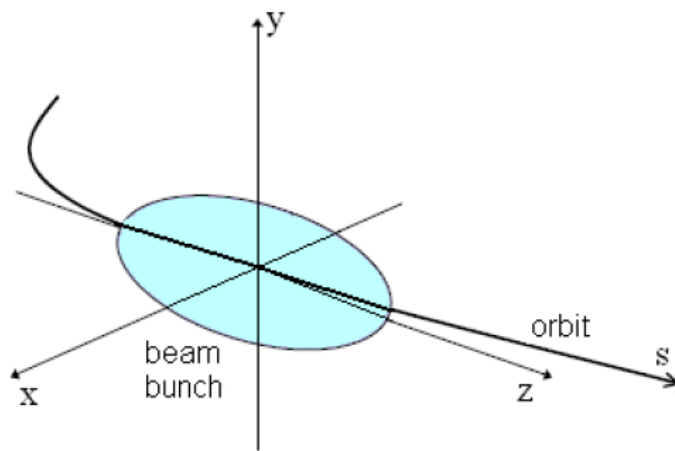


Fig. 5.2. A schematic of coordinate system attached to the beam bunch moving along the accelerated orbit in the median plane.

We now introduce a local coordinate system x , y and z as shown in Fig. 5.2 with the centre of the ellipsoid which moves with velocity v along the accelerated orbit in the median plane. Here x and y are the two transverse coordinates measure the distances from the bunch centre ($x = y = z = 0$) along the radial and vertical directions respectively

whereas z measures distance along the longitudinal direction. The z axis is always tangent to the accelerated orbit. If s be the path length along the accelerated orbit in the median plane from the starting point, then a particle with coordinates (x, y, z) in the beam frame has coordinates $(R + x, y, s + z)$ in the laboratory frame where R is the instantaneous orbit radius from the machine centre. The differential equations for beam envelopes $X(s)$ and $Y(s)$ in the two transverse planes [84, 85] can be written as:

$$X'' + \frac{(\beta\gamma)'}{(\beta\gamma)} X' + \left[\frac{\nu_x^2}{R^2} - \frac{3Ic}{2I_0\beta^2\gamma^3 f_{rf}} \frac{1}{X^3} G1\left(\frac{Y}{X}, \frac{Z}{X}\right) \right] X - \frac{\varepsilon_{nx}^2}{\beta^2\gamma^2 X^3} = 0 \quad (5.6)$$

$$Y'' + \frac{(\beta\gamma)'}{(\beta\gamma)} Y' + \left[\frac{\nu_y^2}{R^2} - \frac{3Ic}{2I_0\beta^2\gamma^3 f_{rf}} \frac{1}{Y^3} G2\left(\frac{X}{Y}, \frac{Z}{Y}\right) \right] Y - \frac{\varepsilon_{ny}^2}{\beta^2\gamma^2 Y^3} = 0 \quad (5.7)$$

and the average beam current I as

$$I = \frac{4}{3} \pi XYZ n_b q f_{rf} = Q_b f_{rf} \quad (5.8)$$

Here $X(s)$, $Y(s)$ and $Z(s)$ are the semi axes of the ellipsoid, which are also the envelope sizes in the x , y and z directions respectively. Q_b is the total charge in the bunch assumed to remain constant during the motion, f_{rf} is the rf frequency, R is the average orbit radius, ν_x and ν_y are the betatron tunes and ε_{nx} and ε_{ny} are the normalized emittances of the beam in the x and y planes respectively. $I_0 = 4\pi\varepsilon_0 mc^3 / q$ is the characteristic current and for proton, $I_0 = 31$ MA. The second term in both the envelope equations (5.6) and (5.7) represent the acceleration effect and prime denotes the differentiation with respect to s . Integrals, $G1$ and $G2$ in eqs. (5.6) and (5.7) can be expressed in terms of the elliptic integrals of the first kind $F(\alpha, p)$ and second kind $E(\alpha, p)$. The form of these integrals depends on the relative magnitude of the envelope functions. For the ellipsoid with $X < Y < Z$, the integrals $G1$ and $G2$ have the form:

$$G1\left(\frac{Y}{X}, \frac{Z}{X}\right) = -\frac{2X^3 E(\alpha, p)}{(Y^2 - X^2)\sqrt{(Z^2 - X^2)}} + \frac{2X^2 Y}{Z(Y^2 - X^2)} \quad (5.9)$$

$$G2\left(\frac{X}{Y}, \frac{Z}{Y}\right) = \frac{2Y^3 \sqrt{(Z^2 - X^2)}}{(Z^2 - Y^2)} \left[\frac{E(\alpha, p)}{(Y^2 - X^2)} - \frac{F(\alpha, p)}{(Z^2 - X^2)} \right] - \frac{2XY^2}{Z(Y^2 - X^2)} \quad (5.10)$$

where α , p and the integrals $F(\alpha, p)$ and $E(\alpha, p)$ are given by

$$\alpha = \sin^{-1} \left(1 - \frac{X^2}{Z^2} \right)^{1/2}, \quad p = \left(\frac{Z^2 - Y^2}{Z^2 - X^2} \right)^{1/2},$$

$$F(\alpha, p) = \int_0^\alpha \frac{dx}{\sqrt{(1 - p^2 \sin^2 x)}}, \quad E(\alpha, p) = \int_0^\alpha \sqrt{(1 - p^2 \sin^2 x)} dx. \quad (5.11)$$

For oblate ellipsoid and spheroid with different relative magnitudes of X , Y and Z , integrals $G1$ and $G2$ have been obtained using the standard integrals given in ref. [86].

The transverse envelope equations with acceleration and linear focusing forces for a long uniform continuous beam having elliptical symmetry [87] can be expressed as

$$X'' + \frac{(\beta\gamma)'}{\beta\gamma} X' + \frac{v_x^2}{R^2} X - \frac{4I}{I_0 \beta^3 \gamma^3} \frac{2\pi}{\Delta\phi} \frac{1}{(X+Y)} - \frac{\epsilon_{nx}^2}{\beta^2 \gamma^2 X^3} = 0 \quad (5.12)$$

$$Y'' + \frac{(\beta\gamma)'}{\beta\gamma} Y' + \frac{v_y^2}{R^2} Y - \frac{4I}{I_0 \beta^3 \gamma^3} \frac{2\pi}{\Delta\phi} \frac{1}{(X+Y)} - \frac{\epsilon_{ny}^2}{\beta^2 \gamma^2 Y^3} = 0 \quad (5.13)$$

The term $(2\pi/\Delta\phi)$ is included with the beam current I to account for the phase acceptance in the central region. Knowing the functional dependence of the focusing strength and $(\beta\gamma)' / (\beta\gamma)$ along the path length s , one can easily obtain the evolution of envelopes around the central ion trajectory in the median plane of the cyclotron. The space charge term couples the envelope equations, and hence plays an important role in the evolution of envelopes $X(s)$ and $Y(s)$, particularly when the beam current is sufficiently large. For low beam current and without acceleration there are special solutions of Eqs. (5.6) and (5.7), where $X = X_m = \text{const.}$ and $Y = Y_m = \text{const.}$ and are given by

$$X_m = \sqrt{\frac{\varepsilon_{nx} R}{\beta\gamma v_x}}, \quad Y_m = \sqrt{\frac{\varepsilon_{ny} R}{\beta\gamma v_y}} \quad (5.14)$$

These correspond to the so called matched solutions for which the beam envelope sizes preserve the initial shape throughout its path *i.e.* beam envelopes are straight lines. The matched solutions with space charge terms and without acceleration, can be obtained by solving the following coupled equations simultaneously

$$\frac{v_x^2}{R^2} X - \frac{3Ic}{2I_0\beta^2\gamma^3 f_{rf}} \frac{1}{X^2} G1\left(\frac{Y}{X}, \frac{Z}{X}\right) - \frac{\varepsilon_{nx}^2}{\beta^2\gamma^2 X^3} = 0 \quad (5.15)$$

$$\frac{v_y^2}{R^2} Y - \frac{3Ic}{2I_0\beta^2\gamma^3 f_{rf}} \frac{1}{Y^2} G2\left(\frac{X}{Y}, \frac{Z}{Y}\right) - \frac{\varepsilon_{ny}^2}{\beta^2\gamma^2 Y^3} = 0 \quad (5.16)$$

In the case of space charge dominated beam together with acceleration it is not possible to obtain the matched sizes. In such situation one needs to solve Eqs. (5.6) and (5.7) for beam envelopes along the path of the accelerated orbit and then to optimize the initial conditions for which the envelopes $X(s)$ and $Y(s)$ exhibit minimum amplitude of oscillations.

5.4. Numerical results and discussions

In this section we present the results of studies on behavior of the beam envelopes in the focusing channel of the 10 MeV compact cyclotron under various initial conditions of the beam parameters. We performed numerical solutions of Eqs. (5.6) and (5.7) and tried to optimize the input beam conditions in the presence of space charge to get the beam envelopes within the specified acceptance in the 10 MeV cyclotron. We have used same values for emittances equal 60π mm mrad in both the planes in the present calculation. This is the typical value of the emittance one expects at the injection radius in the cyclotron after transporting and inflecting the beam by a spiral inflector using the microwave ion source. The values of $(\beta\gamma)' / (\beta\gamma)$ have been estimated from the change of energy of the accelerated particle along the path length s using the orbit integration code.

Figure 5.3(a) shows the variation of $(\beta\gamma)' / (\beta\gamma)$ as a function s up to five turns. The bunch size corresponding to 30° of rf phase at the injection energy of 80 keV and rf frequency of 42 MHz, is equal to 8 mm. Therefore, we have chosen the initial value of the longitudinal semi axis of the ellipsoidal bunch equal to 4 mm. As the beam energy increases the bunch size also increases along the longitudinal direction. The variation of bunch size $2Z$ as a function of the path length s for five turns is shown in Fig. 5.3(b). This change of bunch size has been incorporated while solving Eqs. (5.6) and (5.7) along the accelerated orbits of the beam.

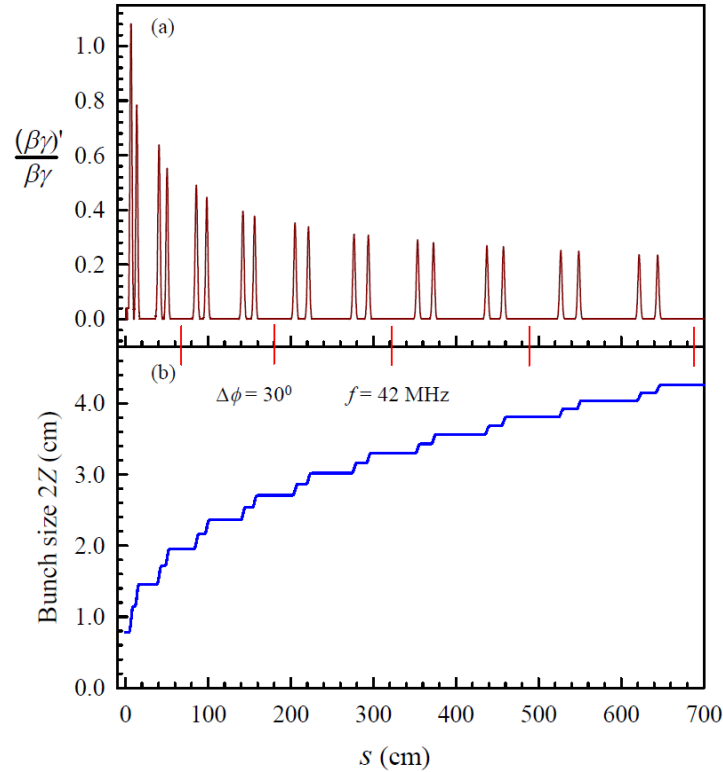


Fig. 5.3. The variation of (a) $(\beta\gamma)' / (\beta\gamma)$ and (b) bunch size $2Z$ as a function path length s along the accelerated orbits up to five turns. Long ticks on the middle horizontal line indicate the turn number. There are four kicks at four acceleration gaps in each turn.

5.4.1. Beam envelopes in a particular orbit

To understand the beam envelopes behaviour along the accelerated orbits we have first explored the beam envelopes under various conditions at a particular orbit radius of 30 cm (it can be any radius) without including the acceleration effects in the envelope equations.

We obtained the matched beam sizes at this radius for three different values of beam current using Eqs. (5.14) to (5.16). The calculated matched beam sizes in the radial and vertical planes are 1.71 mm and 1.98 mm for 0 mA, 1.92 mm and 2.38 mm for 5 mA and 2.11 mm and 2.84 mm for 10 mA respectively as shown by the dotted lines in Fig. 5.4.

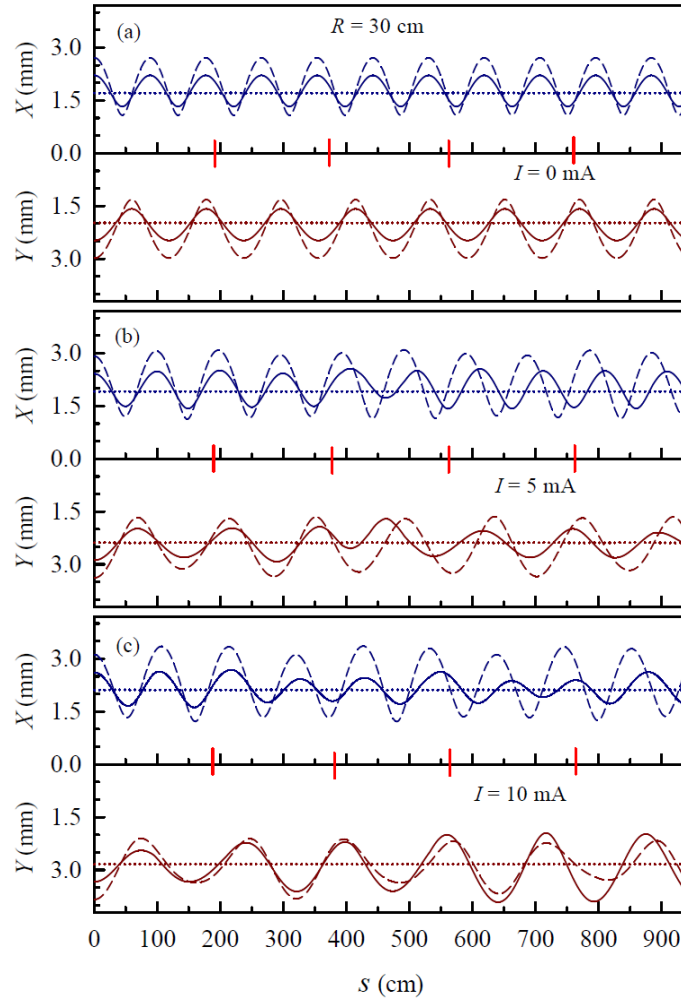


Fig. 5.4. Radial and vertical beam envelopes, for different initial conditions at radius 30 cm without acceleration for five revolutions and three different values of beam current. Matched beam sizes are shown by dotted lines. All solid curves represent mismatch by 0.5 mm from the matched beam size whereas dashed curves represent mismatch by 1.0 mm from the matched beam size. The values of the matched beam sizes are (a) $X_m = 1.71$ mm, $Y_m = 1.98$ mm for 0 mA, (b) $X_m = 1.92$ mm, $Y_m = 2.38$ mm for 5 mA and (c) $X_m = 2.11$ mm, $Y_m = 2.84$ mm for 10 mA.

We then studied the envelope evolution for five revolutions by changing the initial beam sizes by 0.5 mm and 1.0 mm from the matched values in all the above mentioned

three cases. Results are shown in Fig. 5.4. In the case of $I = 0$ mA, the patterns of the envelope oscillations in each plane are similar for the two values of displaced initial beam sizes. The number of oscillations per turn in the radial plane is equal to 2.12 which is twice the value of betatron tune $\nu_x = 1.06$ and follows the linear theory of envelope oscillations described in detail for solenoid and quadrupole focusing channels [44, 88]. Similarly in the vertical plane where $\nu_y = 0.8$, there are 1.6 oscillations per turn. These numbers of oscillations are independent of the displacement of the initial beam size from the matched value, however, the amplitudes of oscillations are different.

It is readily seen from Fig. 5.4(b) and 5.4(c) that the envelope oscillations pattern is completely different in both the planes when the space charge effect is included in the calculations. We observed the decrease in the number of oscillations per turn as the beam current is increased and a marginal increase in the number of oscillations as the beam size from the matched radius is increased. This behavior is due to the fact that with increase in the beam current there is a depression in the tune values and hence the decrease in the number of oscillations. However it is difficult to predict the exact behavior of these oscillations due to mixture of two modes of oscillations because of different values of betatron tunes in the two transverse planes.

We have also studied the envelope behaviors by increasing and decreasing the beam sizes from the matched beam size in one plane and keeping the beam size fixed in the other plane equal to the matched size. In the case of $I = 0$ mA, as expected, we did not observe any change in the envelope of y plane due to mismatch in the x plane and vice versa. However, with beam current, a mismatch in x plane not only produced oscillations in the x plane but also produced a small ripples in the y plane and vice versa. We observed this effect in the case of 5 mA and 10 mA beam current which is due to the fact that space charge term couples the two transverse motions. The behavior of envelopes in

x and y planes around the matched beam sizes (dotted line) under various conditions is shown in Fig. 5.5 for 5 mA beam current.

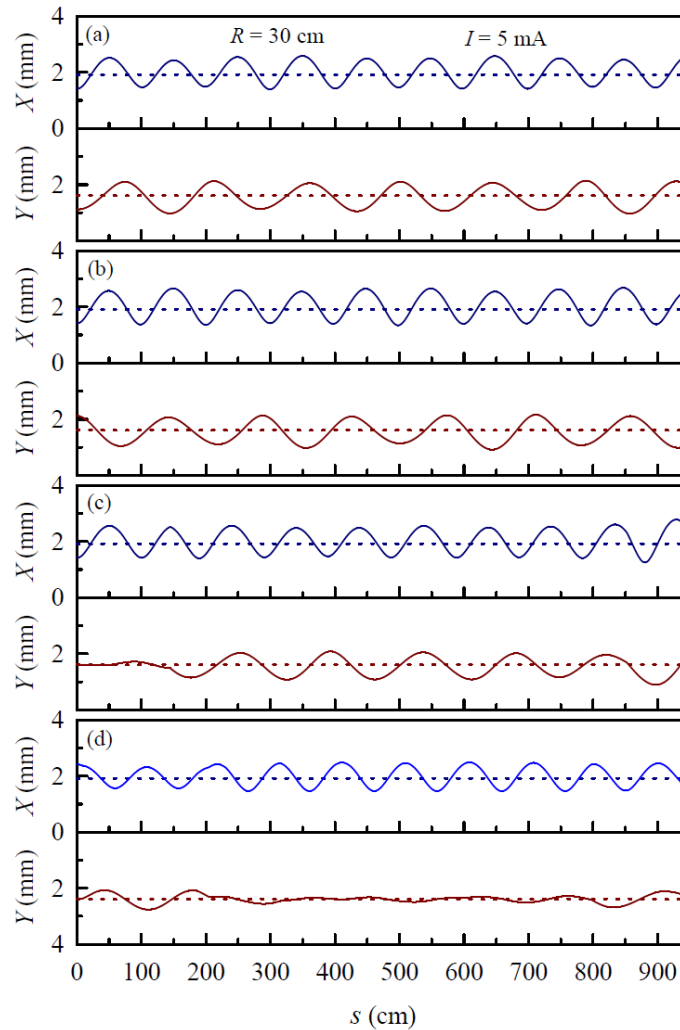


Fig. 5.5. Radial and vertical beam envelopes without acceleration, for different initial conditions at radius 30 cm for five revolutions at $I = 5$ mA beam current. Dotted lines represent the matched envelope sizes $X_m = 1.92$ mm and $Y_m = 2.38$ mm. The beam envelopes are for (a) $X = X_m - 0.5$ mm, $Y = Y_m + 0.5$ mm, (b) $X = X_m - 0.5$ mm, $Y = Y_m - 0.5$ mm, (c) $X = X_m - 0.5$ mm, $Y = Y_m$, (d) $X = X_m + 0.5$ mm, $Y = Y_m$.

In Fig. 5.5(a) the initial beam sizes in x plane is reduced by 0.5 mm whereas in y plane it is increased by 0.5 mm from the corresponding matched beam sizes. In this case the envelope oscillations start initially with so called “out of phase” mode, quickly change to “in phase” mode and then again to “out of phase” mode and so on. This mixed mode of oscillation is due to the fact that betatron tunes in both planes are different and hence the

number of oscillations per turn. Fig. 5.5(b), in which the initial beam sizes in both x and y planes are reduced by 0.5 mm from the matched beam sizes, shows the almost identical behavior where the initial oscillations start first with “in phase” mode and keep on changing between the two modes along the path length. In Fig. 5.5(c) and 5.5(d) we have shown the behavior of envelope oscillations where the initial beam sizes in y plane is kept equal to matched beam sizes and in x plane the beam size is decreased by 0.5 mm in one case and increased by 0.5 mm in other case from the matched sizes. Here we observe that the induced envelope oscillations in y plane are completely different in both cases.

5.4.2. Beam envelopes along accelerated orbit

Now we will discuss about the behaviour of the beam envelopes along the accelerated orbits in the 10 MeV cyclotron. Since there is a wide variation of betatron tunes with radius in a cyclotron as shown in Fig. 5.1, the calculated matched beam sizes at different orbit radii are also different. Figure 5.6 shows the variation of matched beam sizes X_m and Y_m in the radial and vertical planes respectively as a function of the orbit radius for various values of the beam current. The increase in the matched beam sizes with beam current in both the cases is due to the depression in tune values with beam current. Since the matched beam sizes at different orbit radii are not same, it is not possible to find out a unique matched beam sizes at the injection radius. The matching of the beam size at one radius automatically becomes an un-matched beam size at other radii and hence produce oscillations as well as growth in the beam envelopes. It is well known that amount of beam current that can be transported through a focusing channel is a maximum when the beam is perfectly matched to the acceptance of the channel. It is not possible to obtain such condition in a cyclotron focusing channel. Therefore, one needs to optimize the initial

beam conditions in both the planes at the injection radius to reduce the amplitude growth and envelope oscillations as minimum as possible throughout the focusing channel.

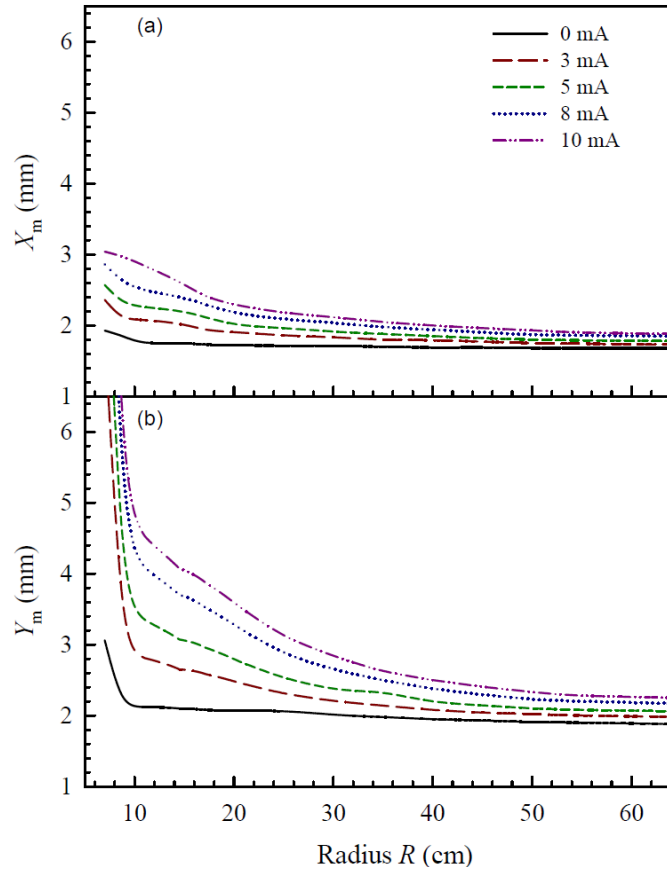


Fig. 5.6. Variation of matched beam envelope sizes X_m and Y_m as a function of orbit radius for various values of beam current.

The beam envelopes in the two transverse planes as a function of distance s along the accelerated orbit for beam current $I = 0$ mA are shown in Fig. 5.7(a). The initial beam sizes used here are the matched beam sizes $X_m = 1.92$ mm and $Y_m = 3.26$ mm at the injection radius (7.05 cm). We see that due to the acceleration there is a large growth in the amplitude of the envelope oscillations in both the planes together with a distinct slow modulation on the radial beam envelope amplitude. It is clear that these initial conditions are not at all suitable. In order to reduce the amplitude of oscillations we studied the behavior of the envelopes by changing the input beam conditions. Figure 5.7(b) shows the optimized envelopes after adjusting the initial beam sizes as well as orientations of the

phase ellipses in both the planes. There is a substantial reduction in the envelope amplitude with these initial conditions. The pattern of modulation on the amplitude is also altered with the reduction in the frequency of modulation.

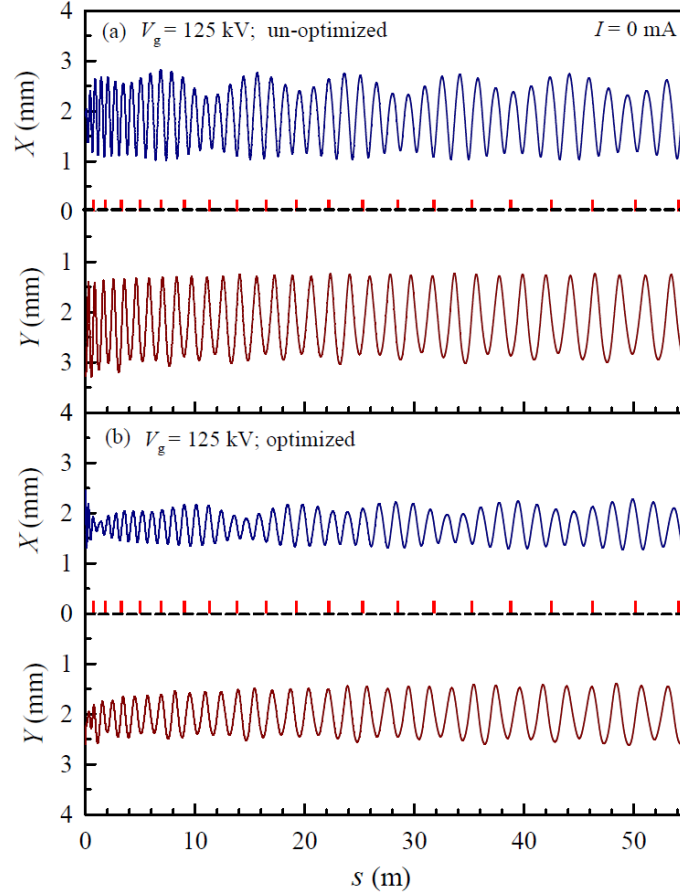


Fig. 5.7. Beam envelopes along the path of the accelerated orbits up to final radius for $I = 0$ mA. (a) The initial beam sizes are the matched beam sizes $X_m = 1.92$ mm and $Y_m = 3.26$ mm at the injection radius (7.05cm) in both the planes. (b) Envelopes obtained after optimization of initial beam conditions to yield minimum amplitude of oscillations in the beam envelopes. Ticks on the horizontal central line indicate the number of turns.

The behavior of beam envelopes for 5 mA is shown in Fig. 5.8. The input conditions of the beam in Fig. 5.8(a) are the same as that of optimized input conditions of $I = 0$ mA. As we see these input conditions produce more amplitude of oscillations in the beam envelopes. At different values of beam current the pattern of oscillations are different. The optimized beam envelopes are shown in Fig. 5.8(b) after further adjusting the initial beam conditions at the injection radius. Figure 5.9 shows the phase ellipses in the radial and

vertical directions used as initial conditions for beam current $I = 0$ mA and $I = 5$ mA. It is to be pointed out here that orientations of the phase ellipses and beam sizes at the injection are very crucial parameters and need to be adjusted properly each time, if the beam current is changed. For different values of the beam current, the orientation of the phase ellipses are different in both the planes to yield minimum growth in the amplitude of beam envelope oscillations.

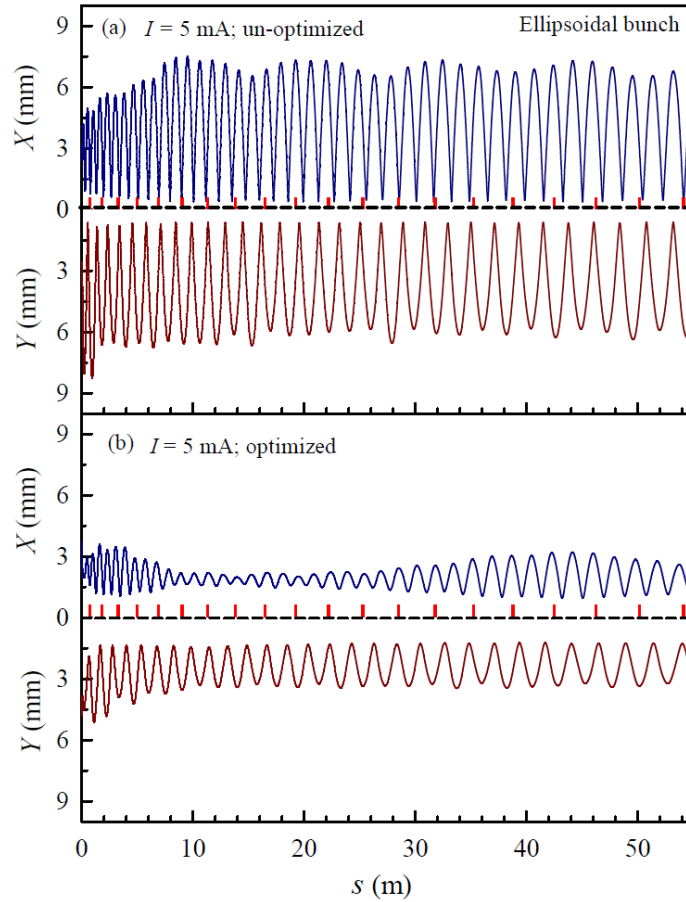


Fig. 5.8. Radial and vertical beam envelopes along the path of the accelerated orbit up to final radius for $I = 5$ mA. (a) The initial beam sizes are the optimized sizes with $I = 0$ mA; $X_0 = 2.4$ mm, $X'_0 = -7$ mrad in the radial plane and $Y_0 = 2.6$ mm, $Y'_0 = -10$ mrad in the vertical plane at the injection radius. (b) Envelopes obtained after optimization of initial beam conditions to yield minimum oscillation in the envelopes ($X_0 = 3.7$ mm, $X'_0 = -27$ mrad, $Y_0 = 4.8$ mm, $Y'_0 = -32$ mrad).

A comparison of the behavior of envelopes of uniform ellipsoidal bunch with that of a uniform continuous beam obtained by solving Eqs. (5.12) and (5.13) shows the patterns of

oscillations almost similar. However, the growth in the amplitude is less in the case of a uniform cylindrical beam. This kind of result is expected because for the same value of beam current in a given phase width, the charge density and hence the space charge defocusing force is more in the case of ellipsoidal bunch. Since ellipsoidal bunch is more close to the laboratory beam, we can say that the uniform cylindrical beam underestimates the space charge effects.

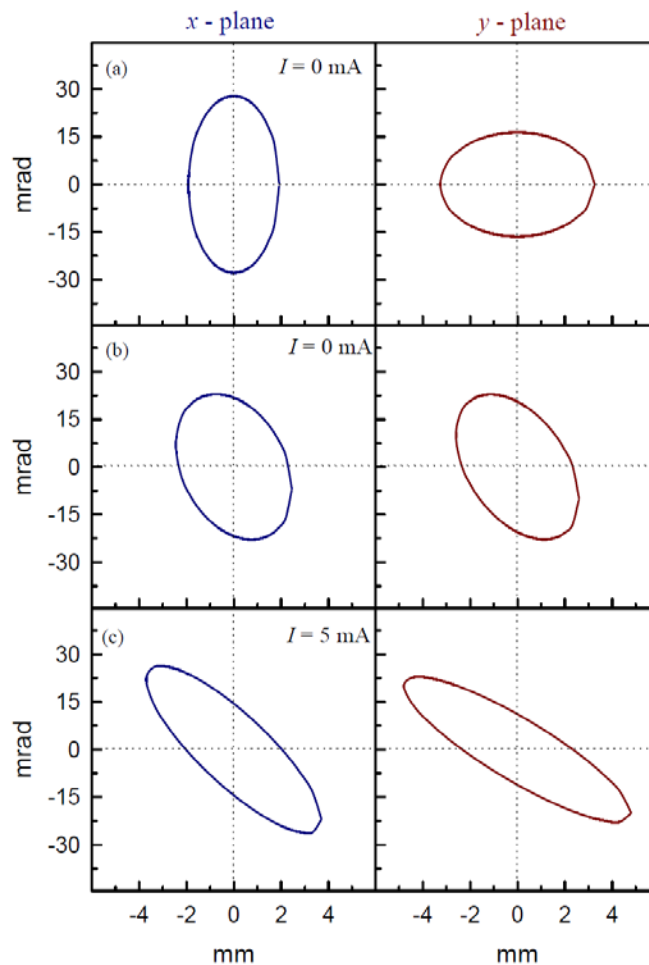


Fig. 5.9. Input phase ellipses in x and y planes for (a) matched envelope sizes at injection radius for $I = 0$ mA (Fig 5.7(a)), (b) the optimized envelopes with acceleration and $I = 0$ mA (Fig 5.7(b)), (c) the optimized envelopes with acceleration and $I = 5$ mA (Fig 5.8(b)).

5.4.3. Estimation of limiting current

We have also estimated the maximum transverse limiting current that can be transported through the focussing channel of the 10 MeV cyclotron within 6 mm half

aperture. **Figure 5.10(a)** shows the radial and vertical beam envelopes along the accelerated orbits up to 21 turns with optimized initial conditions for ellipsoidal beam. In the case of ellipsoidal bunch the limiting current is approximately 7 mA. The limiting current in the case of uniform continuous beam is slightly higher *i.e.* 8.2 mA. These limiting currents can be increased if we remove the restriction on the aperture sizes from 6 mm. We have also carried out optimization of the beam envelope by varying the normalized beam emittances from 0.5 to 1.5 π mm mrad and found that the limiting current reduces slightly with the increase in the beam emittance. At normalized emittances of 0.5, 0.7, 1.0, 1.2, 1.5 π mm mrad the limiting currents, whose beam envelopes remain within 6 mm in both planes, are 7.2 mA, 7 mA, 6.6 mA, 6.3, mA and 6.1 mA respectively.

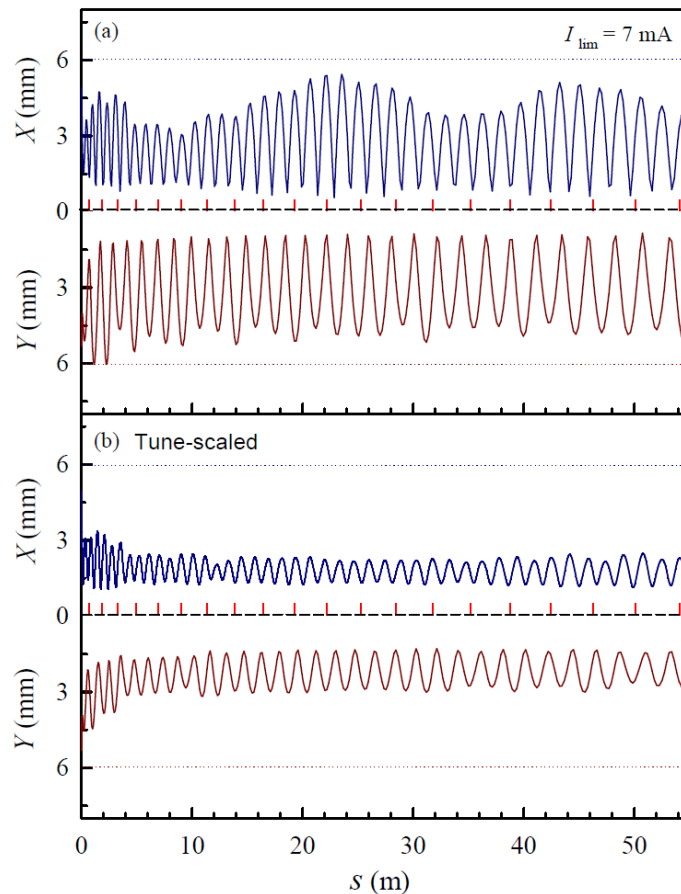


Fig. 5.10. Radial (X) and vertical (Y) beam envelopes along the accelerated orbits up to 10 MeV. (a) uniform ellipsoidal bunched beam with initial conditions $X_0 = 4.9$ mm, $X'_0 = -30$ mrad, $Y_0 = 5.3$ mm, $Y'_0 = -35$ mrad and (b) envelopes when the betatron tunes are scaled of by 1.15 times with same initial conditions as in (a).

The vertical blow up of the beam near the injection caused by the small tune value is the main factor responsible for the limiting current. In our design, the chosen maximum height of the dee from the median plane is equal to 15 mm. Therefore, a 5 mA beam current can be comfortably injected and accelerated in the present design of the cyclotron.

We believe that slow modulation on the radial beam envelope (X) is due to the betatron tune ν_x , which is very close to one at the lower radii. A scaling of ν_x either up or down from the present value reduces the amplitude as well as these oscillations considerably.

Fig 5.10(b) shows the envelope patterns where the ν_x and ν_y are scaled up by a factor of 1.15. In a compact cyclotron, one can easily manipulate the values of vertical tune ν_y by changing the flutter and the shape of sectors. It is not possible to change the profile of the radial tune ν_x as desired in an isochronous cyclotron because it follows the profile of relativistic term γ as the energy of the beam increases. This value remains very close to unity at lower radii where the beam energy is not sufficiently relativistic. The best way to control the beam envelope oscillations and amplitude growth is then to optimize the initial beam conditions properly.

Till now we have discussed the beam optimization in the focusing channel of the cyclotron and results indicate that for maximum beam transmission one needs converging initial phase ellipses in both the transverse planes. However, in reality it is difficult to get such initial conditions because the spiral inflector which is used to inject the beam in the central region puts severe restrictions on the beam emittance due to inter-plane coupling effect. Generally the optimum phase ellipse in the vertical direction at the inflector exit is diverging. The optimized phase ellipses at the exit of the inflector are shown in **Fig. 5.11(a)** and **5.11(b)** for equal input emittances of 45π mm mrad in both the planes. It can be readily seen that there is a substantial growth of emittances in both the planes and the

orientations of phase ellipses are also different. The behavior of beam envelopes in x and y planes with these input conditions of the beam are shown in Fig. 5.11(c). Here we see that there is a slight reduction in the beam current ($I_{lim} = 5.3$ mA) within the specified 6 mm half aperture sizes in both the planes.

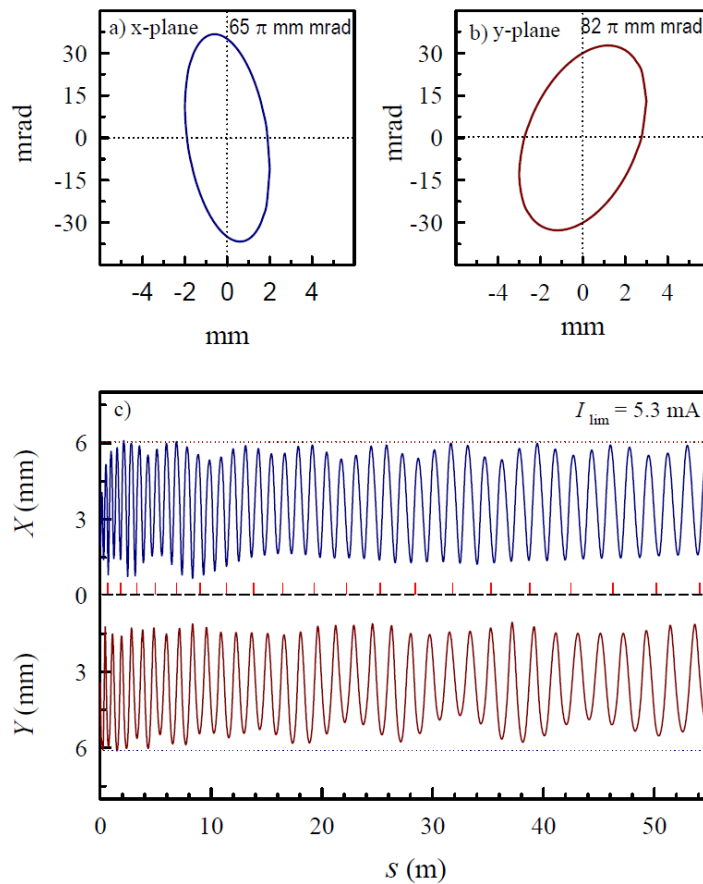


Fig. 5.11. Optimized phase ellipses at the exit of spiral inflector in the central region of 10 MeV cyclotron and beam envelopes in x and y planes along the accelerated orbits with these input beam conditions.

5.5. Summary

The behavior of transverse beam oscillations has been studied in a compact cyclotron along the accelerated orbits for space charge dominated beam. The emphasis has been on the determination of the input beam conditions at the injection to reduce the oscillations and amplitude growth in both the transverse planes. The most important conclusion that

can be extracted from this study is the critical dependence of the input beam conditions on the injected beam current. Our results suggest that for different values of beam current, the beam sizes and orientations of the phase ellipses are different in both the transverse planes that lead to the minimum amplitude growth in envelope oscillations.

The evolution of beam bunch in the combined electric and magnetic fields of a cyclotron is very complex due to the coupling between the radial and longitudinal motions which leads to the rotation of the bunch. In this work we have presented a simplified model and results so obtained present a good insight about the behavior of the transverse motion of the space charge dominated beam with uniform density distribution in a compact cyclotron.

Chapter 6

Elliptical solenoid and matching of intense beam to the spiral inflector

6.1. Introduction

Since the overall goal of this thesis is to maximize the amount of beam that can be injected into the cyclotron, a transverse beam matching at the inflector entrance is thus necessary. Results of beam dynamics in a spiral inflector carried out in Chapter 4, indicate that convergent phase ellipses with different orientations in x and y planes and a comparatively smaller width in the y plane give better beam transmission. The transformation of an axisymmetric beam from the ion source to a non-axisymmetric beam at the entrance of the spiral inflector can't be achieved by using cylindrical symmetric magnets such as Glaser and solenoid magnets as used in our transport line. In this case one needs either an elliptical solenoid [89-91] or a quadrupole doublet. In our case an elliptical solenoid is more suitable than the quadrupole doublet due to space constraint.

In this Chapter, first we discuss the beam optical properties of an elliptical solenoid magnet in the presence of linear space charge effects, as the beam passes through it. Then we present the feasibility of using an elliptical solenoid in the solenoid based low energy beam transport line of our 10 MeV cyclotron to match the beam at the input of the spiral inflector [92]. Generally the Kapchinskij-Vladimirskij (K-V) beam envelope equations [93] are used to understand the high intensity beam dynamics and evolution of beam envelope through a transport system. However, these equations can be used only in an uncoupled lattice i.e. where the two transverse motions are uncoupled. In the case of an

elliptical solenoid it is not straight forward to decouple the two transverse motions and hence the applications of K-V beam envelope equations are difficult [102].

A simple way to study the dynamics of intense beam in the elliptical solenoid is to find out the transfer matrix of it in the presence of space charge effect. Since both equations of motion and beam envelope quantities are coupled with each other, it is not easy to obtain the transfer matrix analytically. In such situations a convenient way is to follow the infinitesimal transfer matrix approach [81, 94]. We have obtained the paraxial ray equations of motion in the combined fields of elliptical solenoid and space charge. From these paraxial equations we have obtained the infinitesimal transfer matrix of an elliptical solenoid for a non-axisymmetric beam and at the same time we have also calculated the beam envelope through the magnet by employing the recursive sigma matrix method [81].

6.2. Theoretical analysis

Consider a space charge dominated continuous beam propagating through the magnetic field \vec{B} of an elliptical solenoid with average axial velocity $v = \beta c$ where β is the relativistic parameter and c is the speed of light in vacuum. In the laboratory frame, we use a right handed Cartesian coordinate system x, y and z with unit vectors \hat{x}, \hat{y} and \hat{z} respectively. As it is customary in accelerator physics we use $s = z$, the distance along the axial direction aligned with the beam axis and x, y represent the transverse coordinates from the beam axis. In the present analysis we assume that the particle trajectory will remain very close to the axis and transverse beam sizes $X = 2\sqrt{\langle x^2 \rangle}$ and $Y = 2\sqrt{\langle y^2 \rangle}$ in x and y directions are very small compared to the radii of beam pipes, coils etc. where $\langle \dots \rangle$ denotes a transverse statistical average over the beam distribution function. We also assume that the transverse velocities are much smaller compared to the average axial velocity of the particles (i.e. $\dot{x}, \dot{y} \ll v$).

6.2.1. Potential for elliptical solenoid

The magnetic field and its components in an elliptical solenoid can be obtained by solving the Laplace equation for magnetic potential Φ in a cylindrical coordinate system

$$\frac{1}{r} \frac{\partial}{\partial r} \left(r \frac{\partial \Phi}{\partial r} \right) + \frac{1}{r^2} \left(\frac{\partial^2 \Phi}{\partial \theta^2} \right) + \frac{\partial^2 \Phi}{\partial s^2} = 0 \quad (6.1)$$

For two fold geometrical symmetry with respect to $\theta = 0$ and $\theta = \pi/2$ such as the case of elliptical solenoid, the general solution of Eq. (1) can be written as

$$\Phi(r, \theta, s) = \sum_{l=0}^{\infty} \sum_{m=0}^{\infty} \Phi_{2l, 2m}(s) r^{2l} \cos(2m\theta) \quad (6.2)$$

By substituting Eq. (6.2) in (6.1) and comparing the coefficients of r and θ for all values of l and m , which satisfy the recursion relations of both r and θ simultaneously, we find that all $\Phi_{2,4} = \Phi_{2,6} = \Phi_{2,8} = \dots = 0$ as well as all $\Phi_{0,2} = \Phi_{0,4} = \Phi_{0,6} = \dots = 0$. The other coefficients can be obtained using the recursion relations. The general solution (6.2) can now be expressed as

$$\begin{aligned} \Phi(r, \theta, s) = & \Phi(0, s) - \Phi^{(2)}(0, s) \left(\frac{r}{2} \right)^2 + \frac{\Phi^{(4)}(0, s)}{4} \left(\frac{r}{2} \right)^4 - \dots \\ & + \left[4\Phi_{2,2}(0, s) - \frac{4\Phi_{2,2}^{(2)}(0, s)}{3} \left(\frac{r}{2} \right)^2 + \frac{4\Phi_{2,2}^{(4)}(0, s)}{24} \left(\frac{r}{2} \right)^4 - \dots \right] \times \left(\frac{r}{2} \right)^2 \cos(2\theta) \\ & + \left[16\Phi_{4,4}(0, s) - \frac{16\Phi_{4,4}^{(2)}(0, s)}{5} \left(\frac{r}{2} \right)^2 + \frac{16\Phi_{4,4}^{(4)}(0, s)}{60} \left(\frac{r}{2} \right)^4 - \dots \right] \times \left(\frac{r}{2} \right)^4 \cos(4\theta) \\ & + \dots \end{aligned} \quad (6.3)$$

where $\Phi^{(n)}$ denotes the n-th derivative of Φ with respect to the axial distance s . Since in Eq. (6.3) the potential on the axis has only s dependence, therefore, only off axis particles will experience radial and azimuthal fields. Under the paraxial approximation of beam transport as stated above, only the second order terms in the expansions of the potential

will be important. Therefore, in our further analysis, we retain the terms only up to r^2 in Eq. (6.3) and ignore all other higher order terms in the potential. The potential then takes the form of

$$\Phi(r, \theta, s) = A(s) - A^{(2)}(s) \left(\frac{r}{2}\right)^2 + D(s) \left(\frac{r}{2}\right)^2 \cos(2\theta) \quad (6.4)$$

where $A(s) = \Phi(0, s)$ and $D(s) = 4\Phi_{2,2}(0, s)$. The first two terms in Eq. (6.4) are the usual terms used in the conventional solenoid. The third term is the contribution due to the asymmetric pole face of the elliptical solenoid. This term is similar to a quadrupolar term and produces focusing and defocusing in the two transverse planes in addition to the usual solenoidal focusing given by the first two terms. In terms of coordinates x, y and s , the potential Φ as given in Eq. (6.4), can be expressed as

$$\Phi(x, y, s) = A(s) - \frac{1}{4}(A^{(2)}(s) - D(s))x^2 - \frac{1}{4}(A^{(2)}(s) + D(s))y^2 \quad (6.5)$$

The components of the magnetic field at any point (x, y, s) near the axis can be obtained easily from Eq. (6.5) as

$$B_x(x, y, s) = -\frac{1}{2}(B^{(1)}(s) - D(s))x \quad (6.6a)$$

$$B_y(x, y, s) = -\frac{1}{2}(B^{(1)}(s) + D(s))y \quad (6.6b)$$

$$B_s(x, y, s) = B(s) - \frac{1}{4}(B^{(2)}(s) - D^{(1)}(s))x^2 - \frac{1}{4}(B^{(2)}(s) + D^{(1)}(s))y^2 \approx B(s) \quad (6.6c)$$

where $B(s) = A^{(1)}(s)$ is the field on the axis of the solenoid. In the last equation (6.6c) we have neglected the second order terms in x and y . The function $D(s)$ is related with the field gradient along x and y directions and depends upon the shape of the elliptic cross-section of the solenoid. The value of $B^{(1)}(s)$ and elliptical parameter $D(s)$ can be easily obtained using Eqs. (6.6) as

$$B^{(1)}(s) = -\left(\frac{B_x(R_x)}{R_x} + \frac{B_y(R_y)}{R_y}\right) \quad (6.7a)$$

$$D(s) = \left(\frac{B_x(R_x)}{R_x} - \frac{B_y(R_y)}{R_y}\right) \quad (6.7b)$$

where R_x and R_y are the semi major and semi minor axes of the elliptic pole face of the solenoid and $B_x(R_x)$ and $B_y(R_y)$ are the magnetic fields at the tip of the pole face along x and y directions respectively. It is easy to see that for $R_x = R_y$, the value of $D(s)$ becomes zero and $B^{(1)}(s)$ reduces to the same value as that of a conventional solenoid.

6.2.2. Equations of motion

The transverse equations of motion of a particle of rest mass m and charge q in the external magnetic field of the elliptical solenoid and beam self fields can be written as

$$\begin{aligned} \gamma m \ddot{x} &= q[E_x^S + \dot{y}(B_s + B_s^S) - \dot{s}(B_y + B_y^S)] \\ \gamma m \ddot{y} &= q[E_y^S + \dot{s}(B_x + B_x^S) - \dot{x}(B_s + B_s^S)] \end{aligned} \quad (6.8)$$

Here γ is the usual relativistic parameter and \vec{E}^S and \vec{B}^S are the space charge electric and magnetic fields respectively. For an intense continuous beam with small transverse dimensions and slow axial variations ($\partial/\partial s \cong 0$), the s variation of the self scalar and vector potentials can be treated as negligibly small. Under these conditions, the self-electric and self-magnetic fields associated with an intense continuous beam of charged particles can be obtained from

$$\begin{aligned} \vec{E}^S(x, y, s) &= -\left(\frac{\partial}{\partial x} \hat{x} + \frac{\partial}{\partial y} \hat{y}\right) \phi^S(x, y, s), \\ \vec{B}^S(x, y, s) &= \left(\frac{\partial}{\partial y} \hat{x} - \frac{\partial}{\partial x} \hat{y}\right) A_s^S(x, y, s) \end{aligned} \quad (6.9)$$

where the scalar potential $\phi^s(x, y, s)$ for the self electric field obeys the Poisson equation,

$$\left(\frac{\partial^2}{\partial x^2} + \frac{\partial^2}{\partial y^2} \right) \phi^s(x, y, s) = -\frac{qn(x, y, s)}{\epsilon_0} \quad (6.10)$$

and the vector potential for the self magnetic field is

$$\vec{A}^s(x, y, s) = \frac{\beta}{c} \phi^s(x, y, s) \hat{z} \quad (6.11)$$

Here $n(x, y, s)$ is the number density of particles.

In an uncoupled system, a beam having constant density and pulsating in transverse dimensions X and Y , the elliptical cross-section of the beam always remains upright. In this case one can obtain the space charge potential inside the beam by solving Eq. (6.10) and hence self fields as discussed in ref. [93] as well as in many text books [44, 84].

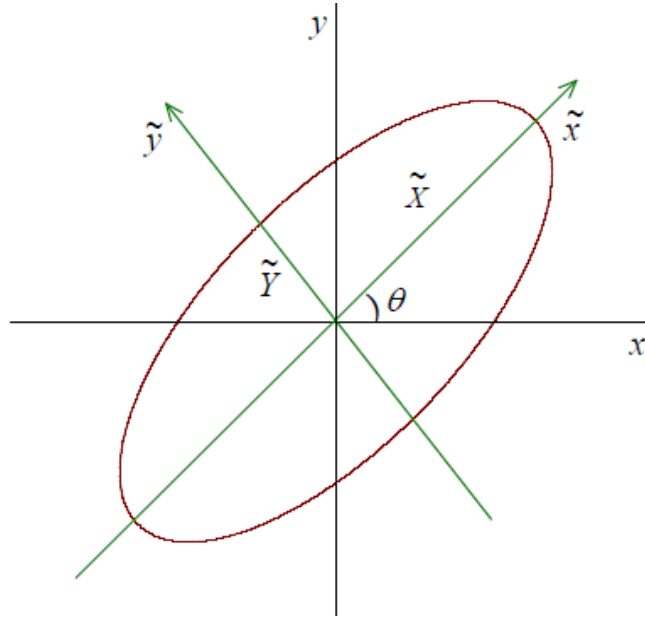


Fig. 6.1. A schematic of rotated coordinate system (\tilde{x}, \tilde{y}) with respect to the laboratory coordinate system (x, y) by an angle θ , in which the semi axes of elliptical cross-section of the beam are aligned with the coordinate axes.

In the cases where the two transverse motions are coupled, the elliptical cross section of the beam not only pulsates in two transverse planes but also rotates about the propagation axis. Both the dimensions X and Y as well as the tilt angle θ are functions of

s and thus it is not straight forward to obtain the space charge potential within the beam. In order to obtain the space charge potential in a coupled system at any axial location s we use a coordinate system which is rotated by an angle θ with respect to the laboratory coordinate system where the elliptical cross-section is upright. Here one can calculate the space charge potential assuming a uniform beam distribution. This potential can then be transformed to the laboratory coordinate system to calculate the required self-electric and self-magnetic fields as desired in the equations of motion.

We have introduced a coordinate system (\tilde{x}, \tilde{y}) which is rotated with respect to the laboratory coordinate system (x, y) by an angle θ . From here and onwards we use tilde \sim on a variable to represent the quantity in rotated coordinate system. In the rotated coordinate system the semi axes of elliptical cross-section of the beam are aligned with the coordinate axes as shown in [Fig. 6.1](#). The coordinates are related by

$$\tilde{x} = x \cos \theta + y \sin \theta, \quad \tilde{y} = -x \sin \theta + y \cos \theta \quad (6.12)$$

To determine the self-electric and self-magnetic fields of the beam self consistently we assume that the equilibrium particle density is uniform within the upright elliptical boundary in the rotated system and zero elsewhere. Therefore the uniform particle density profile of the beam in this system can be expressed as

$$n(\tilde{x}, \tilde{y}, s) = \frac{n_0}{\pi \tilde{X} \tilde{Y}} \Theta \left(1 - \frac{\tilde{x}^2}{\tilde{X}^2} - \frac{\tilde{y}^2}{\tilde{Y}^2} \right) \quad (6.13)$$

where $\Theta(x) = 1$ if $x > 0$ and $\Theta(x) = 0$ if $x < 0$ and $\tilde{X}(s) = 2\sqrt{\langle \tilde{x}^2 \rangle}$ and $\tilde{Y}(s) = 2\sqrt{\langle \tilde{y}^2 \rangle}$ are the beam sizes along the transverse \tilde{x} and \tilde{y} coordinate axes respectively.

Here $n_0 = \int_0^\infty d\tilde{x} d\tilde{y} n(\tilde{x}, \tilde{y}, s) = \text{const}$ is the number of particles per unit axial length. The density profile $n(x, y, s)$ in Eq. (6.10) will also remain constant inside the rotated ellipse whose transverse dimensions are X and Y and the tilt angle is θ [\[95-97\]](#). The self

electrostatic potential in the rotated coordinate system where elliptical cross-section is upright with constant density distribution specified in Eq. (6.13) can be solved using Poisson's equation [98]. The result is

$$\phi^S(\tilde{x}, \tilde{y}, s) = -\frac{I}{2\pi\epsilon_0\beta c} \frac{1}{(\tilde{X} + \tilde{Y})} \left(\frac{\tilde{x}^2}{\tilde{X}} + \frac{\tilde{y}^2}{\tilde{Y}} \right) \quad (6.14)$$

where $I = qn_0\pi\tilde{X}\tilde{Y}\beta c$ is the beam current and ϵ_0 is the permittivity of free space. By substituting the expression of \tilde{x} and \tilde{y} from Eq. (6.12) into Eq. (6.14), we have

$$\phi^S(x, y, s) = -\frac{I}{4\pi\epsilon_0\beta c} (\phi_{xx}x^2 - 2\phi_{xy}xy + \phi_{yy}y^2) \quad (6.15)$$

where

$$\begin{aligned} \phi_{xx} &= \frac{\tilde{X} + \tilde{Y} - (\tilde{X} - \tilde{Y})\cos 2\theta}{\tilde{X}\tilde{Y}(\tilde{X} + \tilde{Y})}, & \phi_{xy} &= \frac{(\tilde{X} - \tilde{Y})\sin 2\theta}{\tilde{X}\tilde{Y}(\tilde{X} + \tilde{Y})}, \\ \phi_{yy} &= \frac{\tilde{X} + \tilde{Y} + (\tilde{X} - \tilde{Y})\cos 2\theta}{\tilde{X}\tilde{Y}(\tilde{X} + \tilde{Y})} \end{aligned} \quad (6.16)$$

Eq. (6.15) gives the self potential in terms of laboratory coordinates x and y . The expressions for the self field of a rotated beam in the case of a linearly coupled system are also mentioned in ref. [99, 100].

We are now in a position to express the equations of motion given in Eq. (6.8) in terms of field components of elliptical solenoid obtained in Eq. (6.6) and self field of the beam.

Replacing t with s ($s = \beta ct$) and using the fact that $E_x^S - \dot{s}B_y^S = -(1 - \beta^2)\partial\phi^S/\partial x$,

$E_y^S + \dot{s}B_x^S = -(1 - \beta^2)\partial\phi^S/\partial y$ and $B_s^S = 0$, the equations of motion can be written as

$$\begin{aligned} x'' &= \frac{qB'(s)}{2m\gamma\beta c} y + J(s)y + 2K(s)y' + Q(x\phi_{xx} - y\phi_{xy}) \\ y'' &= -\frac{qB'(s)}{2m\gamma\beta c} x + J(s)x - 2K(s)x' + Q(y\phi_{yy} - x\phi_{xy}) \end{aligned} \quad (6.17)$$

where $K(s) = qB(s)/2m\gamma\beta c$, $J(s) = qD(s)/2m\gamma\beta c$ and $Q = qI/2\pi\epsilon_0 mc^3\beta^3\gamma^3$ is the beam perveance and the prime denotes the derivative with respect to s . The first term in Eqs (6.17) depends upon the gradient of the magnetic field. It is effective only at the entrance and exit of the elliptical solenoid where there is a sharp rise and fall in the magnetic field. Its effect is to impart an impulse to the particle which causes a sudden change in the direction of the trajectory [91, 101] and can be expressed in matrix form for the entrance as

$$\begin{bmatrix} x \\ x' \\ y \\ y' \end{bmatrix} = \begin{bmatrix} 1 & 0 & 0 & 0 \\ 0 & 1 & K(s) & 0 \\ 0 & 0 & 1 & 0 \\ -K(s) & 0 & 0 & 1 \end{bmatrix} \begin{bmatrix} x_0 \\ x'_0 \\ y_0 \\ y'_0 \end{bmatrix} = \mathbf{R}_{end}(K(s)) \begin{bmatrix} x_0 \\ x'_0 \\ y_0 \\ y'_0 \end{bmatrix} \quad (6.18)$$

where x_0, y_0 are the initial positions and x'_0, y'_0 are the initial divergences of the particle in x and y planes respectively at the entrance of the magnet. For the exit of the solenoid the matrix will be $\mathbf{R}_{end}(-K(s))$. Inside the elliptical solenoid the particle trajectory is obtained by solving Eqs (6.17) without the first term. Thus the equations of motion inside the elliptical solenoid are

$$\begin{aligned} x'' &= J(s)y + 2K(s)y' + Q(x\phi_{xx} - y\phi_{xy}) \\ y'' &= J(s)x - 2K(s)x' + Q(y\phi_{yy} - x\phi_{xy}) \end{aligned} \quad (6.19)$$

These are coupled differential equations and their analytical solutions are known in the absence of space charge ($Q = 0$) and can be represented in terms of transfer matrix [91].

The transfer matrix then can be utilized to obtain the beam properties using the standard sigma matrix method. However, in the case of space charge effect simple matrix multiplication cannot be used because the space charge forces are dependent on the properties of the beam itself. A convenient way for dealing with the space charge is to employ the infinitesimal transfer matrix approach.

6.2.3. Infinitesimal transfer matrix and beam envelopes

Since Eqs. (6.19) are linear, therefore any solution of these equations can be represented by a linear combinations of four linearly independent solutions. Since we are primarily interested in the transverse beam dynamics we need to construct 4×4 infinitesimal transfer matrix. Let $\mathbf{x}(s_0) = (x, x', y, y')^T$ represents the coordinates of a paraxial ray in the laboratory coordinate system at a location s_0 inside the elliptical solenoid magnet. At some other location s , the coordinates will be transformed according to the matrix equation, $\mathbf{x}(s) = \mathbf{R}(s, s_0)\mathbf{x}(s_0)$ where $\mathbf{R}(s, s_0)$ is a 4×4 transfer matrix inside the magnet whose elements are functions of s and s_0 . In order to generate the matrix $\mathbf{R}(s, s_0)$, we need to solve Eqs. (6.19) for four different initial conditions with sufficiently small interval $ds = s - s_0$, with $ds \ll L$, where L is the length of the elliptical solenoid. A simple way is to choose the initial conditions in which one coordinate say x is equal to 1 and all other coordinates are equal to 0. The solution of differential equations will yield the first column of transfer matrix $\mathbf{R}(s, s_0)$. By repeating the same procedure with other coordinates one can easily get the all other columns of matrix $\mathbf{R}(s, s_0)$. The entry and exit matrix of magnet at s_0 and s has to be multiplied with $\mathbf{R}(s, s_0)$ to get the coordinate transformation through the small portion ds of elliptical solenoid magnet. This can be expressed as

$$\mathbf{M}(s, s_0) = \mathbf{R}_{end}(-K(s))\mathbf{R}(s, s_0)\mathbf{R}_{end}(K(s_0)) \quad (6.20)$$

This is the infinitesimal transfer matrix.

It is to be noted here that the space charge term in equations of motion (6.19) depends on the properties of the beam itself i.e. on the beam sizes ($\tilde{X}(s)$ and $\tilde{Y}(s)$) and the rotation angle θ which are function of the axial distance s . These quantities must be evaluated

after each interval ds to obtain the self field. The beam envelope quantities are basically related to the beam matrix σ . For a continuous beam the sigma matrix defines the shape of a 4D hyper-ellipsoid of the beam i.e.

$$\mathbf{x}^T \sigma^{-1} \mathbf{x} = 1 \quad (6.21)$$

where the superscript “ T ” denotes the transpose of the matrix. The 4D hyper-ellipsoid when projected into 2D subspace (say x, y) in the laboratory coordinate system, the equation of the projected ellipse becomes

$$\mathbf{x}_{13}^T \sigma_{13}^{-1} \mathbf{x}_{13} = 1 \quad (6.22)$$

where

$$\mathbf{x}_{13} = \begin{bmatrix} x \\ y \end{bmatrix}, \quad \sigma_{13} = \begin{bmatrix} \sigma_{xx} & \sigma_{xy} \\ \sigma_{xy} & \sigma_{yy} \end{bmatrix} \quad (6.23)$$

Here the elements of sub-matrix σ_{13} are chosen from elements of the matrix σ defined in Eq. (6.21). Expanding Eq. (6.22) we have

$$\sigma_{xx}\sigma_{yy} - \sigma_{xy}^2 = \sigma_{yy}x^2 + \sigma_{xx}y^2 - 2\sigma_{xy}xy \quad (6.24)$$

In the rotated coordinate system, the beam ellipse with semi axes $\tilde{X}(s)$ and $\tilde{Y}(s)$ as shown in [Fig. 6.1](#) is an upright ellipse and its equation can be written as

$$\frac{\tilde{x}^2}{\tilde{X}^2} + \frac{\tilde{y}^2}{\tilde{Y}^2} = 1 \quad (6.25)$$

Now using the values of \tilde{x} and \tilde{y} from Eq. (6.12) into Eq. (6.25) and then comparing the coefficients of x^2 , y^2 and xy with Eq. (6.24) we have

$$\sigma_{xx} = \tilde{X}^2 \cos^2 \theta + \tilde{Y}^2 \sin^2 \theta \quad (6.26a)$$

$$\sigma_{yy} = \tilde{Y}^2 \cos^2 \theta + \tilde{X}^2 \sin^2 \theta, \quad (6.26b)$$

$$\sigma_{xy} = (\tilde{X}^2 - \tilde{Y}^2) \sin \theta \cos \theta \quad (6.26c)$$

The semi axes of upright ellipse $\tilde{X}(s)$ and $\tilde{Y}(s)$ in the rotated coordinate system can be easily obtained using Eqs. (6.26) as

$$\begin{aligned}\tilde{X}(s) &= \frac{1}{\sqrt{2}} \sqrt{\sigma_{xx}(s) + \sigma_{yy}(s) + \sqrt{[\sigma_{xx}(s) - \sigma_{yy}(s)]^2 + 4\sigma_{xy}^2(s)}} \\ \tilde{Y}(s) &= \frac{1}{\sqrt{2}} \sqrt{\sigma_{xx}(s) + \sigma_{yy}(s) - \sqrt{[\sigma_{xx}(s) - \sigma_{yy}(s)]^2 + 4\sigma_{xy}^2(s)}} \\ \theta(s) &= \frac{1}{2} \tan^{-1} \left(\frac{2\sigma_{xy}(s)}{\sigma_{xx}(s) - \sigma_{yy}(s)} \right)\end{aligned}\quad (6.27)$$

The beam sizes $\tilde{X}(s)$ and $\tilde{Y}(s)$ and the rotation angle $\theta(s)$ have been used to determine the self field potential in the laboratory frame as given in Eq. (6.15) to solve Eqs. (6.19).

In order to determine the beam sigma matrix along the axial distance s in the laboratory coordinate system, we use the recursive sigma matrix method. In this method we divided the elliptical solenoid magnet into large number of small intervals $ds = s - s_0$ and beam matrix $\sigma(s)$ at location s is obtained by using the relation

$$\sigma(s) = \mathbf{M}(s, s_0) \sigma(s_0) \mathbf{M}(s, s_0)^T \quad (6.28)$$

where $\sigma(s_0)$ is the beam matrix at location s_0 and $\mathbf{M}(s, s_0)$ is the infinitesimal transfer matrix defined in Eq. (6.20). The beam sizes and the emittances in the x and y planes at an axial location s can be obtained from the following relations

$$\begin{aligned}X(s) &= \sqrt{\sigma_{xx}(s)}, \quad Y(s) = \sqrt{\sigma_{yy}(s)} \\ \varepsilon_x(s) &= \sqrt{[\sigma_{xx}(s)\sigma_{x'x'}(s) - \sigma_{xx'}^2(s)]}, \quad \varepsilon_y(s) = \sqrt{[\sigma_{yy}(s)\sigma_{y'y'}(s) - \sigma_{yy'}^2(s)]}\end{aligned}\quad (6.29)$$

6.3. Beam optical properties of an elliptical solenoid

In this section we first discuss the beam optical properties of the elliptical solenoid magnet in the presence of space charge using the parameters of our low energy beam

transport line. We have chosen injection energy equal to 80 keV and parameters $K = 0.04 \text{ cm}^{-1}$ and $J = 0.0003 \text{ cm}^{-2}$. These parameters are taken constant along the length s of the magnet. Throughout the analysis we have assumed that initial emittances in both the planes are uncoupled. The beam line parameters are: length of the elliptic solenoid $L = 30 \text{ cm}$ and drift lengths before and after the magnet are 40 cm and 100 cm respectively.

6.3.1. Focusing characteristics

We have written a computer code which solves the paraxial trajectory given by Eqs. (6.19) for specified initial beam conditions from point s_0 to $s = s_0 + ds$, where ds is the small interval. We have used the step size $ds = 1 \text{ mm}$. Using the solution of paraxial ion trajectories for four different initial conditions, the infinitesimal transfer matrix $\mathbf{M}(s, s_0)$ is obtained for the small interval ds . It is then used to find out the beam matrix $\sigma(s)$ at point s from Eq. (6.28) utilizing the initial value of $\sigma(s_0)$. To determine the self field potential $\phi^S(x, y, s)$ in the optical coordinate system we have used the elements of $\sigma(s)$ in Eq. (6.27) to get the beam sizes $\tilde{X}(s)$, $\tilde{Y}(s)$ and the rotation angle $\theta(s)$. The beam envelope quantities are obtained from the elements of $\sigma(s)$ using Eqs. (6.29).

In Fig. 6.2 the behavior of beam envelope and focusing properties of elliptical solenoid magnet are compared with the conventional solenoid ($J = 0$) at two values of beam current $I = 0 \text{ mA}$ and $I = 10 \text{ mA}$. The input beam conditions for both cases are $X(0) = Y(0) = 0.25 \text{ cm}$, $X'(0) = Y'(0) = 0 \text{ mrad}$ and equal total emittances in both the planes i.e. $\varepsilon_x(0) = \varepsilon_y(0) = 60 \pi \text{ mm mrad}$ at 40 cm before the magnet. The variation of the beam envelopes through the solenoid magnet for beam current $I = 0 \text{ mA}$ and $I = 10 \text{ mA}$ are shown in Fig. 6.2(a). As expected, the beam envelopes in both the planes are similar for this circular symmetric input beam because solenoid magnet exerts equal focusing forces in both the planes. The effect of space charge is clearly evident in terms of

location and size of the waist. For 0 mA beam current, the waist with size ~ 0.2 cm is formed at a distance ~ 30 cm from the exit of the magnet. In the case of 10 mA, not only the size of the waist ~ 0.33 cm of the beam is larger but the location of the waist ~ 50 cm is also at a farther distance from the exit of the magnet. However, in both the cases the circular symmetry of the beam is maintained.

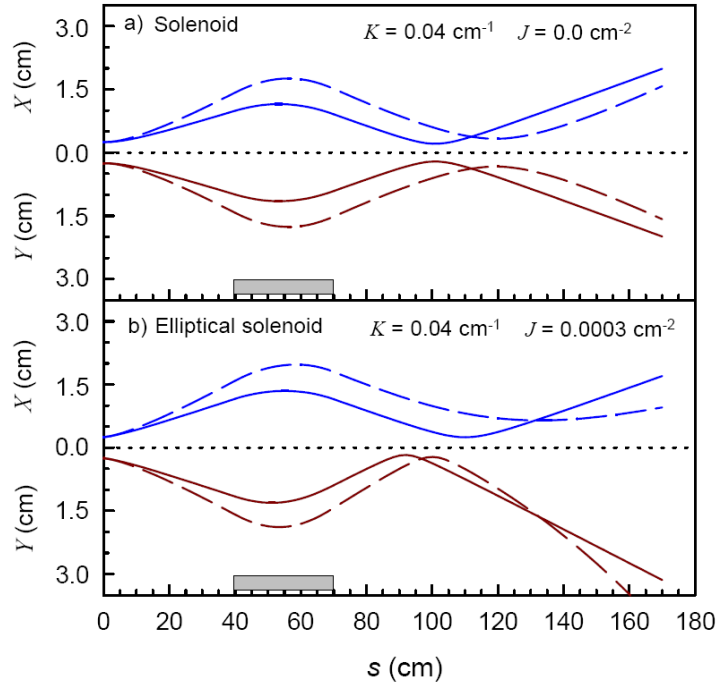


Fig. 6.2. Beam envelopes for (a) solenoid magnet and (b) elliptical solenoid magnet, for same initial axisymmetric beam with $X(0) = Y(0) = 0.25$ cm, $X'(0) = Y'(0) = 0$ mrad and $\varepsilon_x(0) = \varepsilon_y(0) = 60 \pi$ mm mrad for two different values of beam current $I = 0$ mA (solid curve) and $I = 10$ mA (dashed curve).

In **Fig 6.2(b)** we have shown the evolution of beam envelopes through the elliptical solenoid with parameters $K = 0.04 \text{ cm}^{-1}$ and $J = 0.0003 \text{ cm}^{-2}$ for two values of beam current with the same input conditions as in the previous case. The effect of asymmetric focusing and inter-plane coupling effect is clearly visible from the envelope behavior. The beam envelopes in both the planes for $I = 0$ mA are different because of the parameter J which causes an extra gain in focusing force in y plane and a reduction in the x plane. As a result the beam waist in y plane is formed at a shorter distance compared to that of the

x -plane and the sizes of the beam waist are also different for the symmetric input beam. The effect of space charge, as shown in Fig 6.2(b) by dashed curve for 10 mA beam current, not only increases the waist sizes but also the location of the waists in both planes.

6.3.2. Study of inter-plane coupling effect

In order to understand the coupling effect in the beam caused by an elliptical solenoid magnet we now explore the magnitude of projected emittances under various input beam conditions. Fig. 6.3 shows the behavior of the projected x and y emittances as a function of axial distance s , for an axisymmetric input beams with $X(0) = Y(0) = 0.25$ cm, $X'(0) = Y'(0) = 0$ mrad and with equal emittances $\varepsilon_x(0) = \varepsilon_y(0) = 60 \pi$ mm mrad in both the planes. In the case of a conventional solenoid ($J = 0$) the projected emittances in the x and y planes are same at all the points downstream, they are equal to the initial emittances and are not affected by the beam current. This is due to the fact that both the external as well as space charge forces are symmetric with respect to the two semi-axes of the ellipse in the local $x - y$ plane.

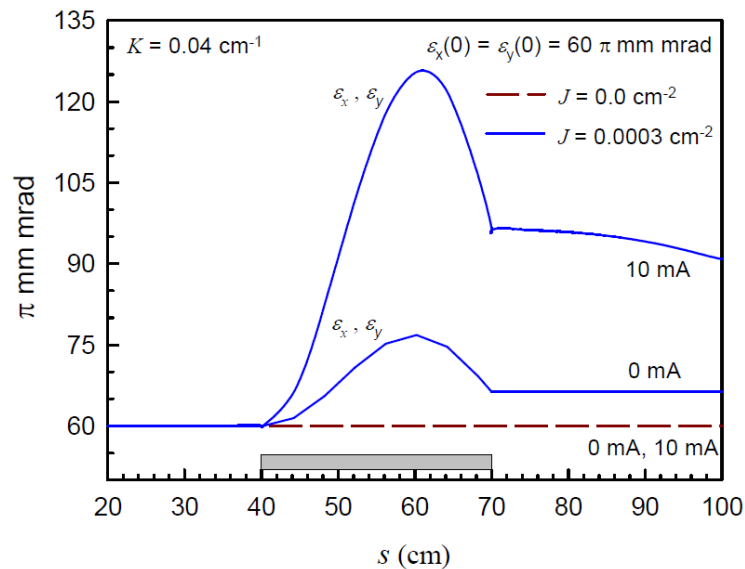


Fig. 6.3. Transverse projected x and y emittances through the solenoid (dashed line) and elliptical solenoid (solid line) for axisymmetric input beam. The input conditions of the beam are same as in the case of Fig. 6.2.

The situation is completely different in the case of elliptical solenoid ($J = 0.0003 \text{ cm}^{-2}$) where we see a growth in the projected x and y emittances even for $I = 0$ mA. This happens because of the fact that the initial axisymmetric beam becomes non-axisymmetric in the local x - y plane even in the absence of space charge. The magnitude of the projected emittances in both the planes grows rapidly as the beam passes through the magnet, reaches to a maximum value inside the magnet and then decreases for both values of beam current. It is interesting to note that x and y projected emittances are always equal to each other at any point downstream and independent of the magnitude of the x - y coupling. There is a substantial growth in the magnitude of the projected emittances at the exit in both the planes due to the coupling effects. The estimated values of the emittances for $I = 0$ mA and $I = 10$ mA at the exit of the elliptical solenoid magnet are 66.4π mm mrad and 96.4π mm mrad respectively.

It can be readily seen from Fig. 6.3 that the behavior of projected emittances in the drift after the exit of the elliptical solenoid is different for the case of beam with space charge where the emittances do not remain constant as in the case of $I = 0$ mA. This is happening due to the coupled motions in x - y planes at the exit of elliptical solenoid i.e. the tilted transverse cross-section of the beam. The space charge effect further introduces coupling due to which there will be either a growth or reduction in the projected emittances as the beam travels in the drift space after the exit.

In Fig. 6.4 we have plotted the behavior of transverse projected emittances through the elliptical solenoid and compared the results with that of conventional solenoid. We have chosen the initial emittances in x and y planes as $\varepsilon_x(0) = 70 \pi$ mm mrad, $\varepsilon_y(0) = 50 \pi$ mm mrad respectively and unequal input beam sizes in the two transverse directions i.e. $X(0) = 0.5$ cm, $Y(0) = 0.25$ cm. The behavior of projected emittances for a conventional solenoid ($J = 0$) is shown in Fig. 6.4(a). It is interesting to note here that there is an

exchange of emittance from one plane to the other plane. The projected emittance reduces in the plane where the initial emittance is high and it grows in the other plane where the initial emittance is low. The projected x and y emittances at any point downstream are always unequal except at a point as shown by the dotted vertical line where these are equal in both the planes. There is very little growth in the projected emittances due to the space charge effect for the present initial condition of the beam.

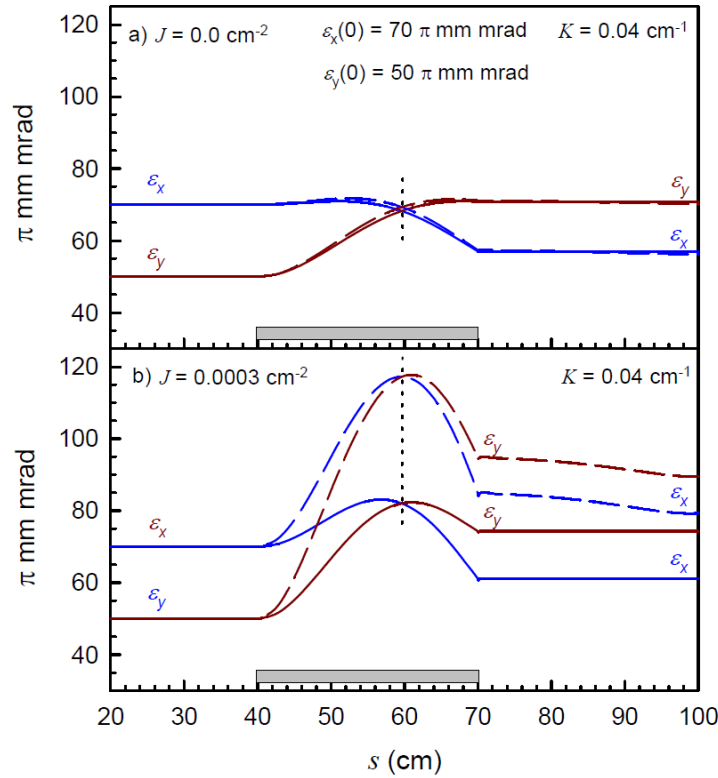


Fig. 6.4. Projected x and y emittances for $I = 0$ mA (solid line) and $I = 10$ mA (dashed line) through the (a) solenoid and (b) elliptical solenoid magnet for non-axisymmetric input beam. The input beam conditions in both cases are $X(0) = 0.5$ cm, $Y(0) = 0.25$ cm, $X'(0) = Y'(0) = 0$ mrad, $\varepsilon_x(0) = 70 \pi$ mm mrad and $\varepsilon_y(0) = 50 \pi$ mm mrad.

The behavior of projected emittances through the elliptical solenoid is presented in [Fig 6.4\(b\)](#) with the same initial conditions. Apart from an exchange of emittances from one plane to the other plane, there is a substantial growth in the projected emittances inside as well as outside the magnet due to the space charge effect. Two points are noteworthy from [Fig. 6.4\(b\)](#). In the case of 10 mA beam current, the projected emittance in both the planes

rises very fast inside the magnet, goes to a peak value and then drops to a smaller value at the exit. This effect is very small in the case of low beam current as well as in the case of the conventional solenoid. The second interesting point is that the projected emittances in both the planes are also equal at only one point and the location of that point is unaffected by the space charge effect.

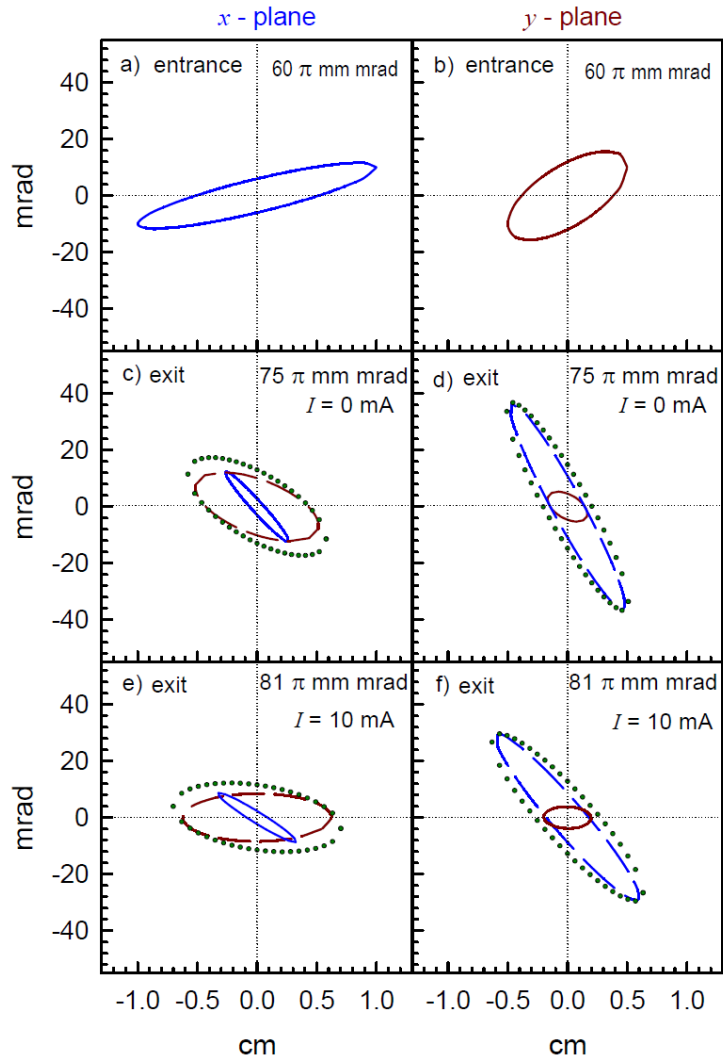


Fig. 6.5. Phase ellipses in x and y planes at the exit of elliptical solenoid along with contributions from the inter-plane coupling for initial uncoupled phase ellipses. Parameters of elliptical solenoid are $K = 0.04 \text{ cm}^{-1}$, $J = 0.0003 \text{ cm}^{-2}$ and $L = 30 \text{ cm}$.

In an elliptical solenoid, there is a strong coupling between the two transverse planes which results in growth of projected emittances at the exit. This growth in projected emittances depends on the parameter J and is very sensitive to the orientation of the

phase ellipses of the beam at the entrance of the elliptical solenoid. In order to demonstrate the coupling effect of the two transverse planes on the projected emittances, tracing of paraxial rays of 40 representative particles that belong to the boundary of the contours in $(x - x')$ and $(y - y')$ planes of the phase ellipse at the entrance in both the planes have been performed through the magnet. The initial conditions for the coordinates and the beam divergences are chosen using tilted phase ellipses with cross-section $X(0) = 1$ cm, $Y(0) = 0.5$ cm and emittances $\varepsilon_x(0) = \varepsilon_y(0) = 60 \pi$ mm mrad in both planes.

Fig. 6.5 shows the orientations of phase ellipses, at the entrance and exit of the elliptical solenoid for 0 mA and 10 mA along with the contributions from the inter-plane coupling. **Figures 6.5(a)** and **6.5(b)** represent the initial phase ellipses at the entrance of the elliptical solenoid whereas **Fig. 6.5(c)** and **6.5(d)** represent the phase ellipses at the exit for $I = 0$ mA. Solid lines indicate the area pertaining to the particular phase plane whereas dashed lines indicate the area contributed from the other plane. The total area of these subspaces gives the effective emittance at the exit of the magnet as shown by the dotted curve. The inter-plane coupling effects in the case of 10 mA beam current are shown in **Fig. 6.5(e)** and **6.5(f)**. It is to be noted here that the increase in emittances in both the planes at $I = 0$ mA is purely due to the inter-plane coupling effects. The estimated effective emittances at the exit in x and y planes are same and equal to 75π mm mrad for $I = 0$ mA and 81π mm mrad for $I = 10$ mA. However, the orientations of projected emittances in both the planes at the exit are different.

6.3.3. Parametric dependence of emittance growth

We have also studied the behavior of projected emittances in both the planes at the exit with parameter J for three different values of the beam current. We have considered two cases. In the first case (**Fig. 6.6(a)**) we have chosen an axisymmetric beam with

$X(0) = Y(0) = 1.5$ cm whereas in the second case (Fig. 6.6(b)) it is a non-axisymmetric beam with $X(0) = 1.5$ cm, $Y(0) = 1.0$ cm. In both the cases initial emittances are uncoupled and equal i.e. $\varepsilon_x(0) = \varepsilon_y(0) = 60 \pi$ mm mrad. It can be readily seen from Fig. 6.6 that, although the projected emittances at the exit increase with parameter J and beam current, their values are always equal in both the planes. For $J = 0$, the projected emittances at the exit are equal to the initial emittances in the case of axisymmetric beam. However, there is a substantial growth in the emittances in the case of non-axisymmetric beam even at $J = 0$ and increases with beam current. It is observed from the numerical calculations that there is a comparatively more growth in the projected emittances for non-axisymmetric beam as we increase the value of parameter J and the beam current.

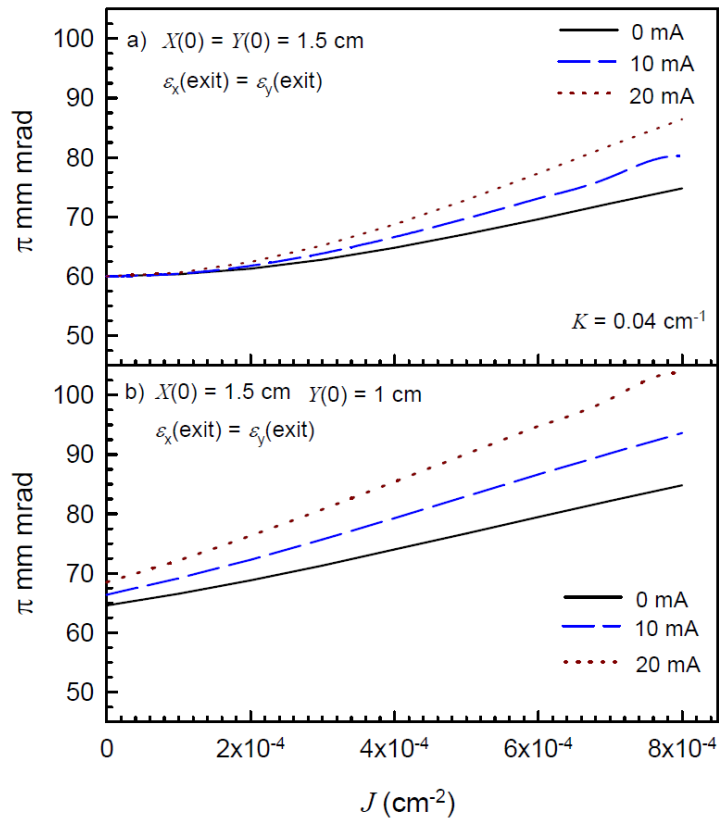


Fig. 6.6. Transverse projected emittances at the exit of the elliptical solenoid as a function of the parameter J for three different values of beam current. (a) axisymmetric beam with $X(0) = Y(0) = 1.5$ cm. (b) non-axisymmetric beam with $X(0) = 1.5$ cm, $Y(0) = 1.0$. Other input conditions are, $\varepsilon_x(0) = \varepsilon_y(0) = 60 \pi$ mm mrad and $X'(0) = Y'(0) = 10$ mrad. Parameters of the elliptical solenoid are $k = 0.04 \text{ cm}^{-1}$ and $L = 30$ cm.

In Fig. 6.7 we have plotted the transverse projected emittances at the exit of the elliptical solenoid as a function of the parameter J for three different values of the beam current considering a more general case where the initial emittances are unequal in both the planes i.e. $\varepsilon_x(0) = 70 \pi$ mm mrad, $\varepsilon_y(0) = 50 \pi$ mm mrad and the beam is non-axisymmetric. As usual we observe an increase in the projected emittances with beam current as well as with parameter J . In this case also there is a distinct exchange of emittances from one plane to the other plane at the exit of the magnet.

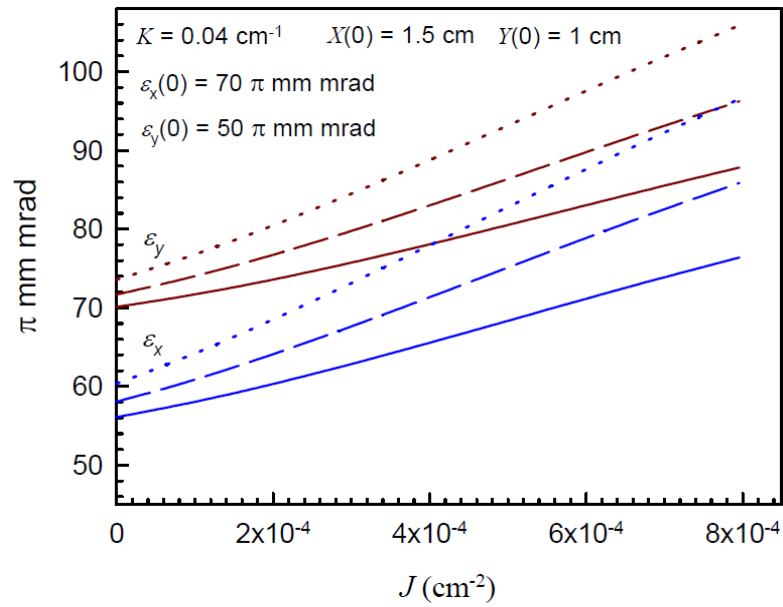


Fig 6.7. Projected emittances at the exit of the elliptical solenoid as a function of the parameter J for beam currents $I = 0$ mA (solid line), $I = 10$ mA (dashed line) and $I = 20$ mA (dotted line) for an initial non-axisymmetric beam with $X(0) = 1.5$ cm, $Y(0) = 1$ cm, $X'(0) = Y'(0) = 10$ mrad, $\varepsilon_x(0) = 70 \pi$ mm mrad and $\varepsilon_y(0) = 50 \pi$ mm mrad. Parameters of the elliptical solenoid are $K = 0.04 \text{ cm}^{-1}$ and $L = 30$ cm.

6.3.4. Conversion of an elliptical beam to a circular beam

It is not always possible to transfer a beam of elliptical cross-section to a circular cross-section using a conventional solenoid. Such transformation can happen only in a particular situation where the beam rotation through the solenoid is $(2n+1)\pi/4$ [102, 103]. But a beam of circular cross-section can never be transformed to an elliptical cross-

section using an axisymmetric solenoid magnet. However an elliptical solenoid can transform a beam of elliptical cross-section to a circular cross-section and vice-versa.

A single elliptical solenoid, in general can never transform a beam of circular cross-section to a circular cross-section like an axisymmetric solenoid. For this we need a combination of two elliptical solenoids in succession with parameters J and $-J$. Figure 6.8 shows the beam envelopes in which the beam waists with equal sizes are formed at the axial location ~ 105 cm in both the planes for $I = 10$ mA. The initial beam is axisymmetric with $X(0) = Y(0) = 0.25$ cm, $X'(0) = Y'(0) = 0$ mrad and $\varepsilon_x(0) = \varepsilon_y(0) = 60\pi$ mm mrad. The optimum locations and lengths of the elliptical solenoids are indicated by boxes in Fig. 6.8. The length of the first magnet is 20 cm with $K = 0.046$ cm $^{-1}$ and $J = 0.00025$ cm $^{-2}$ and that of the second is 19 cm with $K = 0.046$ cm $^{-1}$, $J = -0.00025$ cm $^{-2}$.

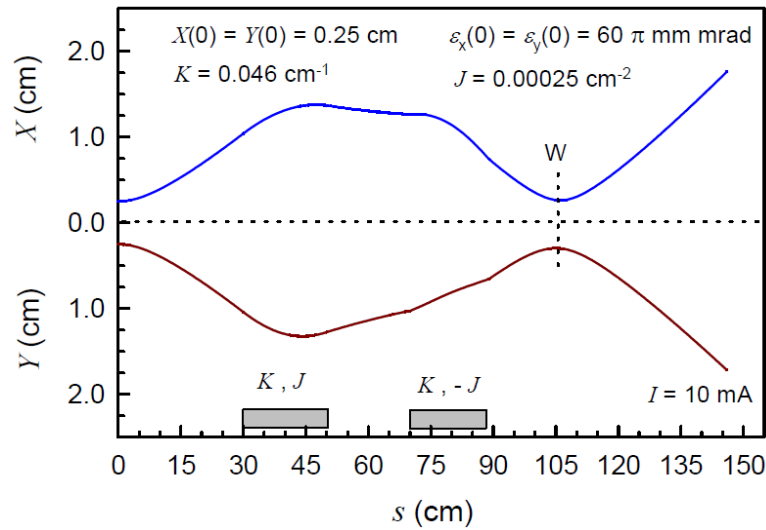


Fig. 6.8. Beam envelopes in x and y planes for 10 mA beam current through elliptical solenoid doublet to produce beam waists at the axial location ~ 105 cm. The initial beam is axisymmetric with $X(0) = Y(0) = 0.25$ cm and $\varepsilon_x(0) = \varepsilon_y(0) = 60\pi$ mm mrad. Here “W” indicates the location of equal beam waist in both the planes.

6.4. Transverse beam matching to the spiral inflector

As it is mentioned earlier, the injection system of 10 MeV proton cyclotron consists of two solenoid magnets to transport and match the beam at the entrance of a spiral inflector.

A detailed study presented in Chapter 4 indicates that convergent phase ellipses with different orientations in x and y planes and a comparatively smaller width in y plane give better beam transmission. Figure 6.9 shows the results of transverse matching of an axisymmetric beam at the entrance of the spiral inflector. The resulting beam envelopes producing a beam of unequal sizes in x and y planes are shown in Fig. 6.9(a) and the phase

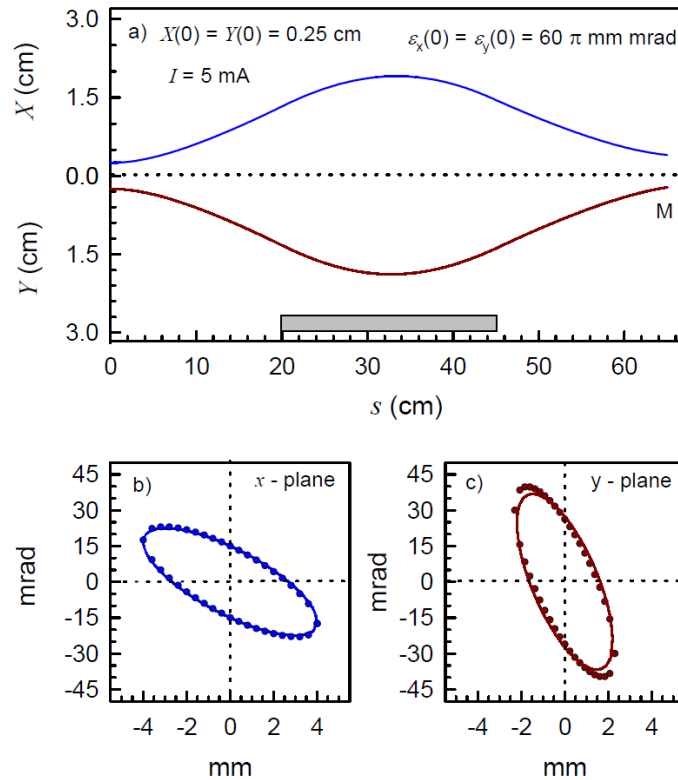


Fig. 6.9. Beam envelopes and phase ellipses in the x and y planes for matching at the inflector entrance with average beam current $I = 5$ mA. The input beam parameters are $X(0) = Y(0) = 0.25$ cm, $\varepsilon_x(0) = \varepsilon_y(0) = 60 \pi$ mm mrad. The estimated emittances at the matching point M are $\varepsilon_x(M) = \varepsilon_y(M) = 61.4 \pi$ mm mrad.

ellipses are shown by solid lines in Fig. 6.9(b) and 6.9(c). The required phase ellipses at the entrance of the spiral inflector for better transmission and minimum emittance growth are shown by dotted curves in Fig. 6.9(b) and 6.9(c). The initial beam parameters at the waist position ($s = 0$) of second solenoid are $X(0) = Y(0) = 0.25$ and equal values of emittances $\varepsilon_x(0) = \varepsilon_y(0) = 60 \pi$ mm mrad in both the planes. The optimized parameters

of the elliptical solenoid magnet are $K = 0.064 \text{ cm}^{-1}$ and $J = 0.00014 \text{ cm}^{-2}$ and length $L = 25 \text{ cm}$. The location of elliptical solenoid and matching point from the beam waist of the second solenoid are 20 cm and 65 cm respectively. The estimated projected emittances at the matching point are $\varepsilon_x(M) = \varepsilon_y(M) = 61.4 \pi \text{ mm mrad}$ which indicates very small emittance growth caused due to elliptical solenoid.

6.5. Summary

In this Chapter, we have discussed the focusing properties of an elliptical solenoid and studied the transport and matching of space charge dominated beam using the infinitesimal transfer matrix technique. We have studied the emittance growth that results from the coupling between the two transverse planes as a function of beam current and the coupling parameter of the elliptical solenoid under various input beam conditions. The change of transverse projected emittances as a function of distance does not really indicate any degradation in the beam quality. We like to mention here that in a linearly coupled 4D phase space although the x and y projected emittances vary as a function of distance, there are always two independent generalized invariants analogous to the x and y emittances for the uncoupled system [104, 105]. Any increase in the generalized invariants provides information about the intrinsic degradation of the full 4D phase space of the beam. Thus in order to know the presence of any nonlinearity in the system one needs to calculate these invariants. We have also shown that the elliptical solenoid has an advantage and flexibility over the conventional solenoid for transverse matching of the beam to the spiral inflector which requires unequal beam sizes as well as different orientations of phase ellipses in the two transverse planes.

Chapter 7

Conclusions and future works

7.1. Conclusions

In this thesis two major topics related with the injection and acceleration of a space charge dominated beam in a compact cyclotron have been addressed. The first topic deals with the design of the 10 MeV compact proton cyclotron and the study of the behaviour of space dominated beam along the accelerated orbits. Initially, a hard-edge approximation for field and the transfer matrix technique have been used to determine the preliminary design parameters of the magnet. We have studied the behaviour of beam envelopes using a uniform beam distribution during the first turn to estimate the acceptance in the central region. The limiting current that can be accommodated for further acceleration has also been estimated. Our results suggest that there is a particular set of initial parameters for a given beam current that gives the optimum beam envelopes. It is shown that a beam with low emittance $\sim 0.8 \pi$ mm mrad and injection energy in the range of 80-100 keV appears reasonable for the injection of 10 mA beam current (theoretical limiting value ~ 15 mA) in the compact cyclotron.

In the next step an iterative random search technique has been developed and utilized to optimize the final profile of the magnet of the 10 MeV cyclotron. When compared with other methods, it is found that this method gives smooth shape of the hill profile and takes less computation time for optimization. The present design of the magnet provides axial betatron tune greater than 0.5 throughout, except near the central region and the phase excursion in the entire region is limited within ± 2 deg.

Since hard edge model of the magnetic field overestimates the vertical betatron tunes at lower radii, the results of envelopes prediction in the cyclotron so obtained are limited in accuracy. In order to improve the accuracy and study the beam dynamics in detail we have used the computed 3D magnetic field data and coupled accelerated beam envelope equations developed assuming the beam as a uniform ellipsoidal bunch. The study of envelope behaviour at a particular radius indicates that when the initial beam sizes are displaced from the matched sizes, the number of oscillations follows the pattern as per the prediction of the linear theory of envelope oscillations.

The results of studies on behaviour of the beam envelope along the accelerated orbits predict the maximum transverse limiting current 7 mA for ellipsoidal bunch and 8.2 mA for uniform continuous beam model within 6 mm half aperture. It is found that the limiting current reduces slightly with increase in the beam emittance. The results of beam optimization in the focusing channel of the cyclotron indicate that for maximum beam transmission one needs converging initial phase ellipses in both the planes. However in reality it is difficult to get such initial conditions because a spiral inflector generally produces axially diverging phase ellipse at its exit. The estimated value of limiting current using the input conditions provided by the spiral inflector is found to reduce slightly ($I_{lim} = 5.3$ mA) within the specified 6 mm half aperture.

The second topic that has been addressed in this thesis is the detailed design of the spiral inflector, the dynamics of a space charge dominated beam through it and the transverse beam matching at its input. A tilted spiral inflector with height $A = 8.65$ cm and tilt parameter $k' = 0.65$ has been chosen after performing several iterations. During the design of the inflector in the space available in the central region at the chosen injection energy we have taken care that the inflected beam in the median plane is well centered.

A detailed study of beam dynamics through the spiral inflector using a uniform ellipsoidal bunch, and including the effect of space charge, has been carried out using infinitesimal transfer matrix technique and sigma matrix method. The increase in the current in the bunch due to bunching as the beam passes through the inflector has been included in the beam dynamics. We observed a significant change in the beam envelopes compared to the case when the beam current in the bunch is constant. From the numerical results it is observed that initial beam conditions have considerable effect on the projected emittances at the exit of the inflector. The growth in projected emittances is comparatively large when one uses the upright input ellipses. It is found that convergent phase ellipses with different orientations in x and y planes and a comparatively smaller width in the y plane give better beam transmission and less emittance growth at the exit of the inflector.

We have also studied the feasibility of transverse beam matching at the input of the spiral inflector using an elliptical solenoid after the second solenoid magnet in the low energy beam transport line. First we have made detail investigation on the beam optical properties of an elliptical solenoid magnet. This analysis includes the effect of space charge and uses infinitesimal transfer matrix technique and sigma matrix method to evaluate the beam behaviour. We have studied the emittance growth through it as a function of beam current under various input beam conditions. It is observed that the magnitude of projected emittances in both the planes is always equal to each other at any point downstream for equal input beam emittances whether initial beam is axisymmetric or non-axisymmetric. On the other hand when the input beam emittances are unequal it is found that there is an exchange of emittance from one plane to the other plane. The projected x and y emittances at any point downstream are always unequal except at a point where these are equal in both the planes. The feasibility of using an elliptical solenoid for transverse matching of a space charge dominated beam to the acceptance of the spiral

inflector which requires converging non-axisymmetric beam has been studied. Numerical results of optimization relevant to our system are also presented.

7.2. Future works

Deep theoretical understanding of the dynamics of space charge dominated beam through cyclotron and spiral inflector has been gained. However most of the theoretical calculations are based on the use of ideal KV beam distribution whose full four dimensional structure corresponds to a singular, hyper-ellipsoidal shell in phase space. For strong space charge, this singular structure drives unphysical, higher-order instabilities which limit the practical use of the K-V distribution [106]. The method presented in this thesis can also be used with physical distributions of beam particle in an rms equivalent beam sense provided the variation of statistical beam emittances is negligible or sufficiently low [44]. In order to verify that the formulations presented also works for non K-V smooth distributions it is required to perform the particle-in-cell simulations.

We also like to point out here that the beam dynamics through the spiral inflector and along the accelerated orbits presented in the thesis assumes negligible energy spread in the beam. It is well known that an energy spread in the beam after a certain threshold value gives rise to the emittance growth for a space charge dominated beam [107]. The detailed simulation of beam dynamics with real beam distributions including the effect of energy spread in the beam would be of interest for future study.

The evolution of beam bunch in the combined electric and magnetic fields of a cyclotron is very complex due to the coupling between the radial and longitudinal motions which leads to the rotation of the bunch. In this work we have presented a simplified model assuming a uniform beam distribution and neglected the coupling between radial and longitudinal motions. Results so obtained present a good insight about the transverse behavior of the space charge dominated beam in a compact cyclotron. However, in order

to study the detailed beam behavior with real beam distributions including the effect of radial-longitudinal coupling it will be necessary to use particle-in-cell simulations [108]. This will provide more insight of the beam behaviour including the neighboring bunch effect in the cyclotron.

In this thesis we have discussed the dynamics of space charge dominated beam through the spiral inflector and in the 10 MeV compact cyclotron and discussed the various requirements of matching and efficient transmission. For better understanding of the beam behaviour it is necessary to do experiments on beam inflection. The experimental results would help to improve the modeling of the simulation work. The microwave ion source is operating and providing ~ 7 mA of beam current at 80 keV. Our future plan is to construct an inflector and a small magnet having similar characteristics as the central region of 10 MeV cyclotron and to study the high current beam inflection. The beam dynamics simulations based on simple model and verification of its results with actual measurements will help to define the final choice of parameters of the facility.

Another direction of future research would be to fabricate an elliptical solenoid and place in the low energy beam transport line to match the beam at the input of the spiral inflector and then study the beam transmission. Such kind of device for matching, to the best of our knowledge, has not been used in the injection line of existing facilities. Results of such experimentations would provide valuable input to the accelerator community for matching the space charge dominated beam to a non-axisymmetric system.

References

- [1] C. Rubbia, P. Mandrillon and N. Fietier; Proceedings of the 4th European Particle Accelerator Conference, EPAC- 94 (London, UK, 1994), p.270.
- [2] G. P. Lawrence, Nucl. Instr. and Meth. B **56** (1991)1000.
- [3] N. Fieuer and P. Mandrillon, Proceedings of the 14th International Conference on Cyclotron and their Applications, (Cape Town, 1995), p.598.
- [4] Th. Stambach, S. Adam, H. R. Fitze, W. Joho, M. Marki, M. Olivo, L. Rezzonico, P. Sigg and U. Schryber , Nucl. Instr. and Meth. B **113** (1996) 1.
- [5] M. Bopp et al., Proceedings of the 16th International Conference on Cyclotron and their Applications, (East Lansing, 2001), p.300.
- [6] V. S. Pandit, P. Sing Babu, A. Goswami and P. R. Sarma, Proceedings of the Asian Particle Accelerator Conference, APAC-07 (Indore, India, 2007), p.342.
- [7] A. Goswami, P. S. Babu and V. S. Pandit, Europ. Phys. Jour. Plus **127** (2012) 47.
- [8] P. Sing Babu, A. Goswami, P. R. Sarma and V. S. Pandit, Nucl. Instr. and Meth. A **624** (2010) 560.
- [9] V. S. Pandit, G. Pal, S. Bhattacharya, R. C. Yadav, S. K. Thakur, P. Y. Nabhiraj, Mou Chatterjee, A. Mishra, P. Sing Babu, A. Goswami and P. R. Sarma, Ion Beam Technology and Applications, SIBTA-2007 (Mumbai, India, 2007), p.109.
- [10] P. S. Babu, A. Goswami and V. S. Pandit, Nucl. Instr. and Meth. A **603** (2009)222.
- [11] A. Goswami, P. Sing Babu and V. S. Pandit, Proceedings of the 19th International Conference on Cyclotrons and Their Applications, (China, 2010) MOPCP038.
- [12] A. Goswami, P. S. Babu and V. S. Pandit, Europ. Phys. Jour. Plus **127** (2012) 79.
- [13] A. Goswami, P. S. Babu and V. S. Pandit, Nucl. Instr. and Meth. A **693** (2012)276.
- [14] E. O. Lawrence and M. S. Livingston, Phys. Rev. **40** (1932) 19.

- [15] J. J. Livingood, *Principle of Cyclic particle Accelerators*, D. Van Nostrand Comp., 1961.
- [16] M. S. Livingston, *High Energy Accelerators*, Interscience Publishers, 1952.
- [17] J. R. Richardson, *Sector Focusing Cyclotrons*, Progress in Nuclear Techniques and Instrumentations, Vol. 1, North Holland (1961), p.21.
- [18] F. A. Heyn and R. T. Khoe, Rev. Sci. Instr. **29** (1958) 662.
- [19] R. K. Bhandari, Proceedings of the 16th International Conference on Cyclotron and their Applications, (East Lansing, 2001), p. 84.
- [20] F. Marti et al., Proceedings of the 16th International Conference on Cyclotron and their Applications, (East Lansing, 2001), p. 64.
- [21] Y. Yano et al., Proceedings of the 16th International Conference on Cyclotron and their Applications, (East Lansing, 2001), p.161.
- [22] M. Schillo et al., Proceedings of the 16th International Conference on Cyclotron and their Applications, (East Lansing, 2001), p.37.
- [23] E. Baron et al., Proceedings of the 16th International Conference on Cyclotron and their Applications, (East Lansing, 2001), p. 431.
- [24] J. B. Warren, Proceedings of the 5th International Cyclotron Conference (Oxford, UK, 1969), CYC69A08.
- [25] S. Adam, Proceedings of the 14th International Conference on cyclotrons and their Applications, (Cape Town, South Africa, 1995), p.446.
- [26] Th. Stambach, Proceedings of the 15th International Conference on Cyclotrons and their Applications, (Caen, 1998), p.369.
- [27] H. G. Blosser and M. M. Gordon, Nucl. Instr. and Meth. **13** (1961) 101.
- [28] W. Joho, Proceedings of the 9th International Conference on Cyclotrons and their Applications, (Caen, 1981), p. 337.

- [29] W. B. Powel, IEEE, Trans. Nucl. Sci. **NS-13** (1966) 147.
- [30] R. W. Muller and Z. Angew, Phys, **18** (1965) 342.
- [31] R. W. Muller, Nucl. Instr. and Meth. **54** (1967) 29.
- [32] L. Belmont and J. L. Pabot, IEEE Trans. Nucl. Sci. **NS-13**, 191 (1966).
- [33] J. Ristic-Djurovic and N. Neskovic, Nucl. Instr. and Meth. A **406** (1998) 172.
- [34] V. S. Pandit, et al., Proceedings of the 2nd International Workshop on ADS and Thorium Utilization, (BARC, Mumbai, 2011) B7.
- [35] P. Sing Babu, A. Goswami and V. S. Pandit, Physics of Plasmas **18** (2011) 103117.
- [36] V. S. Pandit and P. S. Babu, Nucl. Instr. and Meth A **523** (2004) 19.
- [37] A. Goswami, P. S. Babu and V. S. Pandit, Nucl. Instr. and Meth. A **562** (2006) 34.
- [38] *MagNet User Guide*, Infolytica Corporation, version **6.26**.
- [39] M. M. Gordon, Part. Accel. **16** (1984) 39.
- [40] W. J. G. M. Kleeven and H. L. Hegedoorn, Proceedings of the First European Particle Accelerator Conference, (Rome, Italy, 1988), p.735.
- [41] R. A. Baartman, Proceedings of the 14th International Conference on Cyclotrons and their Applications, (Cape Town, 1995), p. 440.
- [42] H. L. Hagedoorn and N. F. Verster, Nucl. Instr. and Meth. **18-19** (1962) 201.
- [43] K. L. Brown, D. C. Carey, Ch. Iselin and Rothacker, *A computer program for designing charged particle beam transport system* (1980) CERN 80-04.
- [44] M. Reiser, *Theory and Design of Charged Particle Beams*, John Wiley and Sons, New York (1994).
- [45] C. Baumgarten, A. Barchetti, H. Einkenkel, D. Goetz and P. A. Schmelzbach, Rev. of Sci. Instr. **82** (2011) 053304.
- [46] V. S. Pandit, Nucl. Instr. and Meth. A **414** (1998) 127.
- [47] N. Fietier, P. Mandrillon, CERN/AT/95-03.

- [48] A. Papash and T. Zhang, Proceedings of the 17th International Conference on Cyclotrons and their Applications, (Tokyo, Japan, 2004), p. 444.
- [49] C. Qin, D. Z. Chen, L.C. Zhao, J. Yang and M.W. Fan, Nucl. Instr. and Meth. A **620** (2010) 121.
- [50] S. S. Rao, *Optimization: Theory and Applications*, Wiley Eastern, New Delhi, 1978 Chapter 6.2.
- [51] Y. Jongen and S. Zaremba, Proceedings of the CERN-1996-02, 1996, p. 139.
- [52] L.W. Root, M.Sc. Thesis, Univ. of British Columbia, 1972.
- [53] L.W. Root, Ph. D. Thesis, Univ. of British Columbia, 1974.
- [54] D. Toprek, Nucl. Instr. and Meth. A **440** (2000) 285.
- [55] V.S. Pandit, PRAMANA Journal of physics **59** (2002) 1019.
- [56] G. A. Karamysheva and L. M. Onischenko, Proceedings of XIX Russian Particle Accelerator Conference, RuPAC 2004, (Dubna, Russia, 2004), p. 198
- [57] F. B. Milton and J. B. Pearson, *CASINO User's Guide and Reference Manual*, TRI-DN-89-19, Vancouver, (1989).
- [58] Lj. M. Milinkovic, *RELAX3D Spiral Inflectors*, TR30-DN-89-21, Vancouver, (1989).
- [59] C. J. Kost, F.W. Jones, *RELAX3D User's Guide and Reference Manual*, TRI-CD-88-01, Vancouver, (1988).
- [60] N. Hazewindus, Nucl. Instr. and Meth, **118** (1974) 125.
- [61] S. B. Vorozhtsov, E. E. Perepelkin, A. S. Vorozhtsov, P. Beličev, N. Nešković, M. Rajčević, Proceedings of the XX Russian Particle Accelerator Conference, RuPAC 2006, (Novosibirsk, Russia, 2006), p.316.
- [62] D. Toprek, D. Reistad, B. Lundstrom and D. Wessman, Nucl. Instr. and Meth. A **486** (2002) 539.

- [63] R. J. Balden, W. Kleeven, L. S. Milinkovic, B. F. Milton and J. B. Pearson, Proceeding of the 12th International Conference on Cyclotrons and their Applications (Berlin, Germany, 1989), p. 435.
- [64] M. Sekiguchi and Y. Shida, Proceeding of the 3rd European Particle Accelerator Conference, (Berlin, Germany, 1992), p. 860.
- [65] T. Zhang, H. Yao, F. Guan, C. Chu, Y. Lu, X. Jia, J. Zhong, J. Yang, J. Xing and Y. Lin, Nucl. Instr. and Meth. B **261** (2007) 60.
- [66] D. Wutte, D. J. Clark, B. Laune, M. A. Leitner, and C. M. Lyneis, AIP Conference Proceeding **600** (2001) 445.
- [67] W. H. Zhang, H. Y. Ma, Y. Yang, Q. Wu, X. Z. Zhang et al., Rev. Sci. Instrum. **83** (2012) 02A329.
- [68] T. Thuillier, J. C. Curdy, T. Lamy, A. Lachaize, A. Ponton et al., AIP Conference Proceeding **749** (2005) 41.
- [69] M. Dehnel and T. Stewart, Proceedings of the 17th International Conference on Cyclotrons and Their Applications, (Tokyo, Japan, 2004), p.293.
- [70] D. Toprek, Nucl. Instr. and Meth. A **453** (2000) 501.
- [71] M. Sekiguchi, Proceeding of the 14th International Conference on Cyclotrons and their Applications, (Cape Town, South Africa, 1995), p. 450.
- [72] X. Jia and T. Jhang, Proceeding of the 18th International Conference on Cyclotrons and their Applications, (Giardini-Naxos, Italy, 2007), p. 72.
- [73] K. Allen, N. Brown and M. Reiser, Part. Accel. **45** (1994) 149.
- [74] Y. Kowamoto, J. Aoki and Y. Soga, Physics of Plasmas **11** (2004) 4868.
- [75] R. Baartman and W. Kleeven, Part. Accel. **41**(1993) 41.
- [76] E.V. Samsonov and L. M. Onischenko, Proceeding of the XIX Russian Particle Accelerator Conference (RuPAC 2004), (Dubna, Russia, 2004), p. 141.

- [77] Morgan P. Dehnel, Karl L. Erdman, Thomas Kou and Larry Root, Proceeding of the 15th International Conference on Cyclotrons and their Applications, (Caen, France, 1998), p. 239.
- [78] N. Gikal, G. G. Gulbekian and I. A. Ivanenko, Proceeding of the International Particle Accelerator Conference, IPAC-10, (Kyoto, Japan, 2010), p. 4536.
- [79] K-Je Kim, Phys. Rev. ST Accel. Beams **6** (2003) 104002.
- [80] M. Reiser, Jour. of Appl. Phys., **42** (1971) 4128.
- [81] J. Sacherer, IEEE Transaction on Nuclear Science **NS-18** (1971) 1105.
- [82] E. Pozdeyev, J. A. Rodriguez, F. Marti and R. C. York, Phys. Rev. ST Accel. Beams **12** (2009) 054202.
- [83] Y. Bi, T. Zhang, C. Tang, Y. Huang and J. Yang, Jour. of Appl. Phys., **107** (2010) 063304.
- [84] R. C. Davidson and H. Qin, *Physics of Intense Charged Particle Beams in High Energy Accelerators*, (World Scientific Publishing Company, 2001).
- [85] C. K. Allen and N. D. Pattengale, LANL Report No. LA-UR-02-4979, 2002.
- [86] I. S. Gradshteyn, I. M. Ryzhik, *Table of integrals, Series and Products*, (Academic Press, Inc., New York, 1980).
- [87] S. M. Lund, T. Kikuchi and R. C. Davidson, Phys. Rev. ST Accel. Beams, **12** (2009) 114801.
- [88] J. Struckmeier and M. Reiser, Part. Accel., **14** (1984) 227.
- [89] S. Humphries, S. Russell, B. Carlsten, L. Earley and P. Ferguson, Phys. Rev. ST Accel. Beams **7** (2004) 060401.
- [90] S. J. Russell et al., Phys. Rev. ST Accel. Beams **8** (2005) 080401.
- [91] R. Sarma, Eur. Phys. Jour. Plus **126** (2011) 54.
- [92] A. Goswami, P. S. Babu and V. S. Pandit, Nucl. Instr. and Meth. A **685** (2012) 46.

- [93] I. Kapchinskij and V. Vladimirskij, Proceedings of the International Conference on High Energy Accelerators and Instrumentation, CERN Scientific Information Service, (Geneva, 1959), p.274.
- [94] M. S. de Jong and E. A. Heighway, IEEE Transactions on Nuclear Science **NS-30** (1983) 2666.
- [95] J. Sacherer, Ph.D. Thesis, University of California, Berkeley, 1968.
- [96] Hong Qin, Moses Chung and R. C. Davidson, Phys. Rev. Lett. **103** (2009) 224802.
- [97] Hong Qin and Ronald C. Davidson, Physics of Plasmas **18** (2011) 056708.
- [98] Jing Zhou and Chiping Chen, Phys. Rev. ST Accel. Beams **9** (2006) 104201.
- [99] D. Chernin, Part. Accel. **24** (1988) 29.
- [100] J. Barnard, Proceeding of the 1995 Particle Accelerator Conference, Vol 5 (Dallas Texas, 1996) p 3241.
- [101] Ph. Royer, CERN- Neutrino Factory Note 11, 1999.
- [102] A. Goswami, P. S. Babu and V. S. Pandit, Nucl. Instr. and Meth. A **678** (2012) 14.
- [103] J. H. Li and J. Y. Tang, Nucl. Instr. Meth. A, **574** (2007) 221.
- [104] A. J. Dragt, F. Neri, and G. Rangarajan, Phys. Rev. A **45** (1992) 2572.
- [105] R. A. Kishek, J. J. Barnard and D. P. Grote, Proceedings of the Particle Accelerator Conference, (New York, 1999), p.1761.
- [106] I. Hofmann, L. J. Laslett, L. Smith, and I. Haber, Part. Accel. **13** (1983) 145.
- [107] J. J. Barnard, J. Miller and I. Haber, Proceedings of the Particle Accelerator Conference, (Washington, 1993), p. 3612.
- [108] J. Yang, A. Adelman, M. Humbel, M. Seidel and T. J. Zhang, Phys. Rev. ST Accel. Beams **13** (2010) 064201.

List of publications

- *[1] Behavior of space charge dominated beam in a high current compact cyclotron;
A. Goswami, P. Sing Babu and V. S. Pandit,
[Nuclear Instruments and Methods in Physics Research A 562 \(2006\) 34.](#)

- [2] Simulation of beam bunching in the presence of space charge effects;
P. Sing Babu, **A. Goswami** and V. S. Pandit,
[Nuclear Instruments and Methods in Physics Research A 603 \(2009\) 222.](#)

- *[3] Optimization of sector geometry of a compact cyclotron by random search and matrix method;
P. Sing Babu, **A. Goswami**, P. R. Sarma and V. S. Pandit,
[Nuclear Instruments and Methods in Physics Research A 624 \(2010\) 560.](#)

- [4] Behavior of space charge dominated beam during longitudinal compression in a bunching system;
P. Sing Babu, **A. Goswami** and V. S. Pandit,
[Nuclear Instruments and methods in Physics Research A 642 \(2011\) 1.](#)

- [5] Envelope equations for cylindrically symmetric space charge dominated multi species beam;
P. Sing Babu, **A. Goswami** and V. S. Pandit,
[Physics of Plasmas 18 \(2011\) 103117.](#)

- [6] Effect of nonuniform radial density distribution on space charge dominated beam bunching;
P. Sing Babu, **A. Goswami** and V. S. Pandit,
[Physics of Plasmas 18 \(2011\) 113104.](#)

- *[7] Investigation on beam envelope oscillations and amplitude growth in a high-current compact cyclotron;
A. Goswami, P. Sing Babu and V. S. Pandit,
[European Physical Journal Plus 127 \(2012\) 47.](#)

- *[8] Space charge dominated beam dynamics in a spiral inflector for a compact cyclotron;
A. Goswami, P. Sing Babu and V. S. Pandit,
[European Physical Journal Plus 127 \(2012\) 79.](#)

- [9] Transfer matrix of a Glaser magnet to study the dynamics of non-axisymmetric beam;
A. Goswami, P. Sing Babu and V. S. Pandit,
[Nuclear Instruments and methods in Physics Research A 678 \(2012\) 14.](#)
- *[10] Beam focusing characteristic of an elliptical solenoid magnet in the presence of space charge;
A. Goswami, P. Sing Babu and V. S. Pandit,
[Nuclear Instruments and Methods in Physics Research A 685 \(2012\) 46.](#)
- [11] Self-consistent space charge dominated beam dynamics in a spiral inflector;
A. Goswami, P. Sing Babu and V. S. Pandit,
[Nuclear Instruments and methods in Physics Research A 693 \(2012\) 276.](#)
- [12] Transport characteristics of a Glaser magnet for axisymmetric and non-axisymmetric space charge dominated beam;
A. Goswami, P. Sing Babu and V. S. Pandit,
[Physics of Plasmas 19 \(2012\) 123105.](#)

* Indicates publications related to this thesis.